

Study of X-ray Emission from the Giant Molecular Clouds in
the Galactic Center Region

Masayoshi Nobukawa

Department of Physics, Graduate School of Science, Kyoto University
Kitashirakawa Oiwake-cho, Sakyo-ku, Kyoto, 606-8502, Japan
nobukawa@cr.scphys.kyoto-u.ac.jp

January 5 2011

Abstract

There are K-shell emission lines of neutral Fe (Fe I $K\alpha$) correlated with giant molecular clouds in the Galactic center (GC) region. The Fe I $K\alpha$ emission is one of the key for the structure and activity of the GC, including the super-massive black hole Sagittarius A* (hereafter Sgr A*) with a huge mass $4 \times 10^6 M_{\odot}$. The origin of the Fe I K is still open question, but possibly due either to X-ray radiation from an external object (X-ray reflection nebula: XRN) or to bombardment of low energy cosmic-ray electrons (LECRE) to neutral atoms in dense molecular clouds. In order to resolve the problem, we made deep observations of molecular clouds emitting the Fe I $K\alpha$ line in the Sagittarius (Sgr) A, B1, B2, and C regions with the Japanese X-ray scientific satellite Suzaku.

We discovered $K\alpha$ lines of neutral Ar, Ca, Cr, Mn atoms in addition to those of Fe and Ni from a cloud in the Sgr A region. The equivalent widths of these emission lines require that the metal abundances in the GC region are ~ 1.6 and ≥ 4 solar values in the XRN and LECRe scenarios, respectively. On the other hand, the X-ray spectrum of the hot plasma extended over the GC region exhibits the metal abundances of 1–2 solar values. The XRN model agrees with these results.

We detected X-ray emissions with strong Fe I $K\alpha$ lines from molecular clouds in the Sgr B1 and C regions. The X-ray spectra consist of the Fe I $K\alpha$ lines with large equivalent widths of 1–2 keV and deeply-absorbed hard continua (column density $N_{\text{H}} \sim 10^{23} \text{ cm}^{-2}$, photon index $\Gamma \sim 1.7$), and hence these clouds are also likely to be XRNe.

We found that the Fe I $K\alpha$ fluxes of the two clouds in the Sgr B2 region had decreased in correlation to the hard-continuum fluxes by factor of 0.4–0.5 from 2005 to 2009. The time interval of 4 years is nearly equal to the light-traveling across the clouds. The rapid and correlated time-variability in addition to the large equivalent width of Fe I $K\alpha$ are consistently explained by the XRN scenario due to an X-ray flare from an external source with the duration time of shorter than 4 years. The peak-position of the Fe I- $K\alpha$ emission shifted slightly to a larger distance from the GC, Sgr A*, and hence the X-ray flare source should be located in the Sgr A*-side with respect to Sgr B. Based on these facts, the luminosity of the X-ray flare is needed to be larger than $10^{40} \text{ erg s}^{-1}$, which is 50 times larger than the Eddington limit of an object with the sun's mass. Therefore Sgr A* is an unique candidate to illuminate the clouds in X-ray.

When the Sgr A* flare is applied to the origin of the Fe I K emission from the other clouds, the required luminosities are similar values of $\sim 10^{41} \text{ erg s}^{-1}$. Thus, we reached a conclusion that the super-massive black hole Sgr A* made a single X-ray flare 300 years ago and illuminated the molecular clouds in the vicinity.

Contents

1	Introduction	1
1.1	Overview of the central region in Milky Way Galaxy	1
1.2	SMBH, Sgr A*	1
1.2.1	X-ray Observations of Sgr A*	2
1.2.2	Gamma-rays from the direction near Sgr A*	4
1.3	Diffuse X-Ray Emission from the GC Region	5
1.3.1	Discovery of Fe Lines from the GC Region	5
1.3.2	Origin of Fe XXV and Fe XXVI	7
1.3.3	GC Hot Plasma	8
1.4	Fe I $K\alpha$ Emission from Giant Molecular Clouds	10
1.4.1	Possible Origins for the Fe I $K\alpha$ Emission	10
1.4.2	Recent Results—time variability of X-ray emissions—	11
1.5	Aim of this thesis	13
2	Suzaku X-ray Satellite	15
2.1	Suzaku Satellite	16
2.2	X-Ray Telescope	16
2.3	X-Ray Imaging Spectrometer	23
2.3.1	Introduction of X-ray Charge Coupled Device Cameras	23
2.3.2	Overview of XIS	24
2.3.3	Charge Injection Capability	27
2.3.4	XIS Performance in orbit	30
3	K-shell Lines of Neutral Atoms	37
3.1	Introduction	37
3.2	Observations and Data Reduction	38
3.3	Analysis and Results	39
3.3.1	6.4 keV line Image	39
3.3.2	Gain Tuning	40
3.3.3	Model Construction	41
3.3.4	Spectral Fitting	43
3.4	Discussion for the X-ray Emission from the Sgr A region	46
3.4.1	The GC hot plasma	46
3.4.2	Origin of the Neutral Clump	47

3.5	Summary	49
4	Other 6.4 keV Clouds	53
4.1	Sgr B1	54
4.1.1	Introduction for Sgr B1	54
4.1.2	Observation and Data Reduction	54
4.1.3	Analysis and Results	55
4.1.4	Discussion for M 0.51–0.10	60
4.1.5	Summary	63
4.2	Sgr C	65
4.2.1	Introduction for Sgr C	65
4.2.2	Observation and Data Reduction	65
4.2.3	Analysis and Results	65
4.2.4	Discussion for the 6.4 keV Clouds in Sgr C	71
4.2.5	Summary	76
5	Time-Variability of X-rays from Sgr B2	77
5.1	Introduction	77
5.2	Observation and Data Reduction	78
5.3	Analysis	78
5.3.1	X-ray Images	78
5.3.2	Spectra	81
5.4	Discussion for the 6.4 keV Clouds in Sgr B2	82
6	Discussion	85
6.1	Features of the 6.4 keV Clouds	85
6.2	Irradiating Source of the 6.4 keV Clouds	87

List of Figures

1.1	Surrounding environment of Sgr A*	2
1.2	X-ray flare from Sgr A*	4
1.3	X-ray spectra and 6.7 keV line intensity distribution (Ginga)	6
1.4	X-ray spectrum of the GCDX obtained by ASCA	7
1.5	X-ray spectrum of the GCDX obtained by ASCA	8
1.6	X-ray map in the 6.4 keV line obtained by ASCA	10
1.7	Time variabilities of the 6.4 keV fluxes from the Sgr B2 clouds	11
1.8	Fe I $K\alpha$ image of the different XMM-Newton observations	12
2.1	Schematic view of the Suzaku satellite	15
2.2	X-ray telescope onboard the Suzaku satellite	17
2.3	Wolter type-I grazing incident optics in the XRT	17
2.4	Comparison of effective areas of the X-ray telescopes onboard the X-ray satellites	19
2.5	Point spread function of the XRT	20
2.6	Vignetting of the XRT	20
2.7	X-ray path through the XRT	21
2.8	Wide-range vignetting function of the Suzaku XRT	22
2.9	Schematic view of a MOS structure	23
2.10	Schematic view of charge transfer in a CCD	24
2.11	Picture and cross section of XIS	25
2.12	Picture of the CCD installed in the base	25
2.13	Schematic view of the XIS CCD	26
2.14	Schematic view of the CI technique	28
2.15	Schematic view of measuring procedure of CTI with the CFCI technique	29
2.16	Pulse height of the Mn I $K\alpha$ line from the calibration source.	30
2.17	Time histories of the Mn I $K\alpha$ line energy.	31
2.18	Time histories of the OXII $K\alpha$ line energy	31
2.19	Schematic response function of the XIS	32
2.20	Time histories of the Mn I $K\alpha$ line width	33
2.21	Time history of the OVII $K\alpha$ line width	33
2.22	Quantum efficiency of the XIS	34
2.23	Spectra of the non-X-ray background	35
2.24	Dependence of the NXB on the COR and ACTY	36

2.25	XIS background counting rate	36
3.1	Sgr A region in the 6.4 keV image	37
3.2	X-ray image in the 6.4 keV neutral iron line at the east region of Sgr A*	40
3.3	X-ray spectra in the Source and the Reference regions	41
3.4	Spectral fitting with a model consisting of plasma and neutral components.	42
3.5	Line intensity ratios of He- and H-like ions.	45
3.6	Relationship between the electron spectral index and the X-ray photon index	48
3.7	Equivalent widths of $K\alpha$ lines of various neutral atoms.	49
3.8	Equivalent width of various elements expected in the XRN and LECRe models	50
4.1	6.4 keV image in the GC region	53
4.2	Full spectrum of the Sgr B1 region	55
4.3	X-ray images in the Sgr B1 region.	57
4.4	The 6.7 keV band image between the Sgr A and Sgr B2 regions	58
4.5	Distributions of the 6.7 keV line flux and the photon flux ratio between the 6.7 and 6.9 keV lines	59
4.6	Background-subtracted spectrum of M 0.51–0.10.	60
4.7	Distribution of the molecular clouds and H II regions in the GC region	61
4.8	Full spectrum of the Sgr C region	66
4.9	X-ray images of the Sgr C region	67
4.10	NXB-subtracted spectra of M 359.43–0.07, M 359.47–0.15, and the outer region	68
4.11	Correlation between the equivalent widths of the Fe $K\alpha$ and Fe XXV $K\alpha$ lines	71
4.12	Background-subtracted spectra of M 359.43–0.07 and M 359.47–0.15	72
4.13	X-ray and radio features in the Sgr C region	74
4.14	6.4 keV image toward the Sgr C region with radio contours of the CS emis- sion line	75
5.1	Sgr B region in the 6.4 keV image	77
5.2	X-ray images in Fe I $K\alpha$ and 8-10 keV near Sgr B2 and M 0.74–0.09.	79
5.3	Projected profile of the 6.4 keV line intensity in the 6.4 keV clouds	80
5.4	X-ray spectra of molecular clouds, Sgr B2 and M 0.74–0.09 on 2005 and 2009.	81
5.5	Schematic face-on view of movement of "X-ray echoes" in the molecular clouds	83
6.1	Required luminosity of the irradiating source	88
6.2	Distribution of the 6.4 keV Clouds	88

List of Tables

3.1	Observation Data List.	39
3.2	Fitting results of <i>Plasma</i>	46
3.3	Fitting Results of <i>Neutral</i> and those of calculated values.*	47
4.1	Result of spectral fitting in Sgr B1	61
4.2	Comparison between required luminosities and observed luminosities	62
4.3	Center energies of the Fe, Ni line from the GCDX	68
4.4	Best-fit parameters for the NXB-subtracted spectra	69
4.5	The best-fit parameters of the spectral fittings to the background (GCDX) subtracted spectra of M 359.43–0.07 and M 359.47–0.15.	73
5.1	Best-fit parameters.*	82
6.1	Parameters of 6.4 keV clouds	86

Chapter 1

Introduction

1.1 Overview of the central region in Milky Way Galaxy

The central region of Milky Way Galaxy (Galactic center, GC) is the closest among those of all galaxies in the universe. A super-massive black hole (SMBH) Sagittarius A* (hereafter, Sgr A*) has been found, which sits at a dynamical center of the Galactic gravity (e.g., Ghez et al. 2008). Many molecular gases, stars, and supernova remnants concentrate in the surroundings of Sgr A*. Interactions between these objects induce star-formations. Many molecular clouds, stellar clusters, and H II regions have been frequently produced in the GC. Strong magnetic field (several tens of μG) has been observed and the energy density of cosmic-rays is also significantly higher than that in the vicinity of the Earth. The GC is an excellent laboratory to research high energy phenomena in astrophysics.

The GC are difficult to be observed in the optical and ultraviolet wavebands because of large extinction and absorption due to inter-stellar dust and gas ($A_V \sim 30$ mag) (e.g. Rieke et al. 1989). The 30 mag of visual extinction corresponds to a column density $N_{\text{H}} \sim 6 \times 10^{22} \text{ cm}^{-2}$ (Predehl & Schmitt 1995), and hence the obscuring medium becomes partially transparent to X-rays from the GC region at energies > 2 keV. The GC can be also observed in radio and infrared band with long wavelengths.

1.2 Super-Massive Black Hole, Sagittarius A*

Nuclei of most galaxies are now believed to harbour super-massive black holes with 10^6 – $10^9 M_{\odot}$ (solar mass). The motions of stars in the central few pc of Milky Way Galaxy indicate the presence of a super-massive black hole with a mass of $\sim 4 \times 10^6 M_{\odot}$ (Genzel et al. 2000; Ghez et al. 2000; Ghez et al. 2008). The black hole coincides with a compact non-thermal radio source, Sgr A*, and the radio emission is thought to be powered by the gravitational potential energy released by matter as it accretes onto the super-massive black hole. However, no counterpart had been found in other wavelength. Sgr A* was much fainter especially in X-rays, which has cast some doubt on adoption of the accretion model.

A cluster of luminous young stars lies in the immediate vicinity of Sgr A*. Many of them are windy emission-line stars that presumably supply the matter which the black

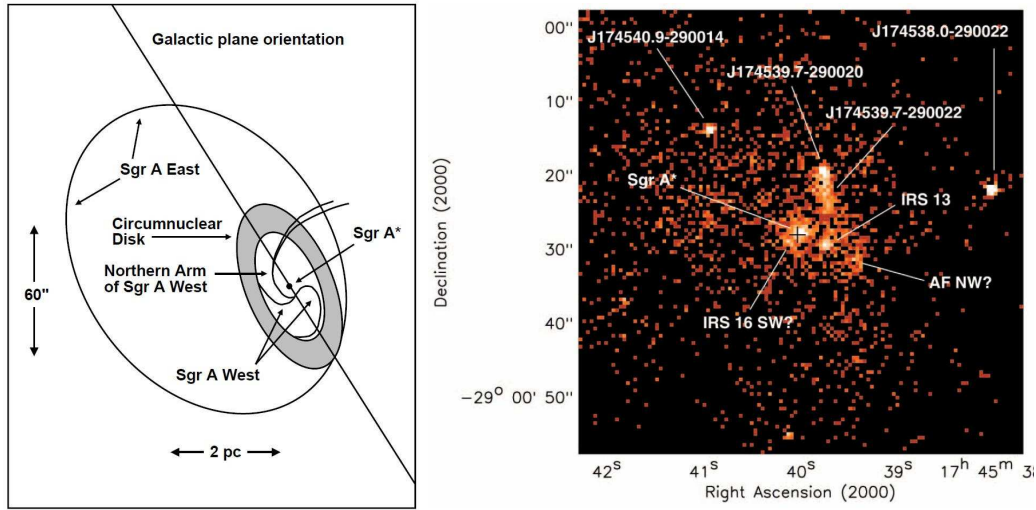


Figure 1.1: Left panel: Schematic diagram of the principle constituents of the Sgr A radio complex (Baganoff et al. 2003). The outer ellipse depicts the location of the radio shell of Sgr A East, which is a filled-center structure in X-rays. The circumnuclear disk may affect the morphology of the super-massive black hole, Sgr A*, lies at the center of a cavity surrounded by the circumnuclear disk. The ionized gas features of Sgr A West and the central cluster of luminous, hot stars also lie within the cavity. Right panel: Chandra X-ray image in 0.5–7 keV with logarithmic scaling of the central $1' \times 1'$ of the GC (Baganoff et al. 2003). The black cross marks the radio position of Sgr A*. The cross lies superposed on the X-ray source that we associate with Sgr A* based on the extremely close positional coincidence. Other sources are a counter part of infra-red stars or new X-ray binaries.

hole is presently accreting (e.g., Krabbe et al. 1995; Paumard et al. 2001). These stars and their colliding winds are themselves potential X-ray sources (Ozernoy et al. 1997). This cluster excites a parsec-scale H II region, Sgr A West, that is well studied at radio and infrared wavelengths. The surrounding of Sgr A West is the dense, predominantly neutral circumnuclear disk (Morris & Serabyn 1996 and references therein). Beyond that, on a scale of ~ 10 pc, a supernova remnant, Sgr A East, with a nonthermal radio shell surrounds the circumnuclear disk in projection.

1.2.1 X-ray Observations of Sgr A*

X-ray observations were carried out with various instruments. The observations with an X-ray telescope were started by the Einstein satellite. 1E 1742.5-2859, the strongest among detected sources was centered only $20''$ from the position of Sgr A* (Watson et al. 1981). Assuming an absorbed thermal bremsstrahlung model with $kT=5$ keV and $N_{\text{H}} = 6 \times 10^{22} \text{ cm}^{-2}$, Watson et al. (1981) estimated the absorption-corrected 0.5–4.5 keV luminosity of this source to be $9.6 \times 10^{34} \text{ erg s}^{-1}$. Hard X-ray observations were made with $3'–5'$ using Spacelab-2/XRT (Skinner et al. 1987), Spartan-1 (Kawai et al. 1988), and Granat/ART-P (Sunyaev et al. 1993; Pavlinsky et al. 1994). These observations suggested the presence of a long-term variable source near the position of Sgr A* with an

average 4–20 keV luminosity of $\sim 10^{36}$ erg s $^{-1}$.

ROSAT observed the Galactic center and detected 14 sources within the central $30' \times 30'$ region. With the relatively high spatial resolution of $10''$ – $20''$, it resolved 1E 1742.5-2859 into three sources, of which RX J1745.6-2900 was coincident within $10''$ with the radio position of Sgr A* (Predehl & Trümper 1994; Predehl & Zinnecker 1996). Predehl & Trümper (1994) adopted a thermal bremsstrahlung model with $kT = 5$ keV, but with $N_{\text{H}} = 1.5 \times 10^{23}$ cm $^{-2}$ to obtain broadband agreement with the hard X-ray data described above, and derived an unabsorbed 0.8–2.5 keV luminosity of $\sim 10^{36}$ erg s $^{-1}$ for the source.

The first X-ray image with an X-ray CCD of the GC was made in 1993 with ASCA (Koyama et al. 1996). The angular resolution of the X-ray telescope onboard ASCA was $\sim 1'$. ASCA detected diffuse thermal emission ($kT \sim 10$ keV) covering the central square degree of the GC (Galactic center diffuse X-rays, GCDX: see section 1.3). A $2' \times 3'$ elliptical region filling a shell of a supernova remnant, Sgr A East showed bright diffuse emission. After correction for a measured absorption of $N_{\text{H}} \sim 7 \times 10^{22}$ cm $^{-2}$, the unabsorbed 2–10 keV luminosity of this gas was found to be $\sim 10^{36}$ erg s $^{-1}$. No subtraction was performed for the spatially variable local background, and consequently ASCA could only place an upper limit of $\sim 10^{36}$ erg s $^{-1}$ on the X-ray luminosity of Sgr A*.

Koyama et al. (1996) found a hard X-ray source, AX J1745.6–2901 located $1.3'$ away from Sgr A*. During their second observation made in 1994, Maeda et al. (1996) discovered an X-ray burst and eclipses with a period of 8.4 hr from the hard source, establishing that it was an eclipsing low-mass X-ray binary (LMXB: see also Hyodo et al. 2009). Only one Ariel V cataloged transient source, A 1742-289 (Eyles et al. 1975), which appeared in 1975, positionally coincides within the error region. However, Kennea & Skinner (1996) reanalyzed the Ariel V data taken in 1975 and found no eclipses from A 1742-289. Hence, the hard source was identified as a newly discovered LMXB and given the name AX J1745.6-2901 (Maeda et al. 1996). Maeda et al. (1996) reported that the absorbed flux from this source varied from 1×10^{-11} to 4×10^{-11} erg cm $^{-2}$ s $^{-1}$, which was similar to the variations reported previously by the lower resolution hard X-ray instruments. Hence, the hard X-ray fluxes attributed to Sgr A* may have been contaminated significantly by AX J1745.6-2901 and A 1742-289 (see also Beckert et al. 1996).

A BeppoSAX observation, with on-axis angular resolution of $\sim 1.3'$ and an energy range similar to ASCA, was performed in 1997 (Sidoli et al. 1999b). BeppoSAX detected the diffuse emission near Sgr A*, measured the absorption column to be $N_{\text{H}} \sim 8 \times 10^{22}$ cm $^{-2}$, and set a tighter upper limit on the 2–10 keV luminosity of Sgr A* of $\sim 10^{35}$ erg s $^{-1}$.

Recently, the Chandra satellite with the highest resolution $0.5''$ found a compact X-ray source, GXOGC J174540.0–290027, coincides with Sgr A* within $0.3''$ (Baganoff et al. 2001; 2003). The spectrum is represented with an absorbed power-law with photon index $\Gamma \sim 2.7$ and column density $N_{\text{H}} \sim 10^{23}$ cm $^{-2}$ or with an absorbed optically thin thermal plasma with $kT \sim 2$ keV and $N_{\text{H}} \sim 10^{23}$ cm $^{-2}$. The detected X-ray flux in 2–10 keV of 10^{-13} erg s $^{-1}$ cm $^{-2}$ is too faint to be detected with the previous X-ray instruments. The absorption-corrected luminosity in 2–10 keV was estimated to be $2.2_{-0.3}^{+0.4} \times 10^{33}$ erg s $^{-1}$. Baganoff et al. (2001) also discovered that Sgr A* flared up in 2000. The luminosity in the flare state was $1 \pm 0.1 \times 10^{35}$ erg s $^{-1}$, about fifty times higher than that in the quiescent

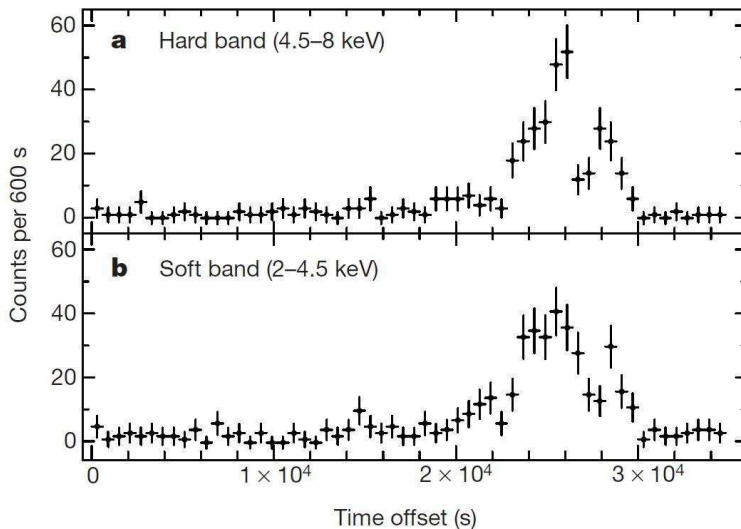


Figure 1.2: X-ray light curve taken from Sgr A* (Baganoff et al. 2001). (a) Light curve in hard band (4.5–8 keV). (b) Same as (a) but in soft band (2–4.5 keV) counts. The transverse and vertical axes show the time offset from the start of the observation and count rates normalized to 600 s. During the quiescent intervals at the beginning and end of this observation, the mean count rate in the 2–8 keV band is $6.4 \pm 0.6 \times 10^{-3}$ counts s^{-1} . The detected count rate at the peak of the flare is 0.16 ± 0.01 counts s^{-1} , which is larger than that in the quiescent level by more than one order of magnitude.

state. The photon index of the spectra seemed to vary from ~ 2.7 in quiescence to ~ 1.0 in flaring. The luminosity is 10^8 – 10^{10} times fainter than the Eddington luminosity of a source with the mass of $4 \times 10^6 M_{\odot}$. Baganoff et al. (2003) discussed the radiation model of Sgr A*. In the model, low energy photons ($\lambda \sim$ sub-mm) are generated by synchrotron of relativistic electrons, and then X-rays are produced via up-scattering of the sub-millimeter photons off the relativistic electrons (synchrotron self-Compton model).

1.2.2 Gamma-rays from the direction near Sgr A*

Gamma-rays were also detected from the position coincide with Sgr A* by some instruments. The EGRET team found that the 100 MeV to 10 GeV gamma-ray emission comes from the GC region at $(l, b) = (0.11^{\circ}, -0.04^{\circ})$ with the errors 0.13° in the 95% confidence level (Mayer-Hasselwander et al. 1998). An Imaging Atmospheric Cerenkov Telescope (IACT), Cangaroo-II detected very high energy (VHE) TeV gamma-rays from a point-like source at a position consistent with that of the Sgr A* (Tsuchiya et al. 2004). The IACT, H.E.S.S. also detected VHE gamma-rays in 0.1–10 TeV and decided the peak position of $(l, b) = (0.0^{\circ} \pm 0.1^{\circ}, 0.0^{\circ} \pm 0.1^{\circ})$ (Aharonian et al. 2006). Although high energy gamma-rays from Sgr A* suggested that super-massive black hole is a site where cosmic-rays are accelerated, the less position uncertainty than that in the radio and X-ray results has remained some origin for the gamma-ray emission detected from the GC.

Some galactic nuclei have high luminosity comparable to the Eddington limit (Active

galactic nuclei: AGN). The reason why the nucleus of Milky Way Galaxy is much fainter than the AGN is under intense debate.

1.3 Diffuse X-Ray Emission from the GC Region

There are a number of types of astrophysical objects which emit X-rays, from galaxy clusters, through black holes in active galactic nuclei to galactic objects such as supernova remnants, stars, and binary systems containing white dwarfs, neutron stars or black holes (X-ray binaries). A combination of many unresolved X-ray sources is thought to produce the observed X-ray background. These are divided into discrete (point-like) and extended objects.

Early X-ray observations discovered the presence of several discrete objects concentrating on the Galactic plane, especially in the Galactic center region (e.g., Watson et al. 1981; Skinner et al. 1987; Kawai et al. 1988). The objects are bright X-ray binaries of black holes or neutron stars with high luminosity of $L_X = 10^{36} - 10^{38}$ erg s $^{-1}$.

On the other hand, diffuse X-ray emission which were not able to be resolved into discrete sources was found from the Galactic plane by various instruments, rockets, balloons, and satellites (Cooke et al. 1969; Hudson et al. 1971; Bleach et al. 1972; Worrall et al. 1982; Iwan et al. 1982). This emission has been called as the Galactic ridge X-ray emission (GRXE). The hard spectrum of the GRXE was explained by an optically thin thermal plasma with a temperature $kT \sim 10$ keV (Iwan et al. 1982) or by a power-law model with a photon index $\Gamma = 2-3$ (Bleach et al. 1972).

Many possible origins have been proposed by many researches so far. Worrall et al. (1982) proposed that the seemingly extended emission of the GRXE comes from integration of discrete sources, accreting white dwarfs (cataclysmic variables) and binary stars with strong coronal activity. On the other hand, Koyama et al. (1989) suggested that the GRXE is truly diffuse, and originates from thermal hot plasma gas with temperature $kT = 1-10$ keV. Ginzburg & Syrovatskii (1964) and Blumenthal & Gould (1970) attempted to explain by another scenario that the nonthermal X-ray spectrum is generated by inverse Compton scattering of the cosmic microwave background ($T \sim 3$ K) on cosmic-ray electrons of a few GeV. Protheroe et al. (1980) interpreted the X-ray emission by the synchrotron radiation of the cosmic-ray electrons of 10^{14} eV interacting with a interstellar magnetic field of several μ G. However, no critical information from the observations had been found and the origin had been under discussion for a long time. It is not understood whether the GRXE is integration of discrete stars or truly diffuse.

1.3.1 Discovery of Fe Lines from the GC Region

The Tenma and Ginga satellites made a breakthrough discovery of a 6.7 keV emission line of Fe XXV $K\alpha$ in the GRXE spectrum (see left panel in figure 1.3). Moreover, the distribution of the 6.7 keV emission line intensity has two components widely extending over the Galactic plane and concentrating within $\sim 1^\circ$ of the Galactic center (GC) at $l = 0^\circ$ (Koyama et al. 1986a; Koyama et al. 1990; Yamauchi et al. 1990). This diffuse

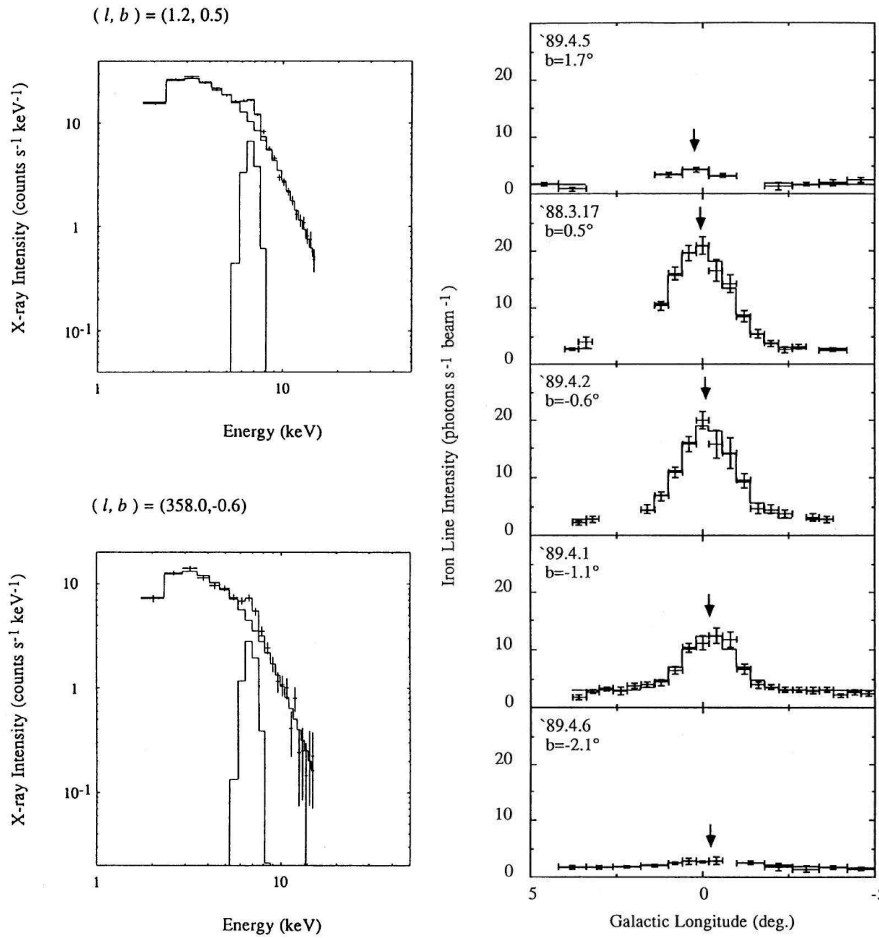


Figure 1.3: Left: X-ray spectra of the GCDX at $(l, b) = (1.2^\circ, 0.5^\circ)$ and $(358.0^\circ, -0.6^\circ)$ near the Galactic center taken by the Ginga satellite (Yamauchi et al. 1990). A pronounced Fe line at 6.7 keV in the spectra is modeled with a Gaussian. Right: Galactic longitude distribution of the Fe line intensity (Yamauchi et al. 1990). Each panel shows the distribution at a different latitude $b = 1.7^\circ, 0.5^\circ, -0.6^\circ, -1.1^\circ,$ and -2.1° . The arrows indicate the intensity peak of each profile.

X-ray emission is called as the GCDX. The existence of the highly ionized Fe suggested that the diffuse X-ray emission possibly comes from the optically thin thermal plasma with the temperature of $kT \sim 10$ keV.

Detailed image and spectrum in the hard X-ray band up to 10 keV were obtained by the X-ray telescopes aboard the ASCA satellite (Koyama et al. 1996). Superior energy resolution of the X-ray CCD cameras (SIS) demonstrated that the Fe emission line is due to complex of three different ionization states, and consists of emission lines at 6.4, 6.7, and 7.0 keV (figure 1.4). The 6.7 and 7.0 keV lines are from highly-ionized ions of He-like (Fe XXV $K\alpha$) and H-like (Fe XXVI $K\alpha$) Fe, respectively. On the other hand, the energy 6.4 keV of the other line indicated that Fe is a neutral or lowly-ionized state. Thus, the GCDX consists of at least two components. One associates with 6.7 and 7.0 keV Fe lines and the other is a neutral component with the 6.4 keV Fe line.

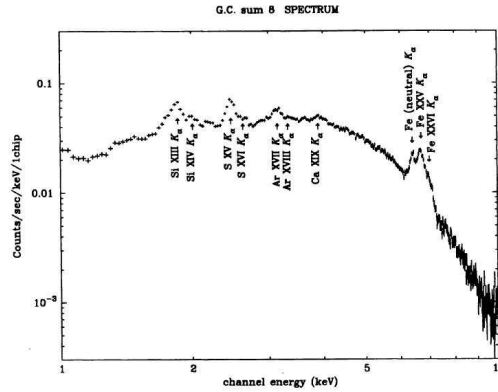


Figure 1.4: X-ray spectrum of the GCDX obtained by ASCA. The Fe lines of neutral (6.4 keV), He-like (6.7 keV), and H-like (7.0 keV) are resolved. There are many emission lines of the other heavy elements, Si, S, Ar, and Ca in highly-ionized states.

We review the previous researches of the 6.7 and 7.0 keV lines in the next section, while those of the 6.4 keV line is mentioned in section 1.4.

1.3.2 Origin of Fe XXV and Fe XXVI

Two plausible origins for the highly-ionized Fe lines (Fe XXV and Fe XXVI) have been proposed. One is collisional excitation in the thin thermal plasma with the high temperature as above mentioned (Koyama et al. 1989; Yamauchi et al. 1990), and the other is charge exchange (CX) recombination due to interaction between bare Fe in cosmic-rays and a hydrogen atom in an interstellar medium (Tanaka et al. 2000).

A broadened Fe line width of ~ 70 eV was found in the X-ray spectrum obtained by ASCA (Tanaka et al. 2000). This suggested that the velocity of the Fe ion was 3000–5000 km s^{-1} , which was greatly exceeded the sound speed ~ 1000 km s^{-1} in the ~ 10 keV plasma. Although intensities of the two Fe lines are expected to be the same in the CX scenario, the observed intensity ratio between Fe XXV $K\alpha$ and Fe XXVI $K\alpha$ is $\sim 1 : 2$ across all the GC region (Koyama et al. 1996). Moreover, no excesses were seen even at regions with dense molecular gases, i.e. molecular clouds (Koyama et al. 1996). These facts deprecate the CX scenario and favored the hot plasma one.

The Fe XXV $K\alpha$ line has fine structures consisting of different transitions of resonance, intercombination, and forbidden. The center energies of the resonance, intercombination, and forbidden lines are 6.70, 6.67–6.68, and 6.64 keV, respectively. The forbidden line is stronger than the resonance line in the CX process, whereas the resonance line is stronger in the hot plasma (Koyama et al. 2007c, and reference therein). Although the X-ray CCDs, which have the highest energy resolution among the instruments launched in orbit, cannot resolve the fine structures, the two origins are distinguishable by the center energy of the Fe XXV $K\alpha$ line. The hot plasma should provides the center energy 6.680–6.685 keV for the Fe XXV $K\alpha$ (Koyama et al. 2007c). On the other hand, Wargelin et al. (2005) measured by a laboratory experiment that the Fe XXV $K\alpha$ line in the CX process has

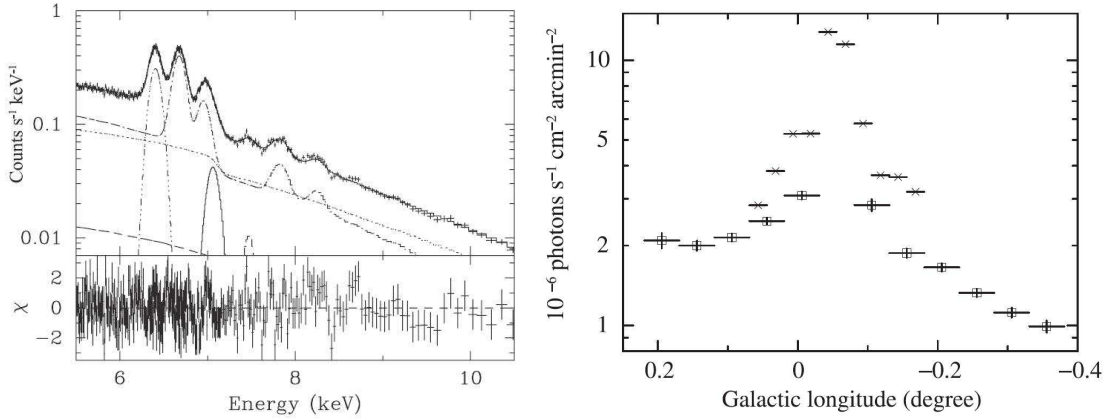


Figure 1.5: Left: X-ray spectrum of the GCDX obtained by Suzaku (Koyama et al. 2007c). The model is a thin thermal plasma of $kT = 6.5$ keV plus a power-law of the photon index $\Gamma = 1.4$ with 3 Gaussian lines at 6.40, 6.68, and 6.97 keV and an iron absorption edge at 7.11 keV. Right: line fluxes of Fe XXV $K\alpha$ are given by the squares, while the integrated point source fluxes in the 4.7–8 keV band are plotted by the crosses (Koyama et al. 2007c). The horizontal axis is the Galactic longitude, but the vertical axis is a logarithmic scale.

lower energy 6.666 ± 0.005 keV.

Suzaku, which is described in chapter 2, obtained the most excellent X-ray spectrum of the GCDX in the past, and decided the center energy 6.680 ± 0.001 keV for the Fe XXV $K\alpha$ line successfully (left panel in figure 1.5). The value is inconsistent with that in the CX origin proposed by Tanaka et al. (2000), but coincides with that expected in the hot plasma.

Suzaku also gave a severe constraint for the Fe XXV $K\alpha$ line broadening of ≤ 30 eV. The intrinsic line broadening of Fe XXVI $K\alpha$ is nearly zero. On the assumption of the CX process, the velocity of the bare Fe is driven to be nearly zero. In such a case, emission lines at the Fe XXV Rydberg series of large principle quantum numbers ($n \leq 10$) are predicted, but no enhancement at the energy was observed in the GCDX spectrum. These observational facts indicate that the highly-ionized Fe lines come from the high temperature hot plasma with $kT \sim 6.5$ keV covering the $\sim 1^\circ$ centered region of the GC, hereafter the GC hot plasma (Koyama et al. 2007c).

1.3.3 GC Hot Plasma

Whether the GC hot plasma is truly diffuse or the integration of faint point sources have been under debate. White dwarf binaries (cataclysmic variables: CV) and active binaries (e.g. RS CVn) have thin thermal spectra with $kT =$ several keV, which is similar to that of the GC hot plasma. However, characteristic properties of X-ray spectra and distributions of the binary sources measured at the vicinity of the solar system does not explain the GC hot plasma (Yamauchi et al. 1990).

The $10'$ central region of the GC was observed with a excellent spacial resolution $\sim 0.5''$ of Chandra (Muno et al. 2003). More than two thousands point sources are resolved. The

lowest flux is 10^{-17} erg s $^{-1}$ cm $^{-2}$, which corresponds to that of a faint CV. The summed flux of the resolved point sources is only 10% of the flux of the total diffuse emission. However, Revnivtsev et al. (2007) re-analyzed the same Chandra data correcting the measured source counts at low fluxes for bias associated with Poisson noise and resolved more number of point sources, whose integrated flux contributes 40% of the total emission of the GC hot plasma. Revnivtsev et al. (2007) proposed that the GC hot plasma is completely divided into discrete sources including fainter CVs and active binaries than the detected ones.

Recently, Suzaku obtained a detailed intensity map in Fe XXV K α around the GC. Koyama et al. (2007c) found a difference between distributions of the Fe XXV K α flux and the total flux of the resolved discrete sources at $l = -0.4^\circ$ – $+0.2^\circ$ (see right panel in figure 1.5), and hence they suspected that the truly diffuse hot plasma should account at least some part of the GC hot plasma. Moreover, Koyama et al. (2009) separated the Suzaku data of the GCDX into $4.5' \times 4.5'$ sections to obtain positional variation of the Fe lines and continuum emission in the 5–10 keV band. The sum of the 6.4 keV and 6.7 keV line fluxes with a ratio of 1 : 2 showed good proportionality to the continuum flux, and hence the continuum flux of the GCDX was phenomenologically decomposed into the 6.4 keV- and 6.7 keV-associated continua with a flux ratio of 1 : 2. The results indicated that the contribution of integrated flux of point sources to the GCDX was $\sim 1/6$ (Koyama et al. 2009).

Each scenario has a problem. If the plasma is the integration of discrete sources, the Fe XXV K α equivalent width ~ 600 eV (e.g. Munro et al. 2003) of the GCDX cannot be explained only by known X-ray sources, such as CVs with a rather small value ~ 200 eV (Ezuka & Ishida 1999). This needs larger metal abundances than the solar value in the GC region or faint X-ray sources that have been invisible so far.

If the GC hot plasma is truly diffuse, it has an enormous amount of energy 10^{53} – 10^{54} erg, which corresponds to 100–1000 supernova explosions. In addition, the $kT = 6.5$ keV plasma is not bounded by gravitational potential of Milky Way Galaxy and runs away within about 10^5 years. A huge energy injection 10^{41} erg s $^{-1}$ is needed to sustain the diffuse hot plasma. Although the X-ray and radio observations have found about 10 supernova explosions for 10^4 years, the required energy injection is not explained. The results obtained by the past observations required that many undetected supernova remnants are buried in a heap of the hot plasma, or the super-massive black hole Sgr A* heated up the surrounding gases.

al. 1996; Murakami et al. 2001a, 2001b). The super-massive black hole, Sgr A* has been suspected to be the irradiating source (e.g. Sunyaev et al. 1993; Koyama et al. 1996). However, the present X-ray luminosity of Sgr A* is 10^{33} – 10^{34} erg s $^{-1}$ (Baganoff et al. 2001, 2003). Therefore, Sgr A* in a few hundred years ago would have been 10^{4-6} times brighter than now (e.g. Koyama et al. 1996).

On the other hand, Yusef-Zadeh et al. (2007) proposed that the origin of the 6.4 keV emission would be low energy cosmic-ray electrons (LECRE: $E_e = 10$ – 100 keV), because they found that the X-rays correlated with synchrotron-emitting radio filaments. Energy densities 20 – 10^3 eV cm $^{-3}$ of the electrons were estimated for the 6.4 keV emission in the Sgr B1, B2 and C regions. Yusef-Zadeh et al. (2007) also explained the cosmic-ray heating of molecular gas and TeV gamma-ray emission in the GC region. In particular, inverse Compton scattering of the sub-millimeter radiation from dust by the relativistic electrons may contribute substantially to the TeV gamma-ray emission.

In the XRN scenario, hard continuum X-rays should be generated due to the Thomson scattering of the incident external X-rays. The LECRe scenario also predicts a hard continuum of the bremsstrahlung by the relativistic electrons. In fact, the INTEGRAL satellite detected hard X-rays upto 100 keV from the Sgr B2 cloud. The hard X-ray spectrum agreed with the XRN model when the photon index of the incident X-rays and the optical depth of the cloud are $\Gamma = 1.8 \pm 0.2$ and $\tau = 0.4 \pm 0.1$, respectively (Revnivtsev et al. 2004). The X-ray luminosity in the hard X-ray band of the Sgr B2 cloud is $L_X \sim 10^{35}$ erg s $^{-1}$ (Revnivtsev et al. 2004). On the other hand, since only $\sim 10^{-5}$ of the energy of the relativistic electrons can go into hard X-ray radiation at ~ 50 keV, the total energy release of cosmic-ray electrons should be $> 10^{40}$ erg s $^{-1}$. The value is comparable to the bolometric luminosity of Sgr B2 mostly observed in infrared (Gordon et al. 1993), and hence the LECRe scenario seems to be unlikely (Revnivtsev et al. 2004).

1.4.2 Recent Results—time variability of X-ray emissions—

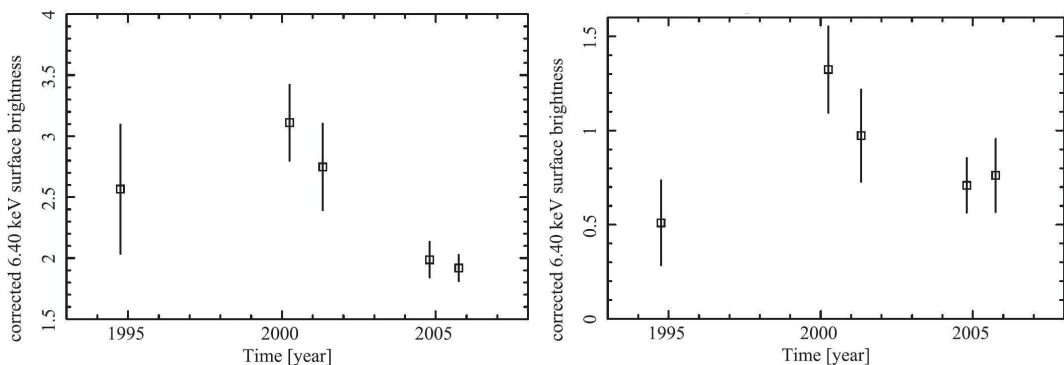


Figure 1.7: Left: Time variability of the 6.4 keV flux from the Sgr B2 clouds (M 0.66–0.02, Inui et al. 2009). The vertical axis means the surface brightness in the 6.4 keV line in the unit of photons s $^{-1}$ cm $^{-2}$ arcmin $^{-2}$. Right: Same as the left panel, but from G 0.570–0.018.

Thanks to the high sensitivity for extended faint sources of Suzaku, many new 6.4 keV clouds have been discovered in a variety of regions (Koyama et al. 2007b; Nobukawa et al. 2008; Fukuoka et al. 2009; Nakajima et al. 2009; Nakashima et al. 2010), and their X-ray spectra, in particular the Fe line, were well studied. Most of the 6.4 keV clouds have the strong 6.4 keV lines with large equivalent widths 1–2 keV and hard continua absorbed by dense media (photon index $\Gamma \sim 2$, absorption column density $N_{\text{H}} \geq 10^{23}$).

Koyama et al. (2008) and Inui et al. (2009) discovered time variability of the 6.4 keV flux in the Sgr B2 region from the archival data for 10 years obtained with Suzaku, XMM-Newton, Chandra, and ASCA. The 6.4 keV flux of the most brightest cloud Sgr B2 was $\sim 3 \times 10^{-6}$ photons $\text{s}^{-1} \text{cm}^{-2} \text{arcmin}^{-2}$ in 1994–2001, while that decreased to $\sim 2 \times 10^{-6}$ photons $\text{s}^{-1} \text{cm}^{-2} \text{arcmin}^{-2}$ in 2004–2005 (figure 1.7). The other spot, G 0.570–0.018, is found to be conspicuous only in the Chandra observation in 2000 (see figure 1.7).

Muno et al. (2007) also discovered the changes in the 4–8 keV fluxes and morphologies of the 6.4 keV clouds in the Radio Arc region from the Chandra observations in 2002–2005. The flux change of the 6.4 keV line of the 6.4 keV clouds was detected at the 5σ confidence level by the combination of the Chandra and Suzaku data (Koyama et al. 2009). Ponti et al. (2010) also studied the 6.4 keV clouds in the Radio Arc region using the XMM-Newton data in 2001–2009 with total exposure time ~ 1.2 Ms. Some of the clouds flickered in the 6.4 keV line as is shown in figure 1.8, while some of them showed constant luminosities.

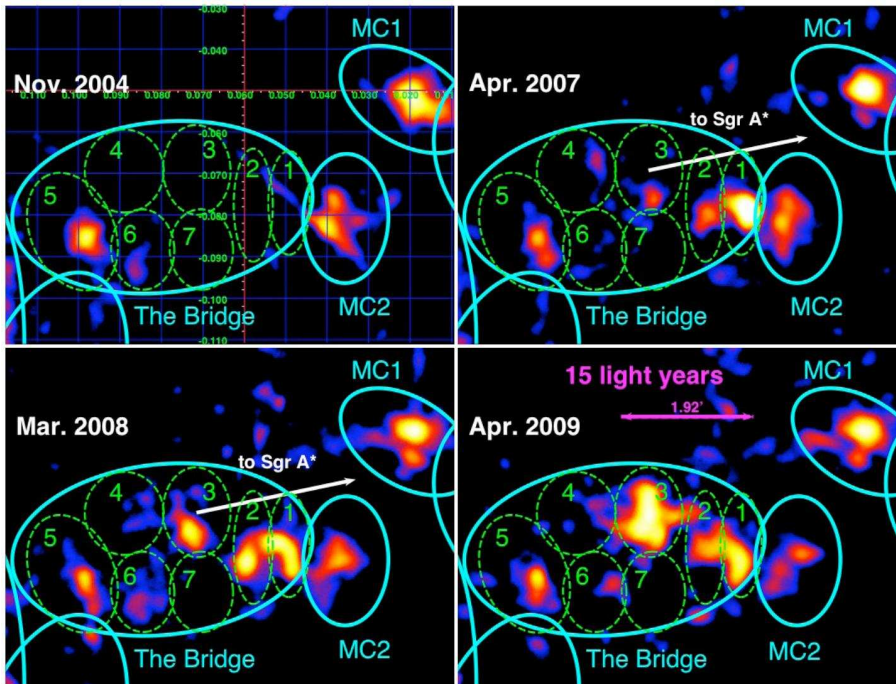


Figure 1.8: Fe I $K\alpha$ images obtained with the different XMM-Newton observations (Ponti et al. 2010). A brightening of the regions marked with numbers of 1, 2, 3, and 4 is clear.

An X-ray flux decrease from the Sgr B2 cloud also in the hard X-ray (20–60 keV) band was detected from the seven years monitoring data taken by INTEGRAL (Terrier et al. 2010). The characteristic time scale of the decay was ~ 8 years, comparable with the

light-travel time across the cloud core.

Since the variability over several years from a pc-scale object requires light-speed communication, these facts support the XRN scenario: X-rays from external sources irradiate molecular clouds and produce the fluorescence iron line at 6.4 keV and Thompson scattering continuum emission in the same manner. However, low-energy cosmic-ray electrons are not formally ruled out since the lifetime of ~ 100 keV electrons in the dense clouds is smaller than the measured decay time of several years, so that if the cosmic-ray injection had ceased with a similar or smaller timescale, we might obtain a similar flux decrease. We have left room for debating the origin of the 6.4 keV line from the GC region.

1.5 Aim of this thesis

In this thesis, we aim to examine the detailed features of the 6.4 keV emission and to reveal the origin.

1. Is the X-ray emission from the 6.4 keV clouds explained only by the X-ray reflection model, not by the low energy electron model?
2. What is the irradiating source of the 6.4 keV clouds?
3. How long and how bright was the Sgr A* flare in the past? (if it is the irradiating source.)

The detailed analyses and results for discrete sources are written in chapter 3, 4, and 5. Since the two processes should produced different X-ray spectra in principle, we can clearly distinguish the origin by the more detailed X-ray spectra. Although only the neutral Fe line has been detected so far, neutral K-shell lines of the other atoms should be emitted from the clouds. In chapter 3, we state a new constrain for the origin (XRN or LECRe) based on K-shell lines of several heavy elements that are newly discovered in this thesis. In chapter 4, we examined 6.4 keV clouds found in other regions and discussed the origins in detail. Previous observations indicated that the most plausible source irradiating the 6.4 keV clouds is the central super-massive black hole, Sgr A*. According to time variabilities of the 6.4 keV and hard X-rays from the two clouds in the Sgr B2 region, an unique constrain on the irradiating source is made in chapter 5. At the end of this thesis, we draw a conclusion for the 6.4 keV emission in the GC region on the basis of the the obtained results.

We use the Galactic coordinates in this thesis, where the transverse and vertical axes are the Galactic longitude and latitude. We also consider the positive and negative directions of the Galactic longitude as "east" and "west", respectively. In the same way, the positive and negative directions in the Galactic latitude are "north" and "south". Errors are estimated at the 90% confidence levels in this thesis, unless otherwise stated.

Chapter 2

Instrument: Suzaku X-ray Satellite

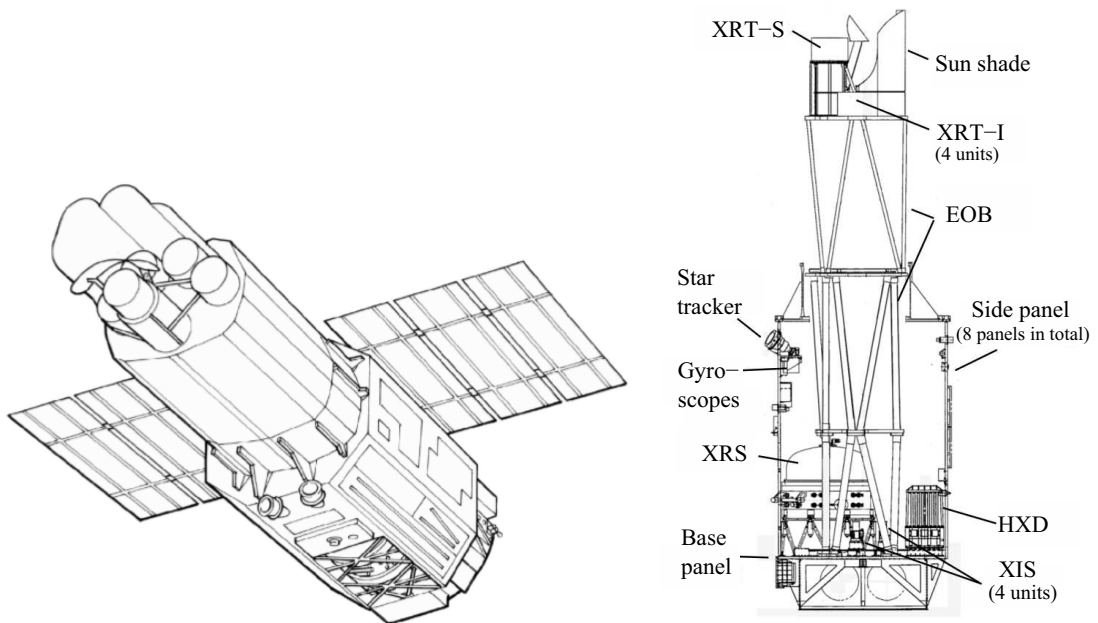


Figure 2.1: Left: Schematic view of the Suzaku satellite in orbit (Mitsuda et al. 2007). Right: Side view of the internal structure (Mitsuda et al. 2007).

For this work, we used data obtained with the X-ray Imaging Spectrometers (XIS: Koyama et al. 2007a) equipped on the focal plane of the X-Ray telescope (Serlemitsos et al. 2007) aboard the Suzaku X-ray satellite (Mitsuda et al. 2007). We introduce the overview and performances of the Suzaku satellite and the onboard instruments in this chapter.

2.1 Overview of the Suzaku Satellite

The Suzaku satellite, which is the fifth X-ray science satellite in Japan, was launched by Japan Aerospace Exploration Agency (JAXA) with the M-V Launch Vehicle from the JAXA's Uchinoura Space Center (USC) on 2005 July 10. The mission name before the launch was Astro-E2. The Suzaku satellite was developed by the Institute of Space and Astronautical Science of JAXA (ISAS/JAXA) in cooperation with the National Aeronautics and Space Administration's Goddard Space Flight Center (NASA/GSFC) and many other institutions.

The Suzaku satellite was carried into the ~ 570 km altitude orbit and is orbiting the Earth with the period of ~ 96 minutes and the inclination angle relative to the equator of 31° . The low altitude makes the significant advantage of the satellite of lower non-X-ray background (NXB) caused by cosmic-rays than the other X-ray satellite, Chandra and XMM-Newton, although efficiency of observation becomes relatively small ($\sim 43\%$) since the Earth occultation. Operations for observation, health check, and data acquisition are performed by communication with large parabola antennas with the diameters of 20 and 34 m in the USC 4 or 5 times per a day. Total communication time is about 50 minutes per one day.

The key feature of the Suzaku satellite is high sensitivity wide-band (0.2–600 keV) X-ray spectroscopy. The Suzaku satellite is equipped on the base plate with the three instruments of the high resolution X-ray spectrometer (X-Ray Spectrometer; XRS, 0.5–10 keV: Kelley et al. 2007), the X-ray imaging spectrometer (XIS, 0.2–12 keV), and the non-imaging collimated hard X-ray detector (Hard X-ray Detector; HXD, 10–600 keV: Takahashi et al. 2007; Kokubun et al. 2007). The arrangement of the instruments is shown in the right panel of figure 2.1. We concentrate the data taken by the XIS with the energy band of 0.2–12 keV in this thesis. The details of the XRT and the XIS are shown in the following sections.

2.2 X-Ray Telescope (XRT)

In order to collect X-rays and to take X-ray images in the < 10 keV band, five sets of the XRT are mounted at the top of the satellite (Serlemitsos et al. 2007). One unit (XRT-S) is used for the XRS and the others (XRT-I0 to XRT-I3) are for the XIS (see figure 2.1).

Design

Since refractive indices of matter to X-rays is less than 1, X-rays cannot be focused by a refracting telescope. X-rays are full-reflected if the incident grazing angle is shallow enough ($\leq 1^\circ$), and thus X-rays are focused using this full-reflection.

An approximate the Wolter type-I optics is used in the XRT. The XRT is the thin-foil-nested X-ray telescope consisting of many concentric thin reflecting mirrors of thin aluminum foils coated with gold. The shape of the reflecting foils are not complete paraboloid but are approximated by cones in the Wolter type I grazing incident optics (figure 2.3).



Figure 2.2: X-ray telescope onboard the Suzaku satellite (Serlemitsos et al. 2007).

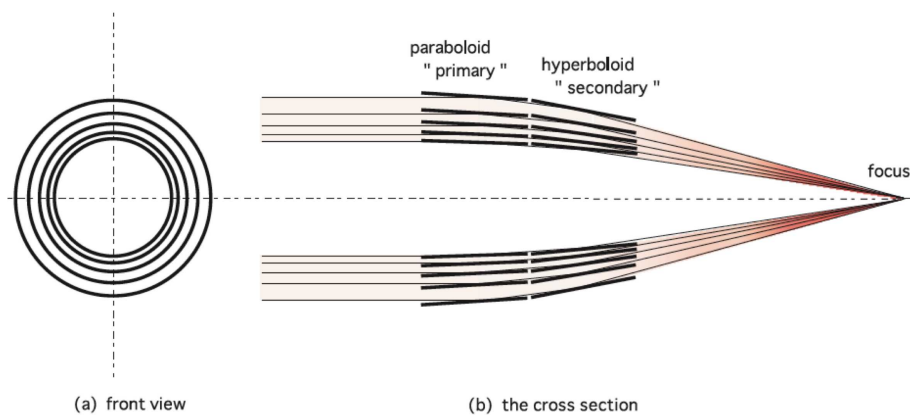


Figure 2.3: Schematic view of an X-ray telescope composed of nested mirror shells with a Wolter type-I grazing incident optics. This figures are adopted from Mori et al. (2005).

X-rays are reflected twice on the surface of the primary and secondary reflectors and are collected on the focal plane. The XRT is basically the same as the X-ray telescope onboard the ASCA satellite (Serlemitsos et al. 1995), while the following major improvements were made.

The incident grazing angle has been reduced to be $\leq 0.6^\circ$ and the diameter of the XRT has increased from ~ 350 mm to ~ 400 mm. As a result, the effective area especially in the higher energy band than that of Fe-K lines (6–7 keV) has been significantly improved since X-rays with the higher energy can be collected than by the ASCA/XRT. The focal length also changed to be from 3.5 m to 4.5 (for XRS) and 4.75 m (for XIS).

The ASCA reflectors were made by coating acrylic lacquer on the aluminum foils followed by vacuum deposition of a gold layer on the top. The surface of the foils was not smooth sufficiently, resulting in the image broadening. For the Suzaku XRT, the gold layer was sputtered onto the glass tube of a highly smooth surface, and was transferred to the foil reflectors. A half power diameter (HPD) is the diameter of a circle which contains 50% of flux of a point source. The change of the fabricating method made the HPD from $\sim 3.6'$ (ASCA) to $\sim 2.0'$ (Suzaku).

X-rays from the field of view (FOV) are properly focused when they are reflected by the two surfaces. If X-rays from the outside of the FOV are reflected only by one surface or by the backside of the mirrors, an incorrect X-ray image appears on the focal plane (stray light). To avoid the stray light, a pre-collimator is equipped on the top of the XRT.

The entrance of the XRT is covered with a thermal shield in order to isolate the XRT thermally from the space and to keep the temperature within the specified range of 20 ± 7.5 °C. The thermal shield also works to block optical light from the sky and from the surface of the Earth illuminated by the Sun.

Performance

The XRT has light-weight of ~ 20 kg and large effective area (450 cm² at 1.5 keV, 250 cm² at 7 keV) per one unit. Since the four sets of the XRT-I modules point to the same direction, the total effective area is calculated by summing those of all the XRT. Figure 2.4 shows the total effective area including the detector efficiency, compared with those of the Chandra and XMM-Newton satellites. Although the total weight of the XRT is at least 80 kg, the effective area at 7 keV is comparable to that of the XMM-Newton mirrors, which has the total weight of ~ 1300 kg. On the other hand, the spacial resolution (HPD) of $\sim 2'$ is larger than the other X-ray telescopes onboard the other active satellites, Chandra (High resolution mirror array: ~ 1500 kg) and XMM-Newton by about one order of magnitude since the design philosophy of the XRT is to achieve the the better spectral power, especially in the 6–10 keV band including Fe-K lines in the confines of a severe weight limit due to the launch vehicle.

The HPDs of the XRTs are $1'.8$ – $2'.3$. Point spread function (PSF) is an intensity profile of a point source as a function of radius from the point source. Enclosed energy function (EEF) is a integration of PSF and shows the ratio of the flux of the enclosed circle to the total flux of a point source. PSF and EEF of one of the XRTs are shown in figure 2.5.

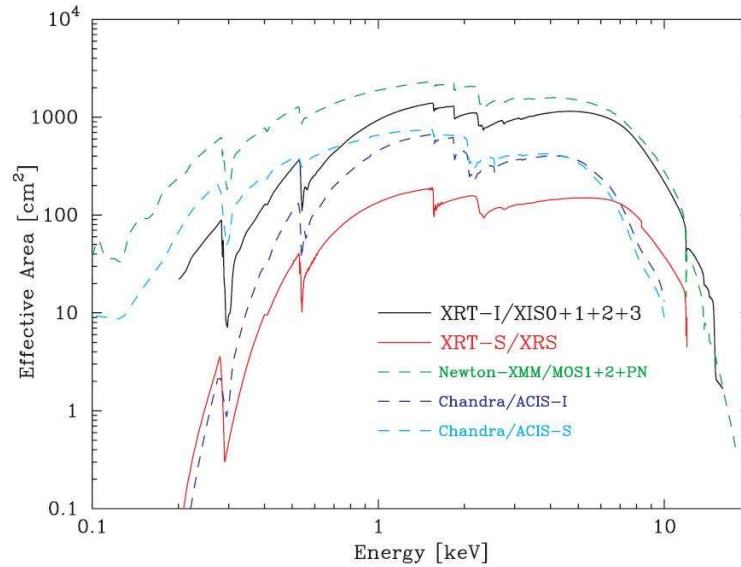


Figure 2.4: Effective areas of the Suzaku XRT, compared with the other telescopes onboard the Chandra and XMM-Newton satellites (Serlemitsos et al. 2007).

Tightly-nested structures increases the possibility of reflection other than the normal double reflection within the telescope structure. Because of these unexpected incidences, X-ray of bright sources outside the field of view reaches the focal plane (stray light). This has been a large problem for nested X-ray telescopes (e.g. ASCA/XRT).

The effective area for off-axis incident X-rays is smaller than that for on-axis X-rays because off-axis X-rays are partially obscured by neighbor mirror shells. This "vignetting" effect is prominent at high energy. A maximum incident angle for full-reflection is smaller for higher energy X-rays than for lower ones. High energy X-rays are reflected only at inner mirror shells, where the cone angles is small and the mirror shells are tightly packed (see figure 2.3), and highly subject to shadowing. The off-axis angle dependencies of the effective area for the soft (3–6 keV) and the hard (8–10 keV) bands are shown in figure 2.6.

Figure 2.8 shows the wide-band vignetting function of the XRT. The stray light (the secondary reflection) dominants at the off-axis angle of $20'$ – $70'$. The pre-collimator successfully reduces the stray light although some portion in the off-axis angle of $\sim 20'$ and $60'$ – $70'$ is not completely diminished.

From real data taken by observations of the Crab Nebula, optical axes of the four XRT-I modules were measured to scatter within $\sim 1.3'$. The observation efficiency of the XRT is more than 97% even at the high energy limit of 8–10 keV.

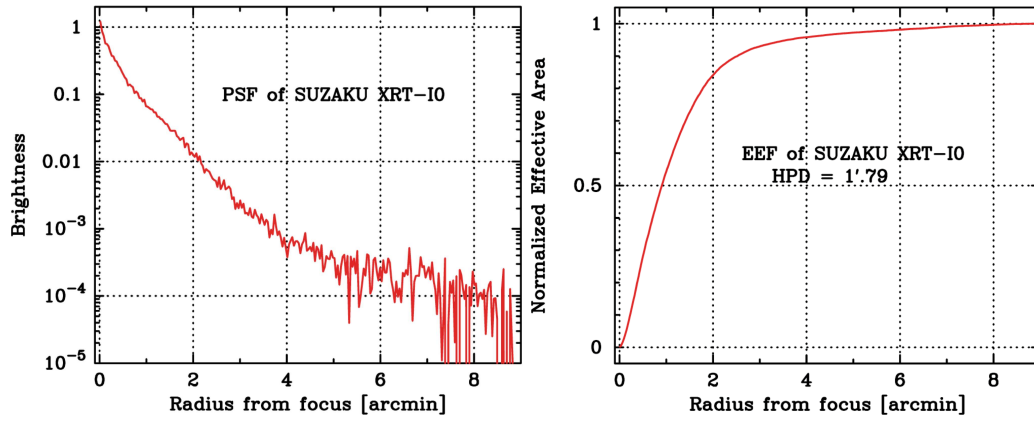


Figure 2.5: Left: Point spread function (PSF) of the XRT of XIS 0 (Serlemitsos et al. 2007). This is obtained with the observation of SS Cyg, which is a bright point-like source. Right: Enclosed energy function XRT of XIS 0 (Serlemitsos et al. 2007). This is obtained with the integration of the PSF in the left panel.

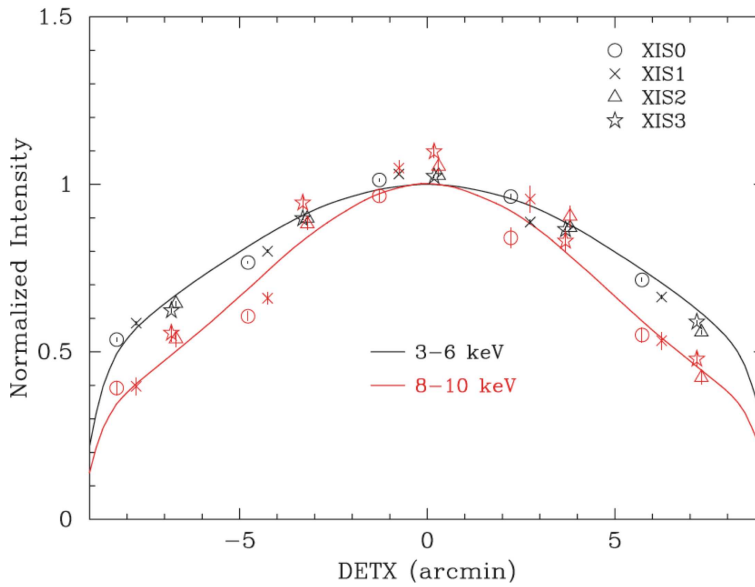


Figure 2.6: Off-axis angle dependence of the effective area normalized at the optical axes (Serlemitsos et al. 2007). The black and red points shows those in the soft and hard bands obtained with the Crab nebula observations, respectively (vignetting). The solid lines show the simulated models.

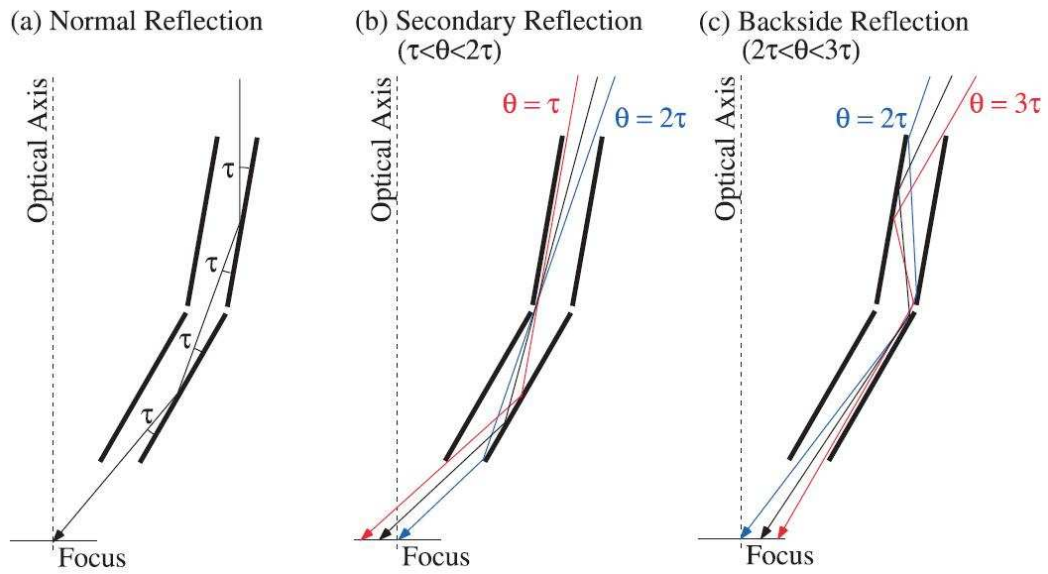


Figure 2.7: Major reflection paths occurring in the XRT. τ represents the oblique angle of the primary reflectors measured from the optical axis (Serlemitsos et al. 2007). (a) Normal double reflection of the X-rays arriving from the on-axis direction. Incident X-rays are bent by an angle of 4τ in total. (b) Secondary reflection: an X-ray arrives at the focal plane only if the incident angle θ measured from the optical axis is in the range of $\tau < \theta < 2\tau$. (c) Stray-light path that gives rise to the brightest ghost among various backside reflections. The pattern occurs then the X-ray incident angle is in the range of $2\tau < \theta < 3\tau$.

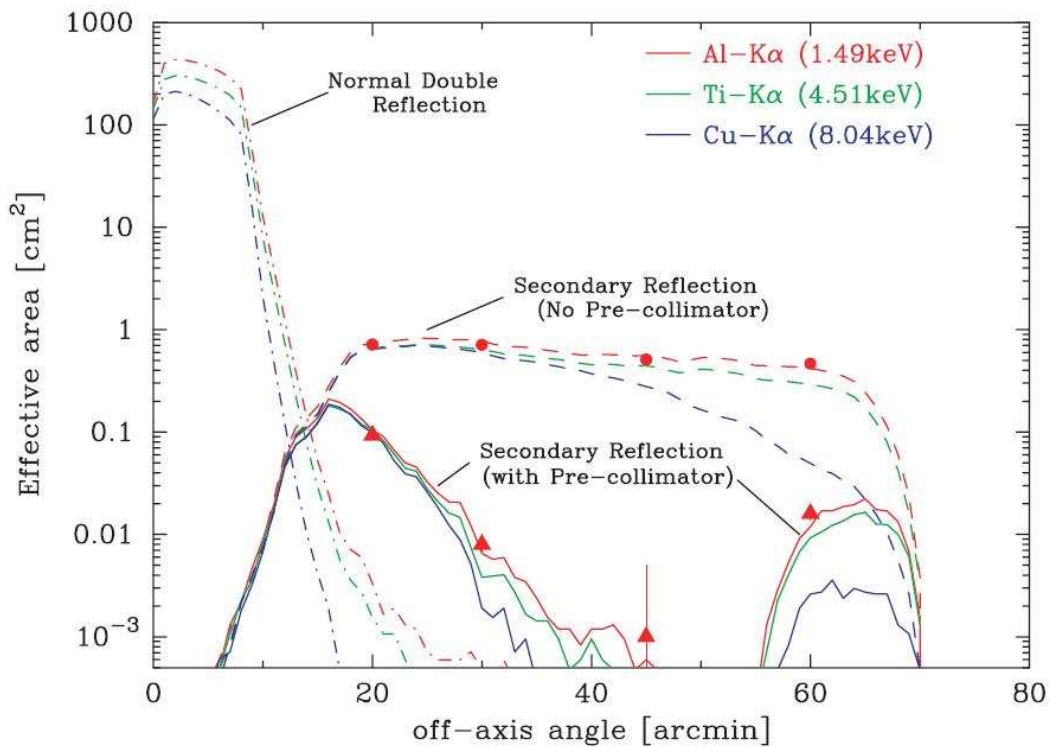


Figure 2.8: Wide-range vignetting function of the XRT at the three energies of Al-K α (1.49 keV), Ti-K α (4.51 keV), and Cu-K α (8.04 keV) for off-axis angles up to 80' (Mori et al. 2005). The circles and triangles are the measured stray effective area at 1.49 keV before and after installation of the pre-collimator, respectively. The continuous and dashed curves are the effective areas of the secondary reflection with and without the pre-collimator, respectively, while the dash-dotted curves are those of the normal double reflection. All of the curves were simulated by the ray-tracing program.

2.3 X-Ray Imaging Spectrometer (XIS)

2.3.1 Introduction of X-ray Charge Coupled Device Cameras

The XIS consists of MOS-type charge coupled devices (CCDs). An X-ray CCD is a silicon semiconductor detector with two-dimensional imaging capability. Each pixel consists of Metal (poly-silicon) and Oxide (SiO_2) as an insulator and p-type semiconductor (silicon). This is called a MOS structure (figure 2.9).

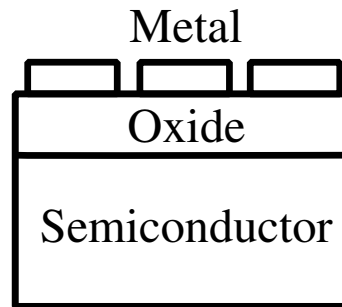


Figure 2.9: Schematic view of a MOS structure.

The principle of an X-ray CCD is briefly explained in the following. In a p-type semiconductor, holes are the major carriers. A positive voltage applied to the metal electrodes repels holes in the semiconductor and leaves behind a depleted layer where an electric field exists. When an X-ray photon enters into a pixel, photo-electrons are created and then electron-hole pairs are generated. The number of the generated electrons is proportional to the energy of the incident photon. The average energy required to form an electron-hole pair is 3.65 eV at -90°C . The holes and electrons are separated by the electronic field in the depletion layer before they recombine. The electrons are collected into the potential wells beneath the electrodes as signal charges. After the exposure period, the signal charges are transferred to the readout node by clocking the voltages of the electrodes.

The CCDs of the XIS employ the three-phase transfer type electrode structure. As shown in left panel of figure 2.10, in this type, three electrodes are deposited on each pixel. By applying the three-phase clock voltage to the electrodes, the potentials beneath the electrodes change periodically and the signal charges are transferred.

The CCD of the XIS is classified as a frame transfer (FT) CCD in the scheme of the charge transfer and readout. A FT CCD consists of an imaging area and a frame-store region shown in right panel of figure 2.10. The imaging area is exposed but the frame-stored region is shielded from X-rays. After the exposure period, the signal charges are transferred in a short time from the imaging area to the frame-store region. The signal charges in the frame-store region are transferred vertically to the horizontal shift register by each row. The charges in the horizontal shift register are transferred to the readout node by each pixel. This process is repeated until the charges in all the pixels of the frame-store are read out. When the charges are transferred to the frame-store area, new

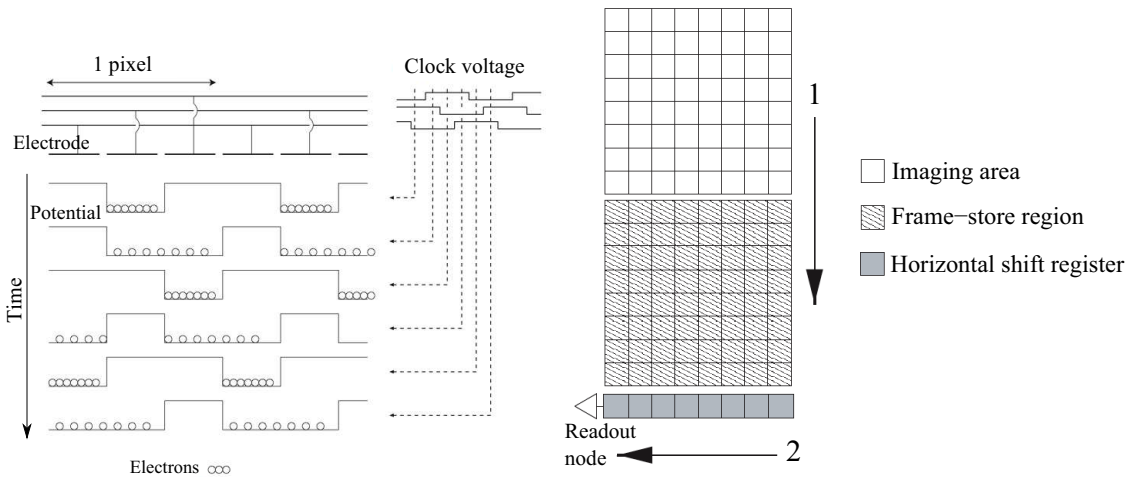


Figure 2.10: Schematic view of three phase transfer (left panel) and frame transfer (right panel) in a CCD (Takagi et al. 2006)

exposure starts in the imaging area. The exposures and readouts are made continuously.

In this way, amounts of charges in each pixel are measured and an image and a spectrum are taken with an X-ray CCD camera. An X-ray CCD camera has also time resolution depending on the exposure cycle.

2.3.2 Overview of XIS

The XIS is an X-ray CCD camera system which can take image, spectral and photometrical data in the 0.2–12 keV band. The XIS has four sensors (XIS 0, 1, 2, and 3). Each sensor consists of one CCD chip and a camera body. A photograph and the cross section of one of the XIS sensors (CCD + camera body) are shown in figure 2.11.

The CCD chip of the XIS is a MOS-type three-phase FT CCD. A photograph and the schematic view of the CCD is shown in figure 2.12 and 2.13. The CCD chips of the XIS are fabricated by the Lincoln Laboratory of MIT and basically same as those of ACIS/Chandra (Burke et al. 2007) except for a charge injection structure. The details of the charge injection structure are found in the following section 2.3.3.

The CCD has imaging and frame-store areas with 1024×1024 pixels (figure 2.13). The signals are transferred down in figure 2.13. The pixel sizes of the imaging area and the frame-store region are $24 \mu\text{m} \times 24 \mu\text{m}$ and $21 \mu\text{m} \times 13.5 \mu\text{m}$, respectively. In the imaging area, one pixel and the entire field of view correspond to $1''.04 \times 1''.04$ and $17'.8 \times 17'.8$, respectively, combined with the XRT whose focal length is 4.75 m. Note that the spatial resolution of the XIS for celestial objects is determined by not the pixel size of the XIS but the imaging capability of the XRT.

Each CCD chip is divided into four segments (from A to D) and each segment has one readout node. One of the CCD chips (XIS 1) is a back-illuminated type (BI) and the others are a front-illuminated type (FI). The front side of a CCD has a structure of electrode and insulator (“gate” structure) made of poly-Si and SiO_2 layers. The thicknesses of the

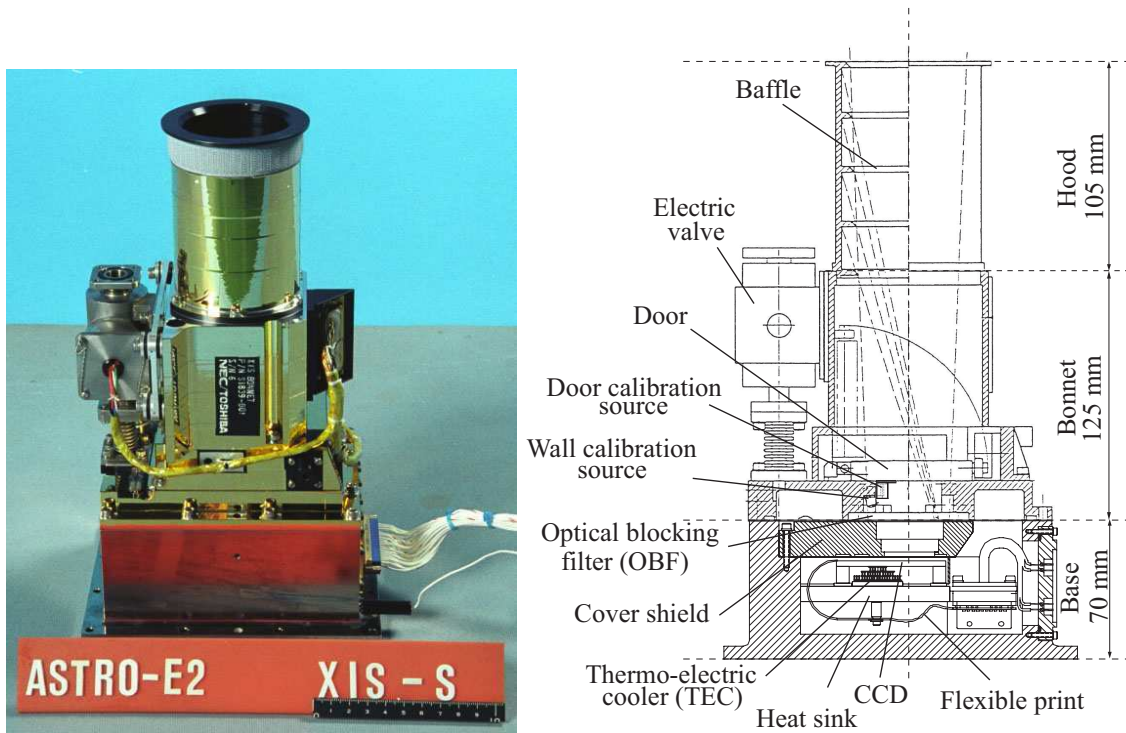


Figure 2.11: X-ray Imaging Spectrometer (Koyama et al. 2007a). Left panel: Picture of one of the XIS sensors. Right panel: Cross section of the XIS sensor.

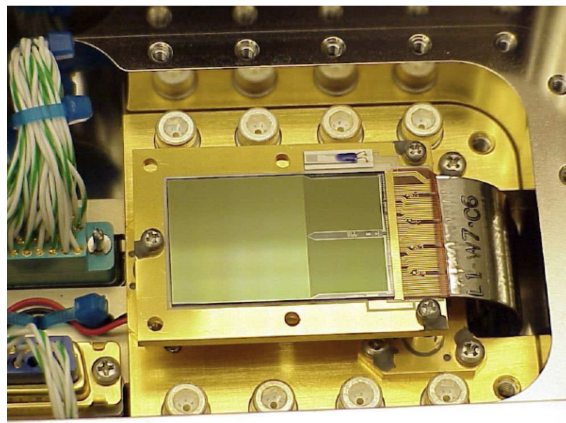


Figure 2.12: Picture of the CCD installed in the base (Koyama et al. 2007a).

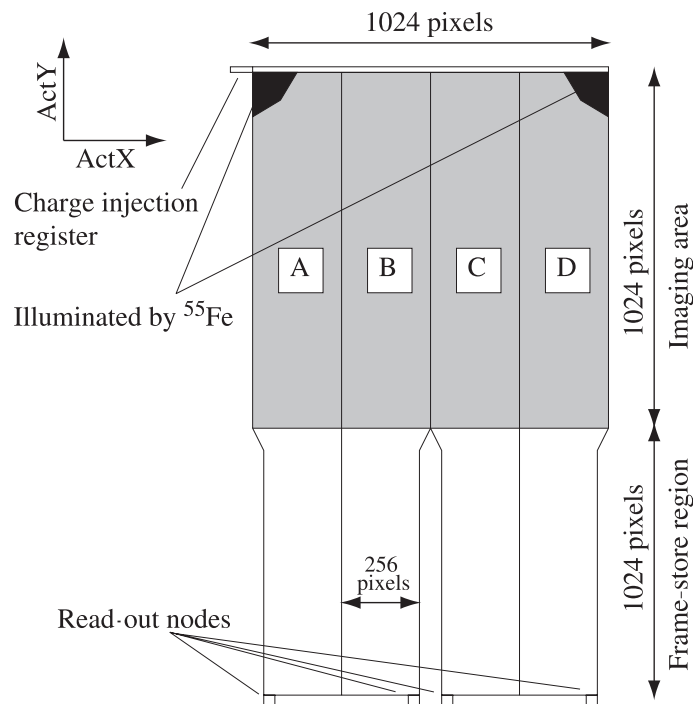


Figure 2.13: Schematic view of the XIS CCD (Koyama et al. 2007a). The CCD consists of four segments (A, B, C, and D), each with a dedicated read-out node. An incident X-ray is received on the top half of the CCD (imaging area). The signal charge corresponding to the incident X-ray is transferred to the bottom half (frame-store area). The attached calibration source irradiates the top corners with Mn I K lines (5.895 and 6.49 keV X-rays). The charge injection register is equipped at the top of the imaging area.

poly-Si and SiO₂ layers are $\sim 0.28 \mu\text{m}$ and $\sim 0.44 \mu\text{m}$ in the case of the XIS. The FI CCD is less sensitive than the BI CCD to X-rays in the $<2 \text{ keV}$ band since the gate structure absorbs soft incident X-rays. On the other hand, the depletion layer of the FI CCD is thicker ($\sim 65 \mu\text{m}$) than that of the BI CCD ($\sim 42 \mu\text{m}$) and thus the FI CCD has high quantum efficiency to hard X-rays than the BI CCD.

For the in-orbit calibration, radiative isotopes ^{55}Fe are equipped (“Wall calibration source” in figure 2.11). They emit the Mn I $K\alpha$ (5.895 keV) and $K\beta$ (6.492 keV) lines to the upper edge of the segment A and D constantly (see figure 2.13).

The CCDs of the XIS are operated at a temperature of -90°C cooled by radiators and Peltier coolers. Each XIS has an optical blocking filter (OBF) to block optical and UV photons. The OBF is made of 100 nm polyimide coated with Al of a 120 nm thickness.

XIS 2 suddenly showed an anomaly on November 9, 2006, and it has not been operated since then. Although there is no direct evidence, the micro-meteoroid impact might have caused the anomaly ¹.

2.3.3 Charge Injection Capability

The XIS is equipped with the CI structure for the first time among the satellite-onboard CCD cameras. A charge injection (CI) structure is installed adjacent to the topmost row of the imaging area. The CI structure allows us to inject an arbitrary amount of charge in a nearly arbitrary spatial pattern. The CI has been used in two ways to mitigate the effect of the radiation damage in orbit; checker-flag CI (CFCI) and spaced-row CI (SCI) techniques. The CI function is important to analyze the data used in this thesis because the difference of the observation dates are up to three and half years. Generally, systematic errors from a time degradation of a CCD become serious problems for such data sets. In the case of the XIS data used in this thesis, however, such systematic errors are small due to these CI techniques.

The function of the CI is described in figure 2.14. A serial CI register of 1024 pixels long is attached next to the upper edge of the imaging area. An input gate is equipped left of the CI register (figure 2.14). Pulling down the potential for electrons at the input gate and the next electrode (S3 in right panel of figure 2.14), the potential well is filled with charges with an amount of Q . Then, pulling up the potential makes the charges to be spilled. The amount of charges is controlled by the offset voltage between the input gate and the next electrode (S3). It can inject charges from $\sim 50 e^-$ to $\sim 4000 e^-$ per pixel; the equivalent X-ray energies range from $\sim 300 \text{ eV}$ to $\sim 15 \text{ keV}$. The deposited charges are transferred horizontally through the serial CI register, vertically through transferred into the imaging area, and to an arbitrary position of the CCD chip. Prigozhin et al. (2008) have reported details concerning the CI structure.

X-ray CCDs suffer from radiation damage in orbit. The damage causes the increase of the charge transfer inefficiency (CTI) which is defined as the ratio of lost charges to transferred charges in one pixel by one transfer. This causes decrease of gain and degradation of energy resolution.

¹See http://www.astro.isas.jaxa.jp/suzaku/proposal/ao3/suzaku_td/ and similar micro-meteoroid impact events of XMM-Newton are reported by Strüder et al. (2001)

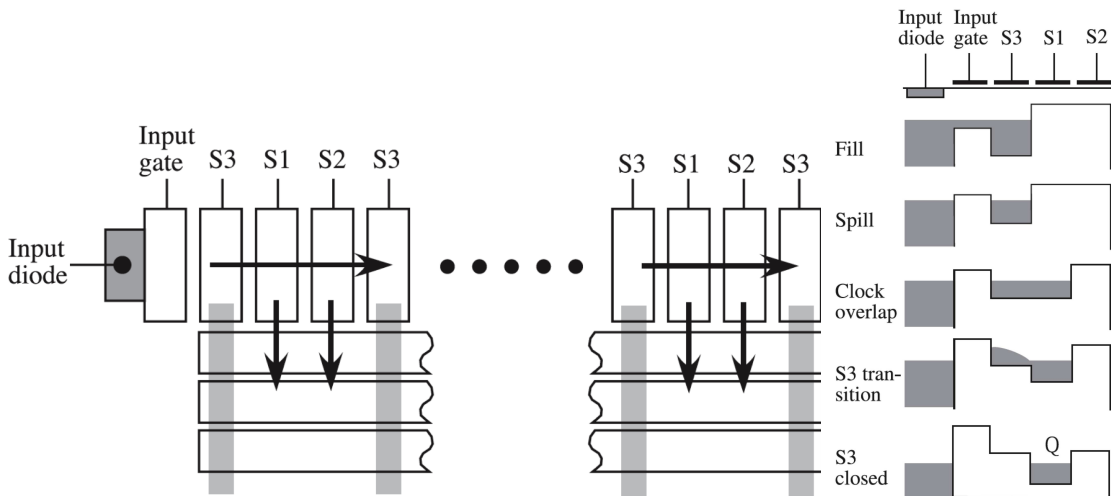


Figure 2.14: Schematic view of the charge injection (CI) technique (Bautz et al. 2004). Left: CI structure. Charge packets are injected to the charge-injection register from an input gate located at the edge of the register. After depositing the packets over the register, a vertical clock runs to inject the packets into the imaging area. Right: Schematic view for the injection of charges at the input gate. The offset voltage between the input gate and the S3 electrode can control the amount of injected charge (Q).

The main origin of the CTI is thought to be the increase of defects in the crystal lattice generated by cosmic-rays in orbit. These defects form charge traps that can capture signal electrons. The CTI results in the degradation of the determination accuracy of the energy and the energy resolution for two reasons: (1) the pulse height strongly depends on the position of an X-ray event, since the X-ray event loses more electric charges as the number of transfer increases, and (2) the loss of charge is a stochastic process, and thus there is a fluctuation in the amount of lost charge.

Checker-Flag Charge Injection

One strategy to mitigate the effect of the CTI is to measure the CTI of each column precisely and correct the lost charges. Here the "column" is defined as the vertical column of the pixels along the ACTY in figure 2.13. The checker-flag CI (CFCI) technique makes the column-to-column CTI measurement possible. Here the outline of the CFCI technique is described referring figure 2.15. First, a "test" charge packet is injected into the top CCD row. Then, after a gap of a few rows, five continuous packets are injected with the same amount of charge of the test packet. The former four packets are called "sacrificial" charge packets, while the last one is called a "reference" charge packet. The test packet loses its charge by charge traps. On the other hand, the reference packet does not suffer from any charge loss, because the traps are already filled by the preceding sacrificial charges. Thus, we can measure the CTI of each column by comparing the pulse heights of the reference charge and the test charge.

Using the obtained CTI values, the column-to-column CTI correction is applied for the

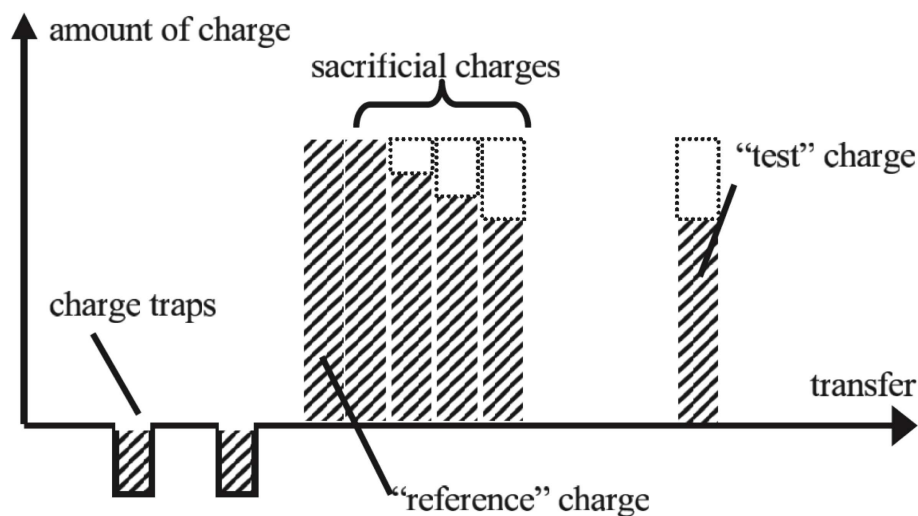


Figure 2.15: Schematic view of measuring procedure of CTI with the CFCI technique (Nakajima et al. 2008). The amount of lost charge (δQ) can be estimated by comparing the PHA of the test packet, which suffers from CTI, to that of the reference packet, which is not affected by the traps.

data observed between the launch and September 2006. The energy resolution of the FI CCD at 5.9 keV was ~ 140 eV (FWHM) at August 2005, and had degraded to ~ 200 eV at August 2006 without the column-to-column CTI correction. The column-to-column CTI correction improves the energy resolution to ~ 170 eV (FWHM) at August 2006. Nakajima et al. (2008) and Ozawa et al. (2009) reported the details of the CFCI in orbit and the column-to-column correction.

However, we cannot correct the fluctuation by the readout-to-readout in a specific column, which still degrades energy resolution even after the column-to-column CTI correction in principle.

Spaced-row Charge Injection

The spaced-row charge injection (SCI) technique can reduce the CTI actively and improve the energy resolution. In the SCI mode, a charge packet is injected into CCD rows periodically during the observation. The injected charge fills the radiation-induced traps as a sacrificial charge packet, and thus prevents some of the traps from capturing signal charges produced by X-rays. Results based on ground experiments using the SCI technique with radiation-damaged CCDs have been reported by Tomida et al. (1997) and Bautz et al. (2004), but no in-orbit experiment had been done.

The Suzaku XIS operated with the SCI technique in orbit for the first time from August 2006. In the SCI mode of the XIS, a charge is injected into every 54th row. The amounts of the injected charge into each pixel are equivalent to the X-ray energy of ~ 6 keV and of ~ 2 keV, for the FI and BI, respectively. The energy resolution was improved from ~ 200 eV to ~ 140 eV at 5.9 keV (Bautz et al. 2007). The SCI has been applied in a normal observation since October 2006 (the SCI mode). In the SCI mode, since the CTI

depends on the distance from a charge injected row, the pulse heights show a sawtooth distribution depending on the transfer number shown in figure 2.16. This non-uniformity of the pulse heights degrades the determination accuracy of the energy and the energy resolution. Thus we developed a new CTI correction method for the SCI mode, which is called a “sawtooth” CTI correction. This method corrects the non-uniformity like shown in figure 2.16. All the XIS data of the SCI mode are processed with the sawtooth correction. The details of the sawtooth correction and CTI measurement method for the SCI mode are described in Uchiyama et al. (2009).

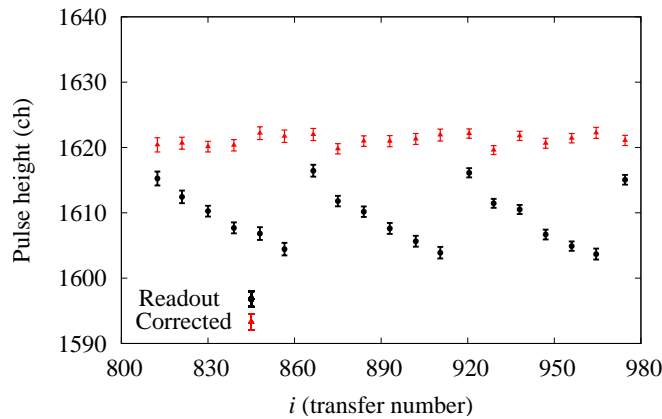


Figure 2.16: Relation between pulse height of the Mn I $K\alpha$ line from the onboard calibration source and transfer number i : This is the data of February 2008. Black and red marks are data before and after our new CTI correction, respectively (Uchiyama et al. 2009).

2.3.4 XIS Performance in orbit

Determination Accuracy of the Energy Scale

Figure 2.17 shows the time histories of the center energy of the Mn I $K\alpha$ line obtained with the onboard calibration sources. These data are processed with the column-to-column CTI correction for the SCI-off data or the saw-tooth CTI correction for the SCI-on data. The center energy of the Mn I $K\alpha$ line have been constantly 5.895 keV. The uncertainty of the energy-scale determination is less than ~ 20 eV (0.3%) at 5.9 keV.

Figure 2.18 shows the time histories of the center energy of the O VII $K\alpha$ line (0.570 keV) obtained from 1E0102-7219, which is a well-studied supernovae remnant and commonly used as a celestial calibration source for X-ray astronomical satellites recently. Narrow lines from 1E0102-7219 were resolved with the grating spectrometer on XMM-Newton (see Rasmussen et al. (2001) and Plucinsky et al. (2008) in detail). The uncertainty of energy-scale determination of the XIS is less than ~ 10 eV (1–2%) at 0.5–1 keV.

There is no good celestial calibration source for the 1.5–3 keV band, and the gain and response functions may jump at the Si-K edge (1.839 keV). Therefore, the relatively

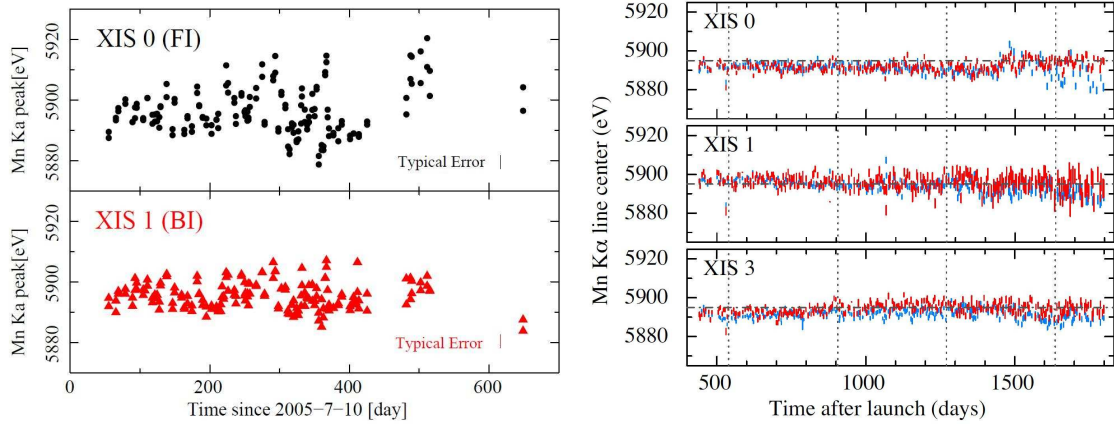


Figure 2.17: Time histories of the CTI-corrected central energy of the Mn I $K\alpha$ line from the ^{55}Fe calibration sources for XIS 0 (FI) and XIS 1 (BI). The left and right figures show data taken in the SCI-off (Ozawa et al. 2009) and SCI-on (Uchiyama et al. 2009) modes, respectively.

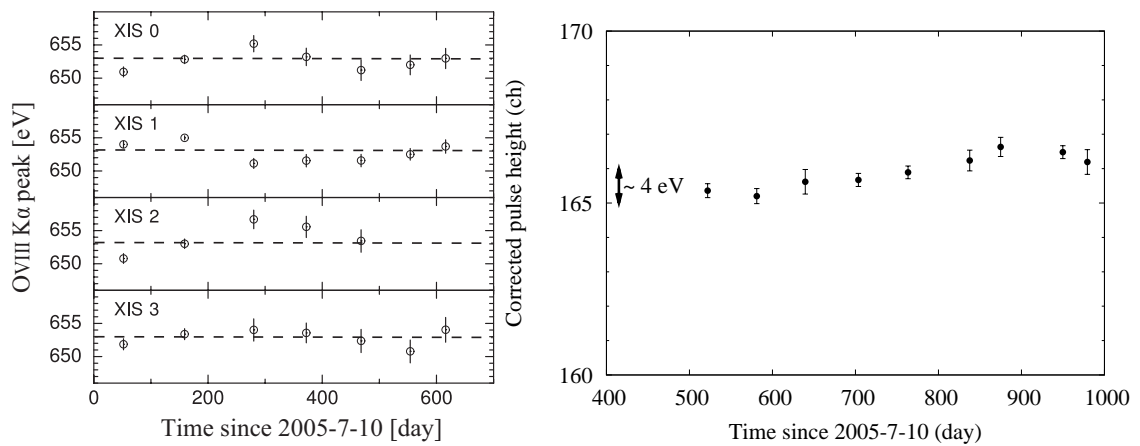


Figure 2.18: Time histories of the center energy of the O VII $K\alpha$ of 1E 0102.2-7219. Left: SCI-off mode (Ozawa et al. 2009). Right: SCI-on mode, where the center energy is described in the unit of pulse height channel and the result of XIS 1 is shown (Uchiyama et al. 2009).

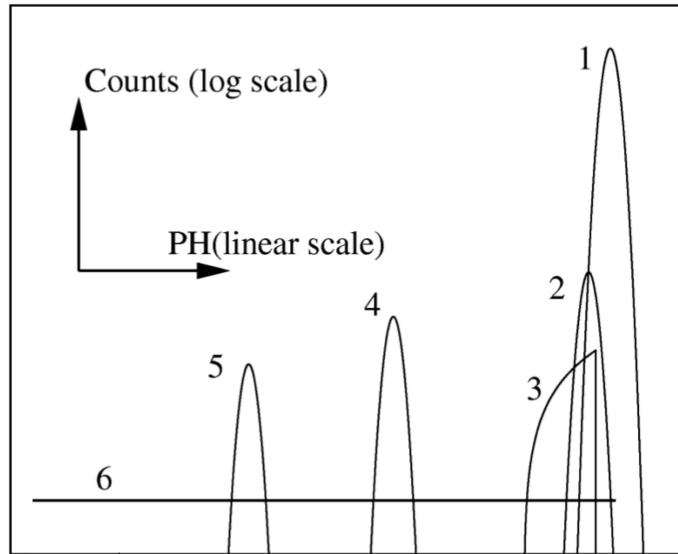


Figure 2.19: Schematic response function of the XIS. 1. main peak, 2. sub peak, 3. triangle component, 4. Si escape, 5. Si K α line, and 6. constant component. The physical interpretation of the each component is shown in Matsumoto et al. (2006).

large uncertainty remains in the band. Recent studies of SNRs using the XIS show the energy-scale determination in the 1.5–3 keV can have the systematic error of 20–30 eV (1–2%).

Response and Energy Resolution

The pulse height distribution of the signals for a monochromatic incident X-ray energy is called a response function of the detector. The schematic response function of the XIS is shown in figure 2.19. The main-peak component is made by complete-gathered signal charges. The sub-peak, triangle and constant components come from events some of which charges are lost. The Si escape line happens when a fluorescent Si X-ray photon generated by a photoelectric absorption escapes. The Si K α line also occurs when the fluorescent Si photon is absorbed in an other pixel. The details of physical interpretations of the response function are reported by Matsumoto et al. (2006).

The energy resolution of the XIS is defined as the width of the main peak. The time history of the widths of Mn I K α from the onboard calibration sources is shown in figure 2.20. The intrinsic width of the Mn I K α line is almost 0 eV, although, strictly speaking, since this line is a blend of Mn K I α_1 5.888 keV and α_2 5.899 keV, the width of the merged Mn I K α is a few eV. Figure 2.20 shows the time histories of the energy resolution at 5.9 keV. The energy resolution of the BI has degraded more rapidly than that of the FI in the SCI mode. This may be caused by difference of the amount of the injected charges.

The time history of the energy resolution at 0.57 keV (O VII K α) is shown in figure 2.21. This figure is obtained with the observations of 1E0102.2-7219. The calibration database for the XIS includes these time history of the energy resolution properly.

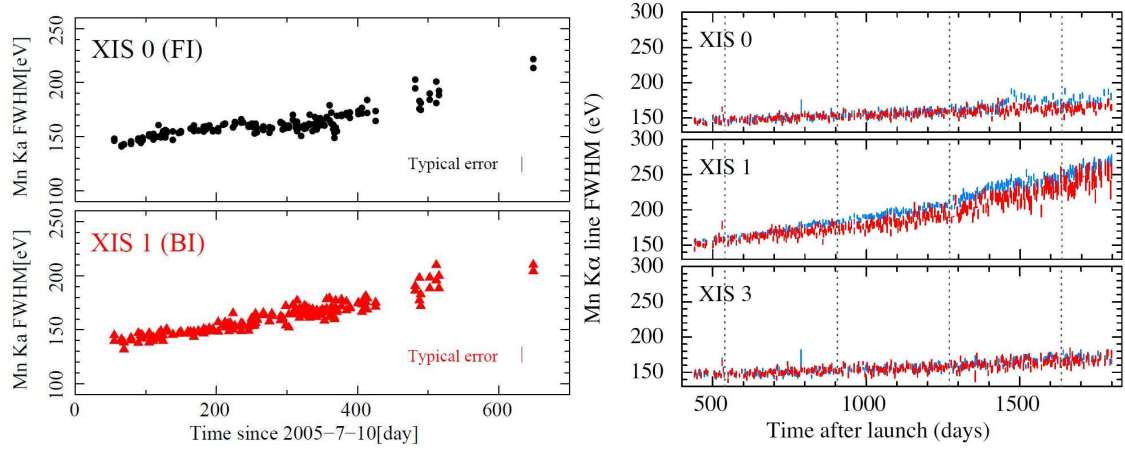


Figure 2.20: Time histories of the width of the Mn I $K\alpha$ line obtained with the onboard calibration sources. Left: in the SCI-off mode (Ozawa et al. 2009). Right: in the SCI-on mode (Uchiyama et al. 2009).

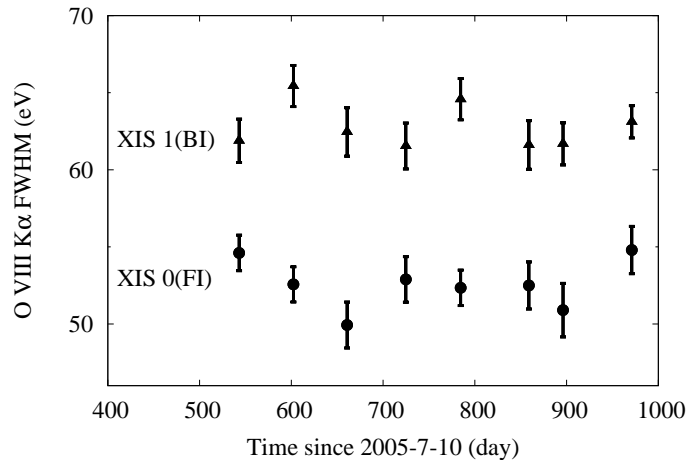


Figure 2.21: Time history of the line widths of the O VII $K\alpha$ obtained with the onboard calibration sources in the SCI-on mode (Uchiyama et al. 2009).

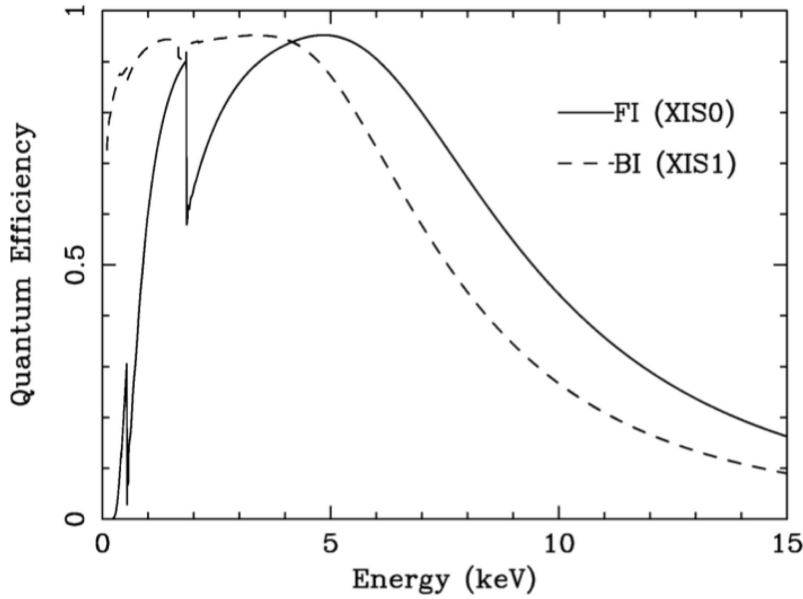


Figure 2.22: Quantum efficiency of the XIS sensor as a function of incident energy (Koyama et al. 2007a). The solid and dashed lines indicate the FI and BI CCDs, respectively.

Quantum Efficiency and Effective Area

Conversion efficiency of an incident X-ray photon to an detected X-ray event is called quantum efficiency (QE), as we shown in figure 2.22. The difference of the QEs between the FI and the BI comes from the illumination type and the thickness of the depletion layers.

The QE in the low energy band has degraded by unexpected contamination (due to out-gassing from the satellite) accumulating on the OBF (Koyama et al. 2007a; Mori et al. 2007). The contaminant is mainly composed of carbon and oxygen. Although the chemical composition of the contaminant is still uncertain, it is assumed in the calibration to be C/O=6 in number. The time evolution of the contaminant has been measured using regular observations of 1E 0102.2-7219. Note that, in this work, Fe $K\alpha$ lines (~ 7 keV) are main targets and the contamination effects almost nothing to the energy band.

Non-X-ray Background

One of the characteristic advantages of the XIS is a low and stable non-X-ray background (NXB), which is caused by cosmic-ray particles in the Suzaku orbit. Figure 2.23 shows the NXB spectra of the FI and BI sensors when the XIS observed the dark (night) Earth (no celestial X-ray is incident). The data during the passage through the south Atlantic anomaly (SAA) or from the calibration source area is excluded. The lines at 5.9 and 6.5 keV are due to scattered X-rays from the calibration sources (Mn $K\alpha$ and $K\beta$). Other than these, many lines from materials in the XIS and the XRT, $K\alpha$ lines of Al, Si, Ni, $K\beta$ of Ni, and $L\alpha$, $K\beta$, and $M\alpha$ lines of Au are detected.

The NXB rates in the 0.4–12 keV band is 0.1–0.2 counts s^{-1} in the FI sensors and

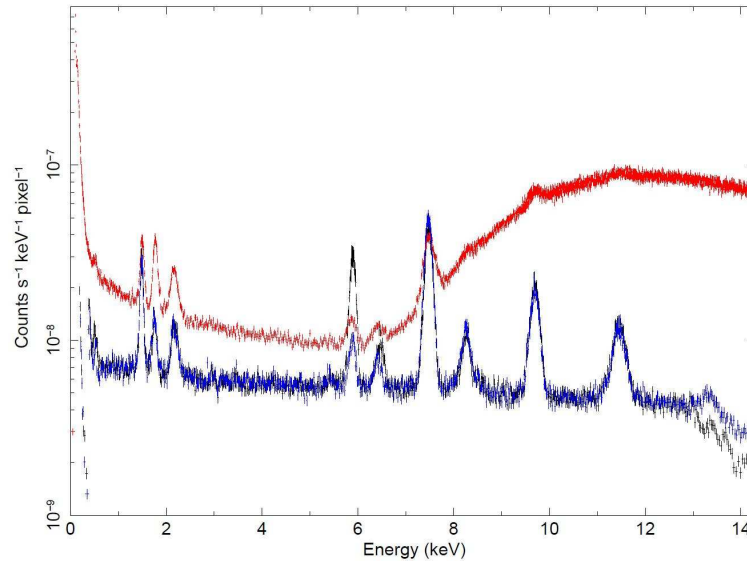


Figure 2.23: Spectra of the non-X-ray background for XIS 0 (black), XIS 1 (red), and XIS 3 (blue). The spectra are constructed from night Earth observations from the SCI start to 2010 May.

0.3–0.6 counts s^{-1} in the BI sensor. The NXB is not uniform over the chip. Since some fraction of the NXB is produced in the frame-store region and the NXB events made in pixels of the larger ACTY take the longer time to be read out (figure 2.13; Yamauchi et al. 2006), the flux tends to be slightly higher at larger ACTY as shown in the left panel of figure 2.24. The NXB also depends on the cut-off rigidity (COR) as shown in the right panel of figure 2.24. The NXB flux is higher at lower COR, where many cosmic-ray particles encounter the satellite. Thus, we need to select the NXB for an appropriate range of the COR in order to subtract the NXB from an observed data. Tawa et al. (2008) modeled the NXB spectra as a function of the COR and the position on the CCD. The model reconstructs the NXB spectra within the accuracy of 5%.

Thanks to the good energy resolution, large collecting area, and the low/stable NXB background, the XIS has a good spectral performance especially in the 5–10 keV band, including Fe-K lines. These capabilities also enable us to make line-resolved imaging for low surface brightness sources.

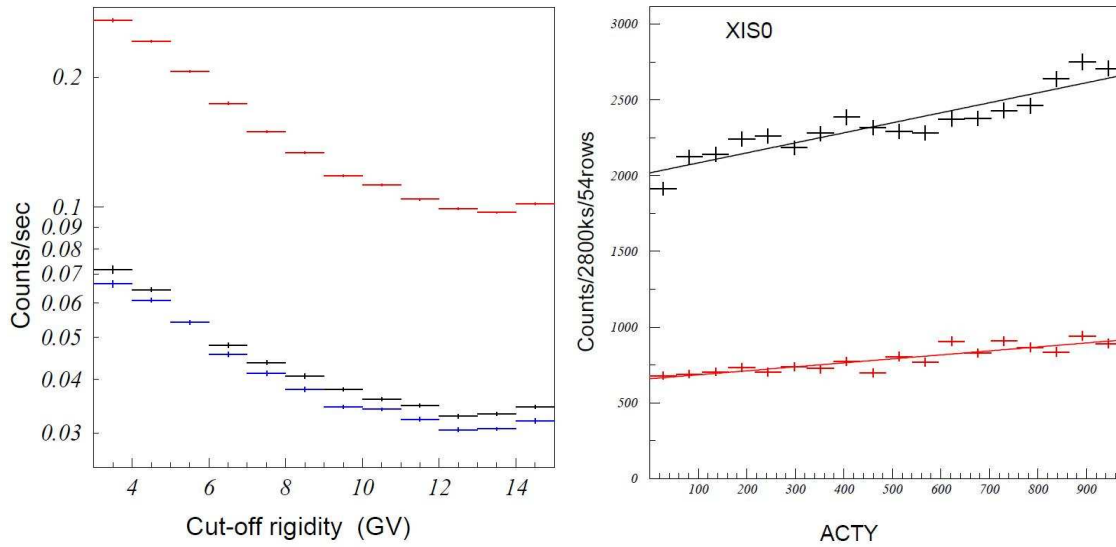


Figure 2.24: Left: NXB rate (average intensity for 5–10 keV) depends on the cut-off rigidity (COR) for each XIS sensor (black: XIS 0, red: XIS 1, blue: XIS 3). The NXB fluxes vary by a factor of ~ 2 depending on the COR (Tawa et al. 2008). Right: Dependence of the NXB on ACTY. Black and red lines indicate the continuum (2.5–5.5 keV) and Ni K α line (7.2–7.8 keV) components, respectively (Tawa et al. 2008).

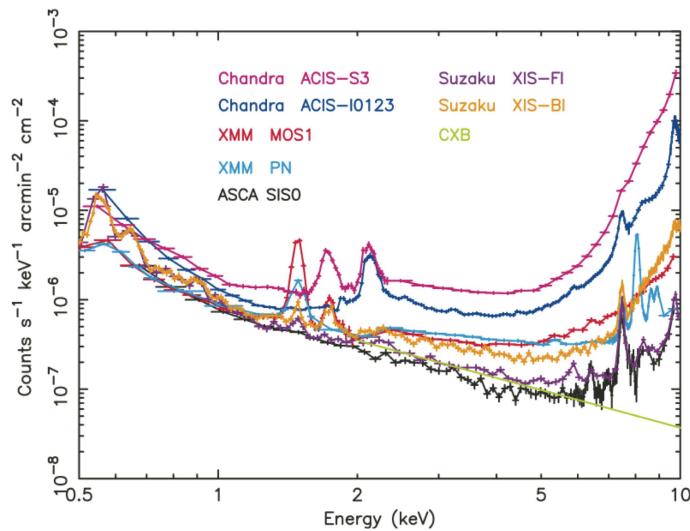


Figure 2.25: XIS background counting rate as a function of energy. They are normalized by the effective areas and the fields of view, which is a good measure of the sensitivity determined by the background for spatially extended sources. The background spectra of ASCA, Chandra, and XMM-Newton are shown for comparisons (Mitsuda et al. 2007).

Chapter 3

Discovery of K-shell Lines of Neutral Atoms from the Galactic Center Region

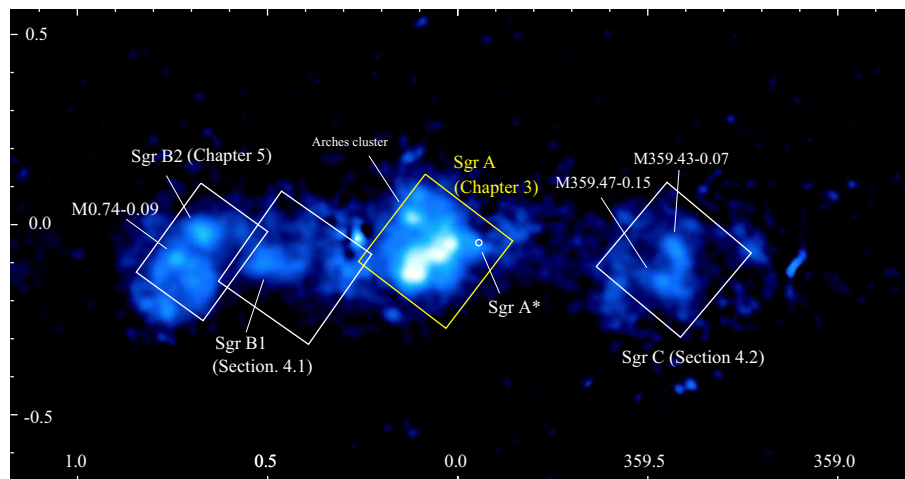


Figure 3.1: X-ray image in the 6.4 keV line taken by Suzaku/XIS. The transverse and vertical axes are the Galactic longitude and latitude in the unit of degree ($^{\circ}$). The solid boxes indicate the field of view of the observations used in this work. We see the brightest 6.4 keV cloud among the GC region in the Sgr A region indicated with the yellow square. The Arches cluster is in the northeast beside of the cloud (e.g. Tsujimoto et al. 2007). The super-massive black hole, Sgr A* inhabits at a position of the small circle. The other regions are referred in the next chapters.

3.1 Introduction

ASCA found clumpy structures in the 6.4 keV line from the Sgr B2 and the Radio Arc regions (Koyama et al. 1996). The clumps correspond to giant molecular clouds

found by radio observations (e.g. Tsuboi et al. 1999). The X-ray spectrum of the Sgr B2 cloud has a prominent 6.4 keV line on the continuum emission with deep absorption of $N_{\text{H}} \sim 10^{24} \text{ cm}^{-2}$ (e.g. Murakami et al. 2000). Recently, many new 6.4 keV clouds have been discovered in a variety of regions (Koyama et al. 2007b; Yusef-Zadeh et al. 2007; Nobukawa et al. 2008; Fukuoka et al. 2009; Nakajima et al. 2009).

Koyama et al. (1996) and Murakami et al. (2000) suggested that the 6.4 keV emission from the 6.4 keV clouds is due to the K-shell ionization of iron atoms by external X-rays, possibly from the super-massive black hole, Sgr A* (an X-ray reflection nebula; XRN). The present X-ray luminosity of Sgr A* is $L_{\text{X}} \sim 10^{33} \text{ erg s}^{-1}$, although some flares with $L_{\text{X}} = 10^{34}\text{--}10^{35} \text{ erg s}^{-1}$ have been found by Chandra and XMM-Newton (Baganoff et al. 2001, 2003; Porquet et al. 2003). However, the luminosity required for the 6.4 keV emission is $10^{38\text{--}39} \text{ erg s}^{-1} \text{ cm}^{-2}$. Therefore, Sgr A* in a few hundred years ago would have been $10^{3\text{--}6}$ times brighter than now (e. g. Koyama et al. 1996). On the other hand, Yusef-Zadeh et al. (2007) proposed that the origin of the 6.4 keV emission would be low energy cosmic-ray electrons ($E_{\text{e}} = 10\text{--}100 \text{ keV}$), because they found that the X-rays correlated with non-thermal radio filaments. The origin of the 6.4 keV line has been an open question so far.

Neutral atoms of lighter elements than Fe, such as Ar and Ca, should also exist in the 6.4 keV clouds, and hence would emit K-shell emission lines. These would provide new information to constrain the origin of the 6.4 keV clouds in the GC region since there is a difference between the X-ray and electron origins, for example, between the cross sections of K-shell photo-absorption by X-rays and K-shell ionization by electrons. However, only the K-shell lines of neutral Fe and Ni atoms have been discovered so far.

The Sgr A region is the best place for the search of neutral K-shell lines of various elements because many bright clouds have been found at $(l, b) \sim (0.1^\circ, -0.1^\circ)$ (see figure 3.1) and the absorption column density is relatively small among the 6.4 keV clouds in the GC region. Moreover, many observations with the total exposure time $\sim 200 \text{ ks}$ have been performed with Suzaku (Koyama et al. 2007c; Hyodo et al. 2009).

We analyzed the X-ray data obtained with the Suzaku/XIS and found emission lines from neutral Ar, Ca, Cr, and Mn atoms for the first time. This chapter reports on detailed analyses, results, and the severe constraint on the origin of the 6.4 keV emission.

3.2 Observations and Data Reduction

The eastern vicinity of Sgr A* was observed 4 times in 2005, 2006, and 2007 with Suzaku/XIS. Each pointing position and roll angle were almost the same. The observation list is listed in table 3.1.

The XIS observations were made in the normal clocking and the full-window mode. XIS 2 has been out of use since 2006 November, hence we did not use the XIS 2 data in 2007 September. The data in 2007 September were taken with the SCI technique. For the data reduction, we used the `xispi` software version 2008-04-10, and the calibration database version 2008-08-25. We removed the data during the epoch of low-Earth elevation angles of less than 5° ($\text{ELV} < 5^\circ$), day Earth elevation angles of less than 10° ($\text{DYE_ELV} < 10^\circ$),

Table 3.1: Observation Data List.

Observation ID	R.A.	Decl.	XIS	SCI	obs start	exposure time*
100027010	266.5146	-28.9267	0 1 2 3	off	2005-09-23	44.8 ks
100037040	266.5133	-28.9266	0 1 2 3	off	2005-09-30	43.0 ks
100048010	266.5135	-28.9269	0 1 2 3	off	2006-09-08	63.0 ks
102013010	266.5129	-28.9278	0 1 3	on	2007-09-03	51.4 ks

*After the data screening described in the text.

and the South Atlantic Anomaly. The good exposure times are listed in table 3.1. The overall spectral resolutions (FI/BI) at 5.9 keV were 150/150, 175/185, and 140/175 eV (FWHM) for the 2005, 2006, and 2007 observations, respectively.

We sorted the NXB with the COR values using `xisnxbgen` from the night-Earth data released by the Suzaku XIS team (see section 2.3.4). The COR-sorted NXB was subtracted from the raw data with the same COR.

Since we checked that the relative gain of the FI sensors were well calibrated and the response functions were essentially the same, we co-added the FI data. We also summed the spectra of the four observations to increase the statistics.

We analyzed the data using the software package HEASoft 6.6.1. For spectral fittings, we made XIS response files using `xisrmfgen`, and auxiliary files using `xissimarfgen`. Errors quoted in this chapter are estimated at the 90% confidence levels unless otherwise stated.

3.3 Analysis and Results

3.3.1 6.4 keV line Image

In order to depict 6.4 keV clouds from the GC region, we made an X-ray image in the 6.4 keV line by the following procedures. We first made X-ray images in the 5–6 keV and in the 6.3–6.5 keV bands, after subtracting the NXB and correcting the vignetting effect. We extracted the X-ray spectrum from a 8' circular region near the field center, and fitted the 5–6 keV band spectrum with a power-law model. The best-fit photon index in the 5.0–6.0 keV band is 1.25 ± 0.07 . The ratio of the photon flux in the 6.3–6.5 keV band to that in the 5.0–6.0 keV band was estimated to be 0.165, by extrapolation of the power-law index. We multiplied the 5.0–6.0 keV band image by 0.165, and subtracted from the 6.3–6.5 keV band image. The result is shown in figure 3.2.

We can see a bright region near the center of the 6.4 keV line image, as is shown with the solid line of a gourd-like shape (hereafter, the Source region). Around the Source region, we can see fainter emissions, which may be due to unresolved minor 6.4 keV clouds.

The X-ray emission from the GC hot plasma contributes to the spectrum of the Source region. In order to examine the contribution of the GC hot plasma accurately, we selected the dashed region, excluding the supernova remnant, Sgr A East (Maeda et al. 2002).,

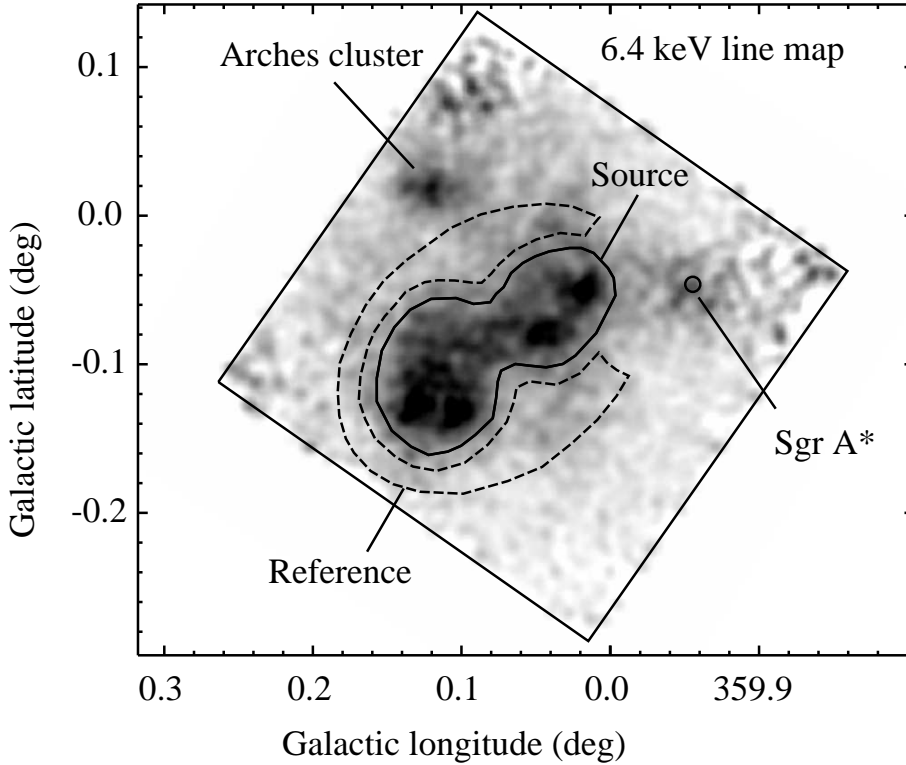


Figure 3.2: X-ray image in the 6.4 keV neutral iron line (the underlying continuum fluxes are subtracted). The solid square is the FOV of the XIS. The small circle indicates the position of Sgr A*. We extracted the source spectrum from the solid region (Source). In order to examine the contribution of the GC hot plasma, we also selected the surrounding region (Reference) marked with the dashed line. The areas of the Source and Reference regions are 43.3 and 40.5 arcmin², respectively. The bright source in the northeast edge of the FOV is the Arches cluster (e.g., Tsujimoto et al. 2007).

whose size and position are $\sim 3'$ and $(l, b) \sim (-359.5^\circ, -0.5^\circ)$. Hereafter, we call this region as Reference.

3.3.2 Gain Tuning

The nominal uncertainty of the absolute energy of XIS is ~ 10 eV (the Suzaku XIS team¹). To be more accurate, we checked the energy of the $K\alpha$ lines of H-like S (S XV) of the spectra and the calibration source ^{55}Fe (emits the Mn I $K\alpha$ line at 5895 eV) attached at the corner of the XIS. Compared with the theoretical value obtained from Atomic & Molecular Database in the Institute of Applied Physics and Computational Mathematics (CAMDB)², we found that the energy differences of S XV $K\alpha$ and Mn I $K\alpha$ were 5 ± 2 and 0 ± 1 eV for FI, while those for BI were consistent with the theoretical energies. We,

¹http://www.astro.isas.ac.jp/suzaku/doc/suzaku_td

²http://www.camdb.ac.cn/spectraspectra_search.asp

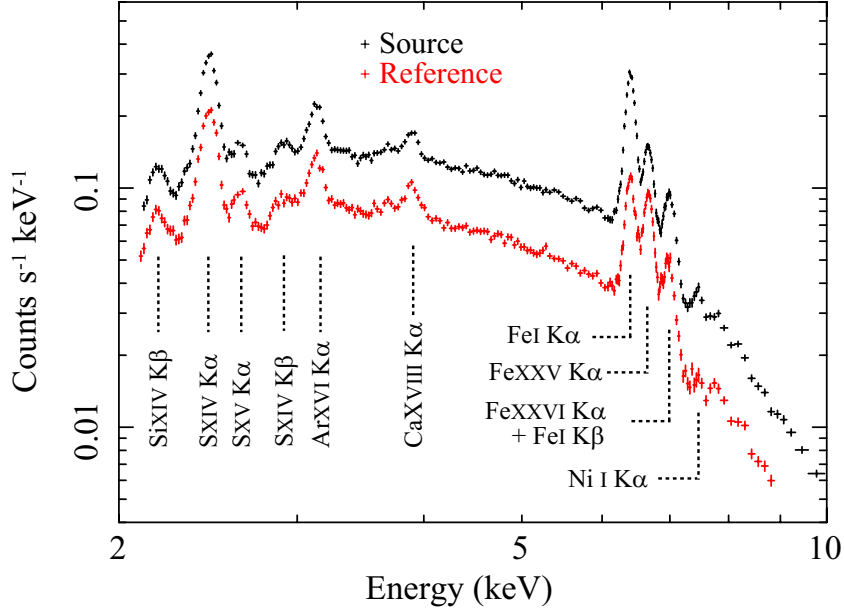


Figure 3.3: X-ray Spectra (FI) in the Source (black) and the Reference (red) regions, where the NXB was already subtracted. Identified emission lines are indicated by the dashed lines with their corresponding elements. Errors of the data are estimated at the 1σ confidence level.

therefore, fine-tuned the energy scale for FI as a liner function;

$$\Delta E = -0.0015 \times (E_0 - 5895) \text{ (eV)}, \quad (3.1)$$

where E_0 and ΔE are the original and energy shift, respectively.

3.3.3 Model Construction

Figure 3.3 shows the X-ray spectra of the FI sensor in the Source and Reference regions. The spectra have several ionized emission lines of heavy elements, such as Si, S, Ar, Ca, and Fe. These lines would come from the GC hot plasma with the temperature of $kT \sim 7$ keV (Koyama et al. 2007c) and possibly $kT \sim 1$ keV (Ryu et al. 2009).

On the other hand, we can see prominent $K\alpha$ lines of neutral Fe and Ni at 6.4 keV and 7.5 keV in the spectra. The neutral lines indicate the existence of a large amount of neutral Fe and Ni atoms in the regions. The neutral lines from the Reference region may be due to many faint unresolved 6.4 keV clouds.

The X-ray spectra of the two regions (Source and Reference) would be a complex of the GC hot plasma and the 6.4 keV clouds (Koyama et al. 2009; Ryu et al. 2009). We, therefore, made a fitting model composed of the GC hot plasma (here *Plasma*), the 6.4 keV clouds (here *Neutral*) and the Cosmic X-ray background (here *CXB*). Thus, the model is given by;

$$Model = Abs1 \times [Plasma + Neutral] + CXB, \quad (3.2)$$

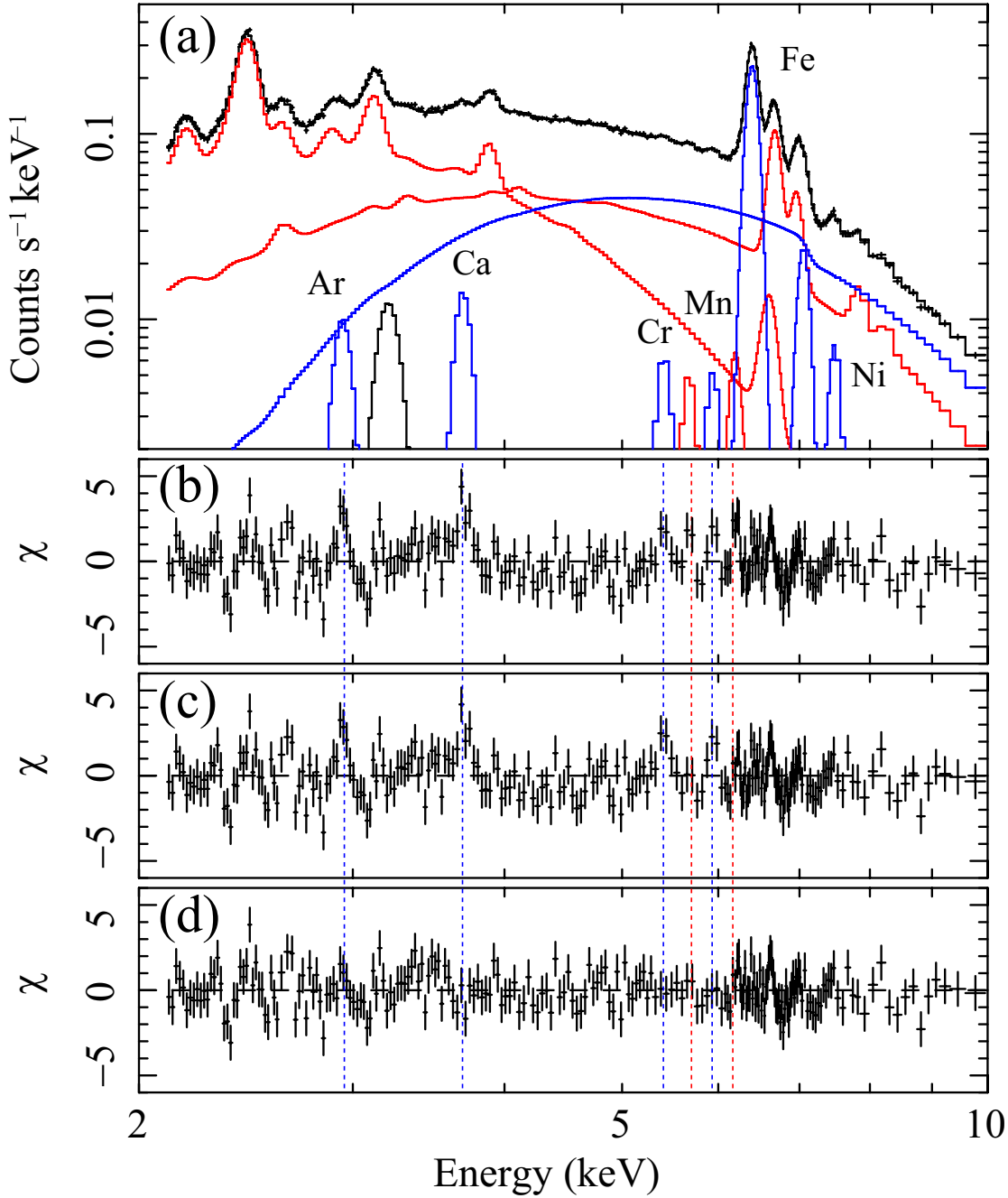


Figure 3.4: (a): FI Spectrum of the Source region fitted with the final model (step 3) in subsection 3.3.4 (see text). The red and blue histograms are the best-fit *Plasma* and *Neutral* components, respectively. The Gaussian line at 3.2 keV is added to compensate the uncertainty of the instrumental response. The blue and red dashed lines indicate the energies of the neutral K α of Ar, Ca, Cr, Mn and the He-like K α of Cr and Mn. (b): Residual of the fitting with the models of *2-kT APEC*, a power-law, and neutral lines of Fe I K α , K β , Ni I K α (step 1). (c): Same as (b), but the ionized Cr and Mn lines were added (step 2). (d): Same as (c), but the neutral Ar, Ca, Cr, and Mn K α lines were added (step 3). Errors of the data were estimated at the 1σ confidence level.

where $Abs1$ is absorption of the inter-stellar medium toward the GC region. The absorption is determined by the spectral shape at a lower energy band where photo-absorption is more effective than at a high energy band.

Ryu et al. (2009) found that the GC hot plasma (*Plasma*) has two-temperature components, and hence the *Plasma* model can be described as

$$Plasma = APEC1 + APEC2 \text{ (photons s}^{-1} \text{ cm}^{-2}\text{)}, \quad (3.3)$$

where *APEC1* and *APEC2* are thin thermal plasma code in the XSPEC package for the low (kT_1) and high (kT_2) temperature components, respectively.

Neutral is composed of neutral lines and associated continuum emission, and hence can be given by

$$Neutral = Abs2 \times [A \times (E/\text{keV})^{-\Gamma} + Gaussians] \\ \text{(photons s}^{-1} \text{ cm}^{-2}\text{)}, \quad (3.4)$$

where $Abs2$ is self-absorption in the 6.4 keV clouds. Neutral lines are expressed by Gaussians, while the continuum is represented by a power-law model with the photon index Γ and the normalization A .

The cosmic X-ray background (CXB) flux is lower than the whole spectra shown in figure 3.3 by more than two orders of magnitude. We nevertheless add the CXB model made by Kushino et al. (2002),

$$CXB = Abs1 \times Abs1 \times 7.4 \times 10^{-7} \times (E/\text{keV})^{-1.41} \\ \text{(photons keV}^{-1} \text{ s}^{-1} \text{ cm}^{-2} \text{ arcmin}^{-2}\text{)}, \quad (3.5)$$

where absorption column density ($Abs1$) is applied twice because the origin of the CXB is extragalactic.

3.3.4 Spectral Fitting

Since the surface brightness of *Plasma* is not constant, the spectrum of *Neutral* cannot be directly obtained by the subtracting the surrounding (Reference) region. We therefore tried to simultaneously fit these two regions and to determine the spectra of the *Neutral* and *Plasma* models, separately.

The X-ray photons below ~ 2 keV from the GC region are heavily absorbed by an inter-stellar medium of $N_H \sim 6 \times 10^{22} \text{ cm}^{-2}$, and the X-ray spectrum below ~ 2 keV is dominated by the local background (Ryu et al. 2009). We therefore used only the 2–10 keV band for the spectral analysis.

In the fitting of *Plasma*, we assumed that the temperatures (kT_1 and kT_2) and elemental abundances (Z) of Si, S, Fe, and Ni were common in the two regions (Source and Reference). Abundances of Ar and Ca were set to be the same as that of S. Also, $Abs1$ was treated to be common in the two regions. On the other hand, we set the normalizations of the hot plasma (*APEC1*, *APEC2*) to be independent free parameters.

For *Neutral*, common free parameters among the two regions are the power-law index (Γ), the equivalent widths (flux ratio) of the neutral lines to the continuum, and line center

energies. The normalization of the power-law (A) is an independent free parameter. With these constraints, we proceeded the model fitting with equation (3.2) along the following 3 steps:

Step 1: Gaussians for K-shell Lines from Fe and Ni

For the *Neutral* model of equation (3.4), we first tried a fitting with three Gaussians for Fe I $K\alpha$ (6.40 keV), Fe I $K\beta$ (7.06 keV), and Ni I $K\alpha$ (7.49 keV) lines (e.g. Koyama et al. 1996; Koyama et al. 2007c).

This fit left many residuals, including that at ~ 3.2 keV. The energy is near the M-edge of Au (3.2–3.4 keV), and hence the residuals are likely due to the calibration uncertainty of the response of the XRT. In fact, similar residuals were reported by Kubota et al. (2007). We, thus, added a broad Gaussian line at ~ 3.2 keV according to Kubota et al. (2007). The best-fit center energy and the line width (1 sigma) of the Gaussian are 3.24 ± 0.02 keV and 0.07 ± 0.02 keV, respectively.

The fitting residuals are displayed simply for the FI spectra of the Source region in figure 3.4b, although the fitting was made simultaneously for the both sensors (FI and BI) and both the two regions. As shown in figure 3.4b, this model was not able to reproduce the observed spectra ($\chi^2/\text{d.o.f}$ is 1447/906).

Step 2: K-shell Lines from Highly Ionized Cr and Mn

One reason of the unacceptable fit is that the APEC model does not contain Cr and Mn K-lines at 5–6 keV. We therefore added two Gaussian lines in the *Plasma* model of equation (3.3) at ~ 5.7 and 6.2 keV for the Cr XXIII and Mn XXIV $K\alpha$ lines, then, the center energies were obtained to be 5.68 ± 0.02 and 6.19 ± 0.02 keV, respectively. These are consistent with theoretical energies of 5.67 and 6.17 keV (CAMDB), the He-like Cr (Cr XXIII) and Mn (Mn XXIV).

The hot plasma can also emit $K\alpha$ lines of H-like Cr (Cr XXIV) and Mn (Mn XXV) at 5.94 keV and 6.44 keV, respectively. Using the two-APEC model with the temperatures of 1 keV and 7 keV and the flux ratios given in table 3.2, we plotted the intensity ratio of H-like to He-like $K\alpha$ lines as a function of atomic number (Ar, Ca, Fe) in figure 3.5. By interpolation, we estimated the line intensity ratios of Cr and Mn to be 0.22 and 0.28. We added these four lines in the *Plasma* model:

$$\begin{aligned} \textit{Plasma} = \textit{APEC1} + \textit{APEC2} + 4 \textit{Gaussians} (\text{Cr, Mn}) \\ (\text{photons s}^{-1} \text{ cm}^{-2}), \end{aligned} \quad (3.6)$$

where the intensity ratios of H-like to He-like Cr and Mn were fixed to be 0.22 and 0.28. We also set the equivalent widths of Cr XXIII $K\alpha$ and Mn XXIV $K\alpha$ to the continuum of the *Plasma* model to be the same in the two regions.

This fitting gave $\chi^2/\text{d.o.f}$ of 1367/902. The residuals from this model in the Source spectrum are shown in figure 3.4c. In the next step (step 3), we used the *Plasma* model of equation (3.6).

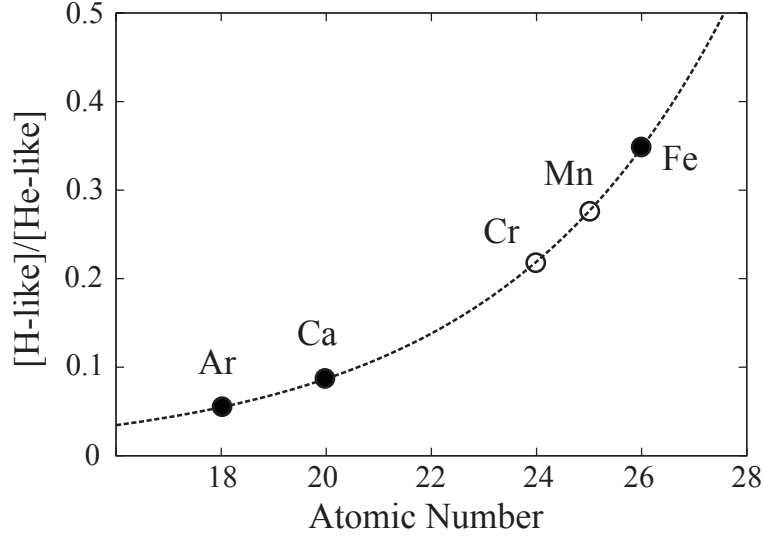


Figure 3.5: Line-intensity ratios of He- and H-like ions. The filled circles are calculated values using the APEC model. The values of Ar, Ca, and Fe are 0.057, 0.085, and 0.35, respectively. By interpolating these data, the line intensity ratios of Cr and Mn are estimated to be 0.22 and 0.28 (open circles).

Step 3: K-shell Lines from Neutral Ar, Ca, Cr, and Mn

Since we still found line-like residuals at the energies of ~ 3.0 , 3.7, 5.4, and 5.9 keV, we added four Gaussian lines to the *Neutral* model of equation (3.4) at these energies (in figure 3.4c, also see dashed lines in figure 3.4). Then the line energies were found to be 2.94 ± 0.02 , 3.69 ± 0.02 , 5.41 ± 0.04 , and 5.94 ± 0.03 keV, respectively. These values correspond to theoretical energies of 2.96, 3.69, 5.41, and 5.90 keV for the $K\alpha$ lines of Ar I, Ca I, Cr I, and Mn I. The fitting residuals in the spectrum of the Source region are shown in figure 3.4d.

As demonstrated in figure 3.4d, the $\chi^2/\text{d.o.f.}$ is largely improved from 1367/902 (step 2) to 1203/894 (step 3), but is not acceptable even at the 99% confidence level. Although the energy resolution in the hard X-ray band is well calibrated with the calibration source ^{55}Fe (emits the Mn I $K\alpha$ line), that in the soft band, especially about 2 keV, may have some uncertainty due to the absence of available calibration sources. Thus the deviation at ~ 2.5 keV would come from the incomplete response function in the soft energy band.

Residuals are also found at $\sim 6.5\text{--}7.0$ keV, with a slight mismatch of the center energy of Fe XXV $K\alpha$. This suggests that the GC hot plasma has more than two temperature components. We therefore tried a fitting with a three- kT plasma model. Although the fit was improved from $\chi^2/\text{d.o.f.}=1203/894$ to 1123/891, the best-fit parameters for the *Neutral* and *Plasma* models do not change from those in the two- kT model within the statistical errors. We, thus, regard that the two- kT model after step 3 is a good approximation to derive the physical parameters.

Table 3.2: Fitting results of *Plasma*.

Component	Parameter	Unit	Value*
<i>Abs1</i>	N_{H}	10^{22} cm^{-2}	6.75 ± 0.13
<i>APEC1</i>	kT_1	keV	$1.01^{+0.01}_{-0.02}$
	Norm	†	12 ± 1
<i>APEC2</i>	kT_2	keV	7.0 ± 0.1
	Norm	†	1.3 ± 0.1
Abundances	Si	solar	$2.52^{+0.09}_{-0.17}$
	S, Ar, Ca	solar	1.87 ± 0.07
	Fe	solar	$1.16^{+0.07}_{-0.04}$
	Ni	solar	1.64 ± 0.37
Gaussian Lines			
Cr XXIII $K\alpha$	energy	(keV)	5.68 ± 0.02
	EW	(eV)	22 ± 6
Mn XXIV $K\alpha$	energy	(keV)	6.19 ± 0.02
	EW	(eV)	39 ± 6

* The uncertainties indicate the 90% confidence levels.

† Emission measure $10^{-12}/(4\pi D^2) \int n_e n_{\text{H}} dV$, where D is the distance to the source (cm), n_e and n_{H} are the electron and hydrogen density (cm^{-3}), respectively.

For the discussion on the 6.4 keV cloud in the Source region, we list the best-fit parameters for the *Plasma* model in table 3.2, while those for the *Neutral* model are listed in table 3.3. For comparison, the best-fit parameters of the Reference region are: normalizations of *APEC1* and *APEC2* are 6.8 ± 0.5 and $0.90^{+0.06}_{-0.04}$ in the same unit shown in table 2, respectively. *Abs2* and normalization of the power-law component are $12.7^{+1.2}_{-1.8} \times 10^{22} \text{ H cm}^{-2}$ and $3.0^{+0.5}_{-0.4} \times 10^{-3} \text{ photons keV}^{-1} \text{ s}^{-1} \text{ cm}^{-2}$, respectively. The other parameters are the same as the Source region.

3.4 Discussion for the X-ray Emission from the Sgr A region

3.4.1 The GC hot plasma

The absorption column density toward the GC region (*Abs1*) is $\sim 6.7 \times 10^{22} \text{ H cm}^{-2}$, a typical value to the GC region (e.g., Munro et al. 2004). This is the first constraint that the low temperature $kT = 1.01^{+0.01}_{-0.02} \text{ keV}$ plasma is also in the GC region.

Koyama et al. (2007c), using the same data set of this paper, reported the temperature of the GC hot plasma is $kT = 6.5 \pm 0.1 \text{ keV}$. The 1 keV plasma also emits Fe XXV $K\alpha$, but no significant Fe XXVI $K\alpha$. Since Koyama et al. (2007c) ignored the Fe lines from the 1.0 keV plasma, they under-estimated the flux ratio of Fe XXVI $K\alpha$ to Fe XXV $K\alpha$, i.e., the plasma temperature. Indeed, about 20% of the Fe XXV $K\alpha$ line may come from the 1.0 keV plasma. The flux ratio of the Fe lines is estimated to be 0.35 and 0.42 about the

Table 3.3: Fitting Results of *Neutral* and those of calculated values.*

Neutral Lines					
Energy (keV)	Identification	Intensity [†]	EW(eV) [‡]	EW(XRN) [§]	EW(LECRE) [§]
2.94 ± 0.02	Ar I $K\alpha$	170_{-40}^{+60}	140 ± 40	45	12
3.69 ± 0.02	Ca I $K\alpha$	54_{-9}^{+14}	83 ± 13	35	10
5.41 ± 0.04	Cr I $K\alpha$	9.5 ± 2.5	24 ± 7	10	3.5
5.94 ± 0.03	Mn I $K\alpha$	7.4 ± 2.2	22 ± 7	7.6	2.8
6.404 ± 0.002	Fe I $K\alpha$	340 ± 10	1150 ± 90	730	270
7.06 (fixed)	Fe I $K\beta$	40 ± 3	160 ± 20	120	38
7.48 ± 0.02	Ni I $K\alpha$	18 ± 3	83 ± 13	53	18
Continuum					
Photon Index		Γ		1.87 ± 0.04	
Normalization				$9.6_{-1.3}^{+1.6}$	
$Abs2(N_H)$		10^{22} cm^{-2}		12.0 ± 1.1	

* The uncertainties indicate the 90% confidence levels.

† Absorption-corrected line intensity in the unit of $10^{-6} \text{ photon s}^{-1} \text{ cm}^{-2}$.

‡ Observed equivalent widths of the neutral lines to the power-law continuum in equation (3.4).

§ Calculated equivalent widths in the XRN and LECRE scenarios when the metal abundances are the solar values and the photon index of the incident X-rays is 1.87.

|| Normalization at 1 keV in the unit of $10^{-3} \text{ photons keV}^{-1} \text{ s}^{-1} \text{ cm}^{-2}$.

6.5 keV and 7.0 keV plasmas by the APEC model, respectively. Taking the contribution of the low temperature plasma into account, the result in Koyama et al. (2007c) is consistent with our work.

The Fe and Ni abundances of 1.1–1.2 and 1.3–2.0 solar are more precise than the previous work (Koyama et al. 2007c). The abundances of lighter elements, Si and S, (Ar, Ca), were respectively determined to be 2.3–2.6 and 1.8–2.0 solar, for the first time. The highly ionized Cr and Mn lines in the GC region were discovered for the first time, but details are beyond the scope of this thesis.

3.4.2 Origin of the Neutral Clump

We discovered the K-shell lines of neutral Ar, Ca, Cr, and Mn from the bright 6.4 keV cloud toward the Sgr A region at the significance levels of 6.8, 9.6, 6.1, and 5.4 σ , respectively. The absorption column densities, $N_H(Abs2)$ in the Source and Reference regions are $12.0(\pm 1.1) \times 10^{22}$ and $12.7_{-1.8}^{+1.2} \times 10^{22} \text{ cm}^{-1}$, respectively.

The photon index, Γ of the continuum (power-law) is 1.87 ± 0.04 , which is consistent with the result of Koyama et al. (2009) in the same region. The equivalent widths of the neutral $K\alpha$ lines to the power-law continuum are $\sim 140, 83, 24, 22, 1150, 83 \text{ eV}$ in Ar, Ca, Cr, Mn, Fe, and Ni, respectively.

The major possibility for the origin of the 6.4 keV clouds is the ionization of neutral atoms by either low energy cosmic-ray electrons (LECRE: Yusef-Zadeh et al. 2007) with an

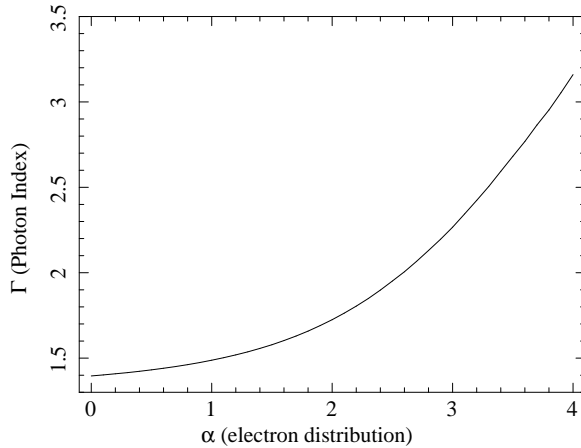


Figure 3.6: Photon index Γ of the X-ray spectrum emitted from a molecular cloud when electrons with the spectral index α are injected (solid line).

energy of 10–100 keV, or X-rays of external sources (XRN: Koyama et al. 1996; Murakami et al. 2000). The ionization cross-sections for these processes are very different. They also produce a continuum emission: the bremsstrahlung in the LECRe scenario and Thomson scattering in the XRN scenario. As a result, the two scenarios make different X-ray spectra. In particular, sharp contrasts are the photon index of the continuum and the equivalent widths of the neutral lines.

The continuum emission in the X-ray spectrum produced by the LECRe scenario is an integration of the bremsstrahlung by electrons with various energies. According to Tatischeff (2003), we calculated the X-ray spectrum with various indexes of their energy distributions into a molecular cloud. Figure 3.6 shows a relationship between the electron spectral index α and the X-ray photon index Γ . As a result, the photon index of $\Gamma = 1.9$ corresponds to an index of the LECRe source spectrum of $\alpha \sim 3$. On the other hand, the Thomson scattering do not change the photon index from the incident spectrum of the external source.

Tatischeff (2003) and Yusef-Zadeh et al. calculated the observed X-ray spectrum produced in the LECRe model. On the other hand, Murakami et al. (2000) estimated the XRN spectrum by a numerical simulation. We improved the calculations to the other relevant elements. Figure 3.8 shows the equivalent widths of the K-shell lines for Ar, Ca, Cr, Mn, Fe, and Ni calculated in the XRN (black) and LECRe models on the assumption that the elemental abundances in the cloud is the solar values. We found that abundant elements such as Fe have a large equivalent width. Although the equivalent width depends on the incident spectral index, we found a large difference between the absolute values in the two scenarios. Thus, the equivalent width of the line is a good indicator for constraint of the origin.

The equivalent widths produced by the LECRe with the index $\alpha = 3$ were estimated as shown with the red solid line in figure 3.7 as well as in figure 3.8. These are listed in table 3.3 and plotted in figure 3.7 together with the best-fit results.

From figure 3.7, the equivalent width of each element in the solar abundance is larger

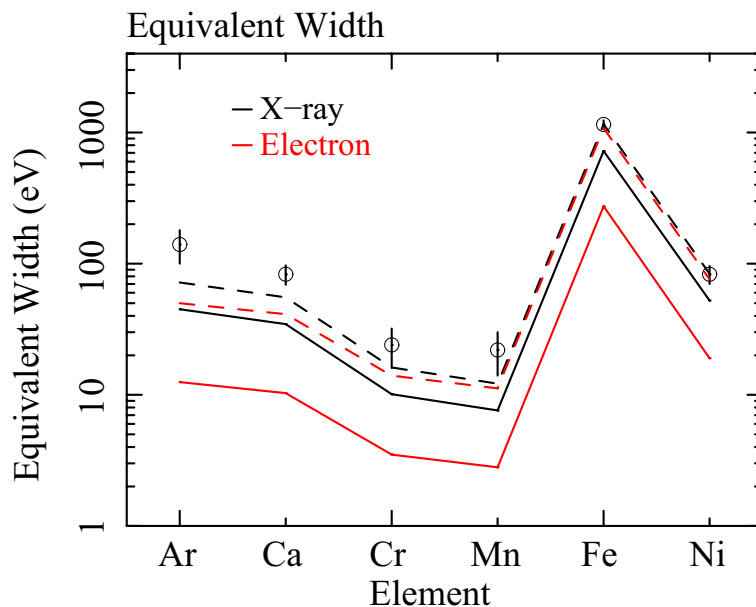


Figure 3.7: Equivalent widths of $K\alpha$ line of various neutral atoms. Black and red lines are the calculated values for the X-ray (XRN) and electron (LECRE) scenarios, respectively. The data points marked with the open circles are the observed value in our work. Errors were estimated at the 90% confidence level. The black and red dashed lines are to guide eyes, which are XRN and LECRe scenarios in 1.6 solar and 4.0 solar abundances, respectively.

than that expected in the both of the LECRe and XRN scenarios. For the LECRe scenario, the abundances of the molecular cloud must be ~ 4 -times larger than the solar value, while the XRN scenario requires ~ 1.6 solar abundance.

Since the molecular cloud may be formed by condensation of the ambient materials, the abundances should be similar to those of 1–2 solar in the GC hot plasma. Accordingly, the neutral lines from the GC region likely come from the fluorescence by external X-rays.

3.5 Summary

The summary of the results in this chapter is as follows:

- We found that a $kT = 1.0$ keV plasma exists in the GC region as well as the $kT = 7.0$ keV plasma. The elemental abundances of Si, S (Ar, Ca), Fe, Ni were measured to be 2.3–2.6, 1.8–1.9, 1.1–1.2, 1.3–2.0 times larger than the solar value. We also discovered He-like Cr and Mn $K\alpha$ lines from the GC region.
- K-shell lines of neutral Ar, Ca, Cr, and Mn were firstly discovered in addition to those of Fe and Ni. Equivalent widths of these atoms are ~ 140 , 83, 24, 22, 1150, and 83 eV, respectively.

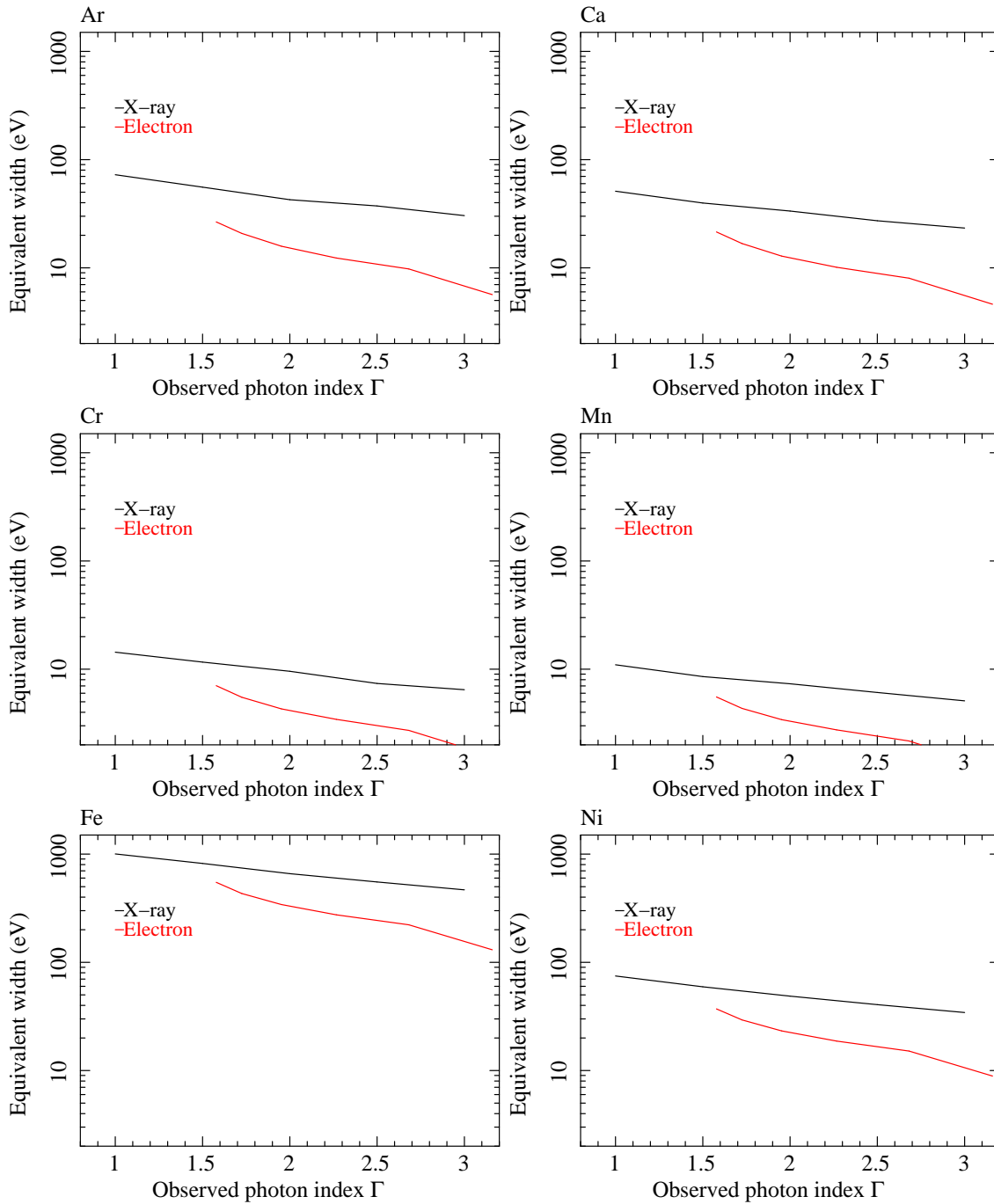


Figure 3.8: Equivalent width of various elements respective to a photon index of an observed X-ray spectrum in the XRN (black) and LECRe (red) models.

- The observed equivalent widths of Ar, Ca, Cr, Mn, Fe and Ni favor the X-ray radiation origin to the molecular cloud with 1–2 solar abundance.

Chapter 4

Other 6.4 keV Clouds in the Sgr B1 and C Regions

In figure 4.1, we see many molecular clouds emitting Fe I $K\alpha$ X-rays other than in the Sgr A region, which was analyzed in chapter 3). As is shown by solid squares in figure 4.1, the Sgr B1 and Sgr C regions are at the east and west side relative to the GC, i.e., Sgr A*, respectively. In this chapter, I investigate detailed X-ray features of 6.4 keV clouds found in the Sgr B1 and Sgr C regions (Murakami et al. 2001; Yusef-Zadeh et al. 2007). Analyses and discussions for Sgr B1 and C are made separately in section 4.1 and 4.2, respectively.

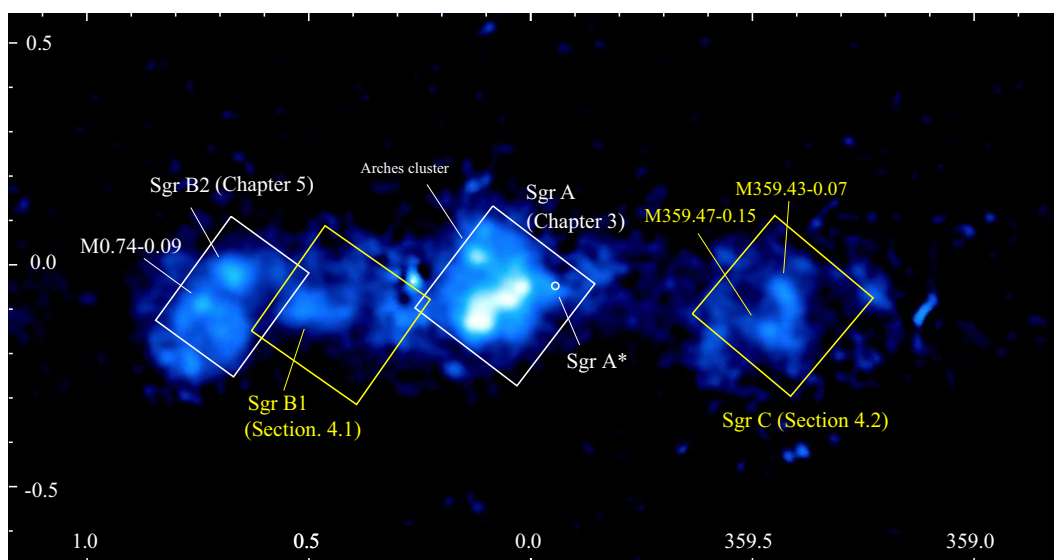


Figure 4.1: X-ray image in the 6.4 keV line same as figure 3.1. In this chapter, 6.4 keV clouds, Sgr B1, M 359.43–0.07, and M 359.47–0.15, in the yellow boxed regions are focused in this chapter.

4.1 Sgr B1

4.1.1 Introduction for Sgr B1

The radio complex Sgr B1 located to the west, or to the negative Galactic longitude of the Sgr B2 giant molecular cloud consists of a H II region surrounded by a molecular loop (Sofue 1990). The expansion of the molecular loop is explained by the past activity of the H II region (Sofue 1990). A 6.4 keV cloud was discovered in this region by Yusef-Zadeh et al. (2007). OH and H₂O masers have been found and a lot of intermediate and/or low-mass stars are formed (Mehringer et al. 1993).

Yusef-Zadeh et al. (2007) suggested that the 6.4 keV X-rays are due to collision of low-energy cosmic ray electrons with molecular gas because of a correlation between non-thermal radio filaments and the X-ray features taken by Chandra. The scenario explains not only the Fe I K α emission, but also cosmic-ray heating of molecular gas and diffuse TeV emission from the Galactic molecular clouds. However, Yusef-Zadeh et al. (2007) did not exhibit detailed features in the X-ray spectrum.

Thanks to the characteristic features of the large effective area and low/stable background, the XIS are instruments suitable to observe diffuse and faint objects. We had observed the Sgr B1 region for about 100 ks with Suzaku in order to obtain a good spectrum of the 6.4 keV cloud detected by Yusef-Zadeh et al. (2007). We report on the detailed analysis and result of the Sgr B1 cloud in this section.

4.1.2 Observation and Data Reduction

We observed the Sgr B1 region with Suzaku/XIS on 2006 March 27–29. The pointing angle was (R.A., Decl.)=(266.7693°, -28.6295°). The XIS data were taken in the normal mode. The XIS pulse-height data for each X-ray event were converted to Pulse Invariant (PI) channels using the xispi software and the calibration database released by the Suzaku/XIS team. After removing the epoch of low earth elevation angle less than 5 degree (ELV < 5°), the day earth elevation angle less than 10 degree (DYE_ELV < 10°) and the South Atlantic Anomaly (SAA), the effective exposure time was about 95 ks. We made the data reduction and analysis using HEADAS software 6.1.2 and XSPEC 11.3.2 for Sgr B1.

Since relative gain among FI sensors are well calibrated and the response functions are essentially the same, we co-added their data. We also applied the non-X-ray background (NXB) data from the night Earth data released by the Suzaku XIS team¹. The NXB data were sorted with the geomagnetic cut-off rigidity (COR) because of the variation of the NXB corresponding to the COR values.

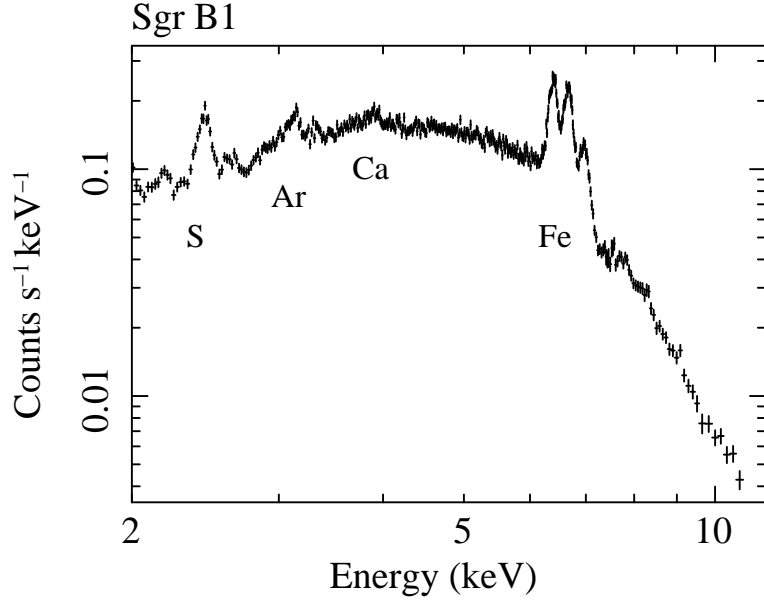


Figure 4.2: X-ray spectrum of the Sgr B1 region (FI: XIS0+2+3). The spectrum was collected from the full FOV, but excluding the corners where the calibration sources (^{55}Fe) illuminate Mn I K lines. The non-X-ray backgrounds were already subtracted.

4.1.3 Analysis and Results

The Overall Features

We show the X-ray spectrum of the Sgr B1 region in figure 4.2. It is the FI (the average of XIS0, 2 and 3) spectrum extracted from the full FOV excluding the corners where the calibration sources of ^{55}Fe illuminate. The NXB was already subtracted from the spectra. The spectrum shows K emission lines from He-like and/or H-like ions of S, Ar, Ca and Fe. In addition, $K\alpha$ emission line at 6.4 keV and K-edge absorption at 7.1 keV of neutral or low ionized Fe are cleanly detected. Three Fe lines at 6.4, 6.7 and 6.9 keV are well resolved thanks to the excellent energy resolution of the XIS.

We examined the characteristic lines of Fe I, Fe XXV, and Fe XXVI. We show narrow band images of 6.4 keV (6.30 to 6.50 keV; Fe I) and 6.7 keV (6.57 to 6.77 keV; Fe XXV) in figure 4.3a, b and c, respectively. They are co-added images of the four XIS, in which the NXB was subtracted and the correction of exposure and vignetting effects were already done. The exposure maps were made with `xissim` (Ishisaki et al. 2007) in HEADAS software 6.1.2.

We see clearly a diffuse source in the elliptic solid region shown in figures 4.3a. We hereafter call the source M0.51–0.10. M0.51–0.10 is identified with the 6.4 keV cloud Sgr B1 discovered by Yusef-Zadeh et al. (2007) whose position of $l, b \sim (0.5^\circ, -0.1^\circ)$ is the same.

We here note the excesses near the western edge of the FOV in each image. A known bright X-ray source with the flux of a few 10^{-10} ergs $\text{s}^{-1} \text{cm}^{-2}$, 1E 1743.1–2843, is located

¹<http://www.astro.isas.jaxa.jp/suzaku/analysis/xis/nte/>

outside the FOV in the northwest direction (Del Santo et al. 2006) and its position is marked with a small green circle in figure 4.3. The northwest excess is due to the XRT PSF (point spread function) tail of 1E 1743.1–2843. It has a hard X-ray spectrum, which is consistent with the result that the northwest excess is seen in all the panels in figure 4.3.

Spatial Distribution of the Fe XXV $K\alpha$ emission

Figure 4.3b and figure 4.4 show the narrow band image of 6.7 keV (Fe XXV), namely distribution of the GCDX. Figures 4, 5 and 6 of Koyama et al. (2007c) gave the profile of the fluxes of the 6.7 keV line and the flux ratios of 6.7 and 6.9 (Fe XXVI) keV lines as a function of the galactic longitude between $l = -0.4^\circ$ – $+0.2^\circ$. We made the same profiles for the Sgr B1 region of $l = +0.3^\circ$ – $+0.6^\circ$ and compared them with the results of Koyama et al. (2007c).

First, we divided the Sgr B1 region into 4×4 small regions excluding the four corners illuminated by the built-in calibration sources as shown in figure 4.3c. Next, we obtained the co-added spectrum of the 3 FIs (XIS0, 2 and 3) for each small region. We finally obtained 6.7 keV and 6.9 keV line fluxes and their ratio for each small region by fitting the spectrum with a continuum (thermal bremsstrahlung), Fe lines, which are Fe I $K\alpha$ and $K\beta$ (6.4 and 7.06 keV), Fe XXV $K\alpha$ (6.7 keV), and Fe XXVI $Ly\alpha$ (6.9 keV), and the cosmic X-ray background (CXB). Koyama et al. (2006) suggested the 6.7 keV emission smoothly extends to the Sgr B2 region ($l = +0.6^\circ$ – $+0.8^\circ$) with almost the same temperature. Thus, we made follow-up analyses on the Fe emission lines for the Sgr B2 region in the same method as done for Sgr B1.

In figure 4.5 we show the 6.7 keV line flux (top) and the ratio between the photon fluxes of 6.7 keV and 6.9 keV lines (bottom) as a function of the Galactic longitude. Excluding the data of the region at G 0.61+0.01 (will be mentioned later on), we found that the 6.7 keV line flux exponentially decreases from the peak at the GC ($l \sim -0.05^\circ$) and smoothly connects the Sgr B1 and B2 regions. The line flux ratios of $[\text{Fe XXVI}]/[\text{Fe XXV}]$ in the Sgr B1 and B2 regions are almost the same as the ones in $l = -0.4^\circ$ – $+0.2^\circ$.

We note that the three data points marked with filled circles in the Sgr B2 region having high 6.7 keV fluxes and low flux ratios between the 6.7 keV and 6.9 keV lines correspond to SNR G 0.61+0.01, which Koyama et al. (2007b) recently discovered with Suzaku. The plasma temperature of G 0.61+0.01 is $kT \sim 3$ keV (Koyama et al. 2007b), which is significantly lower than that of the GCDX ($kT \sim 6$ – 7 keV; Koyama et al. 2007c). We see that the 6.7 keV intensity of the small region [3-2] is rather higher than expectation from the whole tendency and the ratio of $[\text{Fe XXVI}]/[\text{Fe XXV}]$ is lower than the average of the GCDX. G 0.61+0.01 is located to the east of the small region [3-2] (see figure 4.4). This result suggests that the SNR would have a larger size than the one reported by Koyama et al. (2007b) and the small region [3-2] is a part of the G 0.61+0.01.

Spectrum of a 6.4 keV Clump, M 0.51–0.10

We examine M 0.51–0.10, a diffuse source in the 6.4 keV narrow band image of figure 4.3a. We identified this diffuse source with the 6.4 keV cloud, Sgr B1 detected by Yusef-

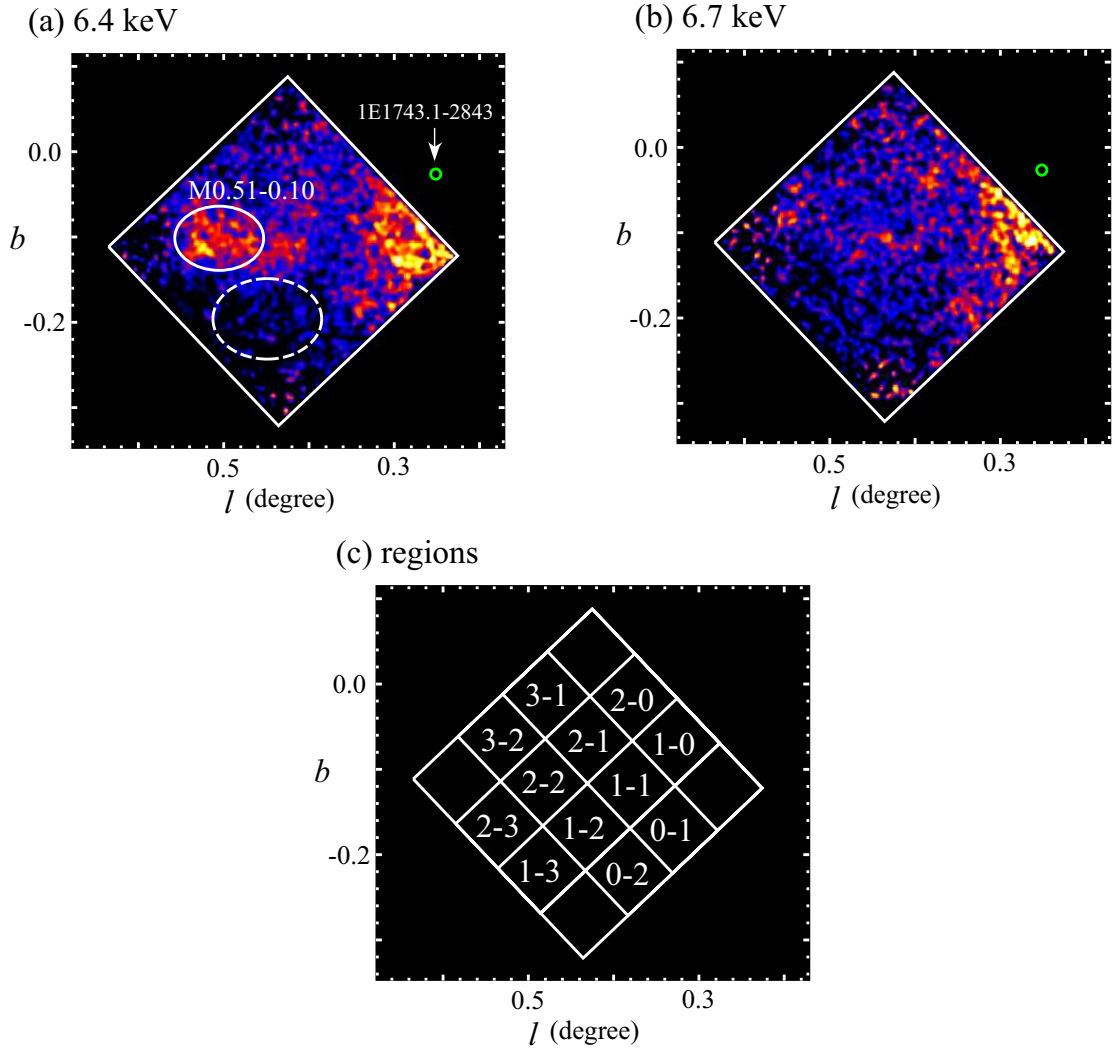


Figure 4.3: The narrow band images in 6.30–6.50 keV (a) and 6.57–6.77 keV (b). They are the co-added images of the four XIS. The subtraction of the NXB was already done and the effects of the exposure and vignetting are taken into account. The solid and dashed lines in the panel (a) show the regions for the spectra of M0.51–0.10 and its background, respectively. The minor and major axes of each elliptical region are $2.3' \times 3.1'$ (source), $2.8' \times 3.8'$ (background), respectively. (c) shows the small square regions and their ID numbers used in section 4.1.3.

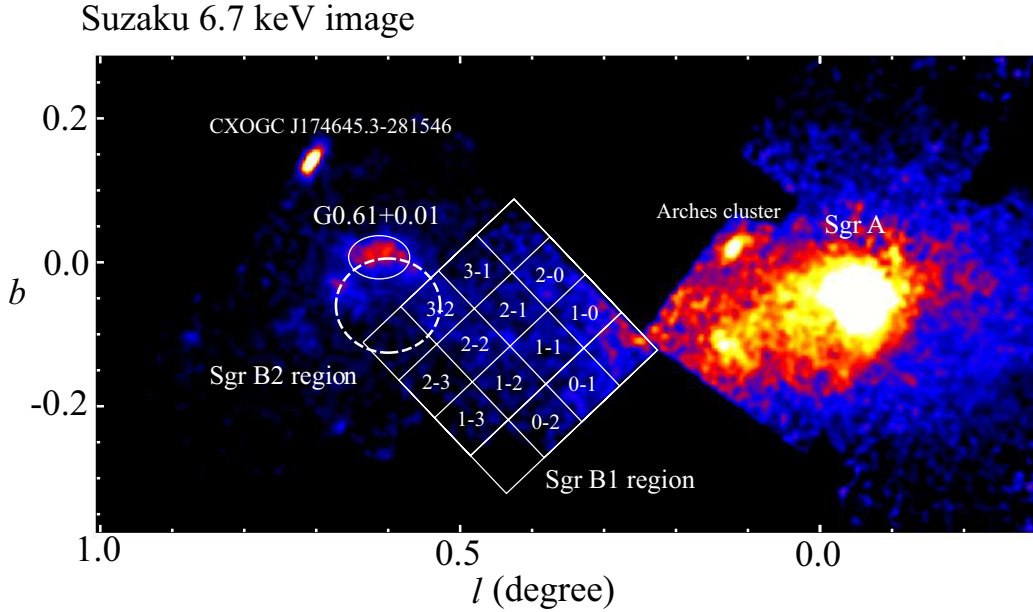


Figure 4.4: The 6.7 keV band image of the Sgr A to Sgr B2 regions with Suzaku. Excepting Sgr B1, the image is adopted from Koyama et al. (2007b), Koyama et al. (2007c), Hyodo et al. (2008), and Mori et al. (2008). The small square regions and the numbers are the same as figure 4.3d. G 0.61+0.01 is located to the east of the Sgr B1 region (the solid ellipse; Koyama et al. 2007b). We can think that G 0.61+0.01 is a part of the dashed shell. There are the other bright sources, CXOGC J174645.3–281546 (Muno et al. 2006; Hyodo et al. 2008) and Arches cluster (Tsujiimoto et al. 2007).

Zadeh et al. (2007). But we will call the 6.4 keV cloud M 0.51–0.10 in order to avoid the confusion with the H II region “Sgr B1” at $(l, b) = (0.5^\circ, -0.05^\circ)$ near the 6.4 keV cloud.

We obtained the background-subtracted spectra shown in figure 4.6, in which the source and background spectra are extracted from the solid and dashed regions in figure 4.3a, respectively. We selected the background region referring to the top panel of figure 4.5, so that the 6.7 keV line fluxes, namely the GCDX, of the two regions are almost the same level within the statistical errors. We assume that since the NXB and CXB are the same in the source and background regions, their contribution is successfully subtracted.

We checked a residual contribution of point sources after the background subtraction with the point source catalog by Muno et al. (2006). There are 14 and 11 point sources in the source and background regions, respectively. Those fluxes per a square arcminute in the 2 to 10 keV band are $5.0 \times 10^{-15} \text{ erg cm}^{-2} \text{ s}^{-1} \text{ arcmin}^{-2}$ in the source region, and $6.4 \times 10^{-15} \text{ erg cm}^{-2} \text{ s}^{-1} \text{ arcmin}^{-2}$ in the background region. Though the flux in the background region is somehow larger than that in the source region, the difference ($1.4 \times 10^{-15} \text{ erg cm}^{-2} \text{ s}^{-1} \text{ arcmin}^{-2}$) is only 3% of the flux of M 0.51–0.10 ($5.4 \times 10^{-14} \text{ erg cm}^{-2} \text{ s}^{-1} \text{ arcmin}^{-2}$). Thus, the contribution from the point sources after the background subtraction can be ignored.

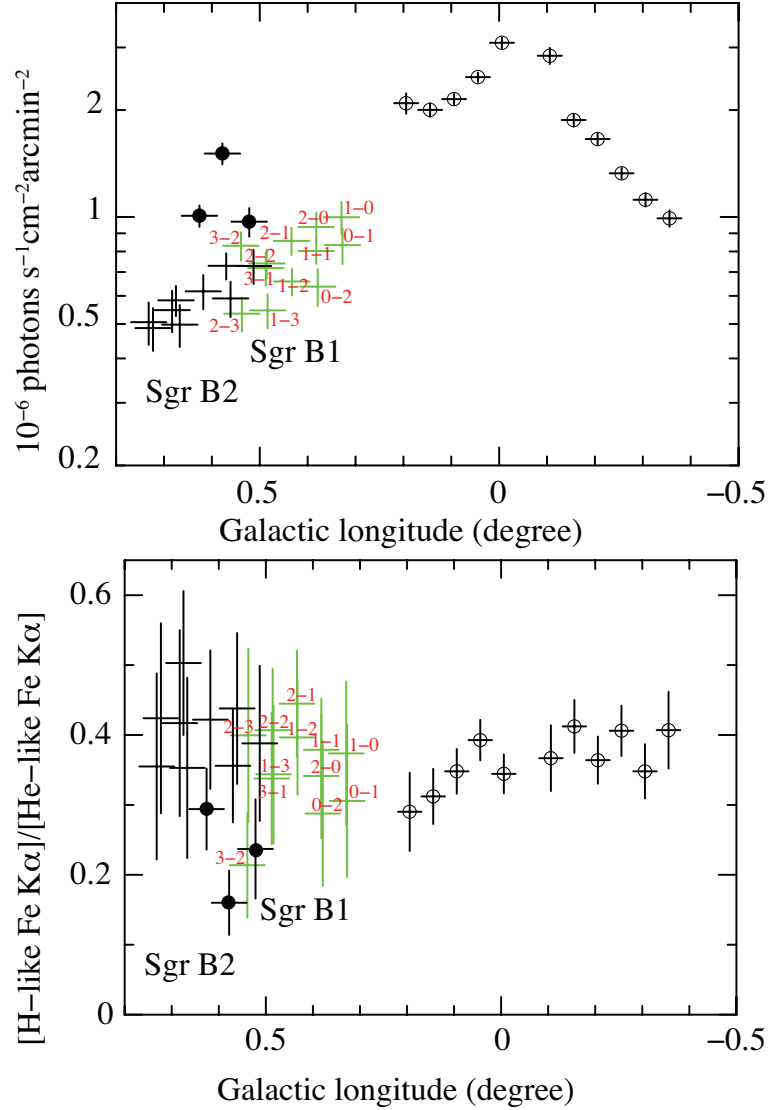


Figure 4.5: Top panel: The 6.7 keV line fluxes of the GC region at $l = -0.4^\circ \sim +0.8^\circ$ including the Sgr B1 and B2 regions. The data of the Sgr B1 region obtained in this observation are colored with green. Data marked with open circles are adopted from Koyama et al. (2007c). The data with filled circles correspond to SNR G0.61+0.01 (Koyama et al. 2007b). The ID number of the data correspond to the regions with the same ID number in figure 4.3c. Bottom panel: The same as in the top panel but for the photon flux ratios between the 6.7 and 6.9 keV lines.

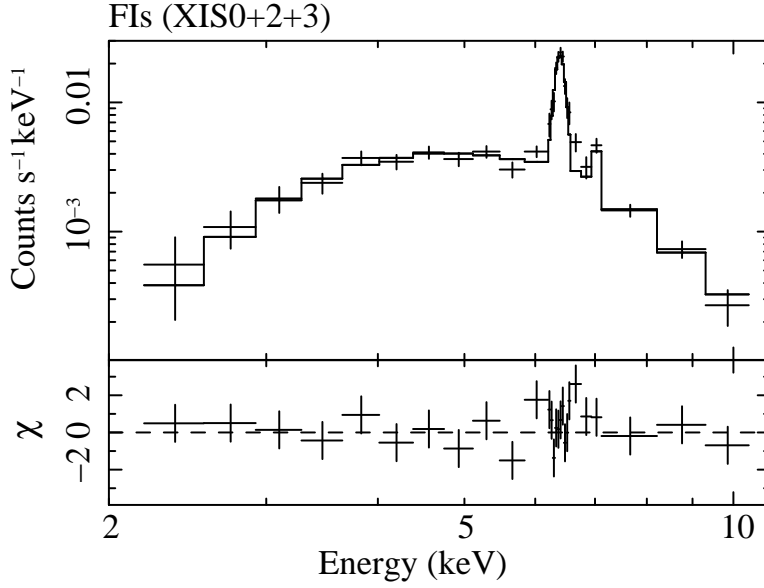


Figure 4.6: Background-subtracted FI spectrum extracted from M 0.51–0.10. The source and background spectra are extracted from the solid and dashed region in figure 4.3a, respectively.

The XIS spectra of M 0.51–0.10 contain the prominent 6.4 keV emission line. We fitted the spectra with the model consisting of an absorbed power-law component plus two gaussian lines of Fe I $K\alpha$ (6.4 keV) and $K\beta$ (7.06 keV). We obtained an acceptable result and show the best-fit parameters in table 4.1. Yusef-Zadeh et al. (2007) reported the equivalent width of the Fe I $K\alpha$ line is ~ 0.6 keV, smaller than our results of ~ 1.4 keV. Yusef-Zadeh et al. (2007) subtracted only the NXB from the source spectrum. We examined that the equivalent width of the Fe I $K\alpha$ line is obtained to be ~ 0.5 keV from our spectra when we subtracted only the NXB from the source spectra. We believe that the difference between the result of Yusef-Zadeh et al. (2007) and ours is due to the different assumption for the background emission.

4.1.4 Discussion for M 0.51–0.10

The absorption column of $1.5 \times 10^{23} \text{ cm}^{-2}$ is 2 times or more larger than the typical value of $6 \times 10^{22} \text{ cm}^{-2}$ for sources in the GC region. The strong 6.4 keV emission line implies that a large amount of iron in the neutral state exists at M 0.51–0.10. Thus, these results suggest M 0.51–0.10 is a local cool dense cloud in the GC region. Indeed, a molecular cloud lies at the same position of M 0.51–0.10, which is a part of the Sgr B1 molecular shell proposed by Sofue (1990) (see figure 4.7).

Two possible scenarios for the the origin of the 6.4 keV emission line have been proposed. One is photo-ionization by X-rays, namely the XRN (X-ray reflection nebula) scenario. The other is inner shell ionization by collision of low energy cosmic ray electrons. The observed large equivalent width of 1.4 keV and absorption column reaching $\sim 10^{23} \text{ cm}^{-2}$ are consistent with those of the XRN scenario. On the other hand, the

Table 4.1: Result of spectral fitting of M 0.51–0.10. The model is an absorbed power-law plus two gaussian lines.

Model component	value
Absorption (N_{H}) (10^{23} cm^{-2})	$1.5^{+0.2}_{-0.1}$
Continuum (power-law):	
Photon index (Γ)	$1.8^{+0.4}_{-0.5}$
Gaussian1 (Fe I $K\alpha$):	
Line center energy (eV)	6402^{+6}_{-7}
Intensity ($10^{-5} \text{ photons cm}^{-2} \text{ s}^{-1}$)	$2.8^{+0.2}_{-0.4}$
Equivalent Width (keV)	$1.4^{+0.3}_{-0.3}$
Gaussian2 (Fe I $K\beta$):	
Line center energy (eV) [†]	7061
Intensity ($10^{-5} \text{ photons cm}^{-2} \text{ s}^{-1}$)	$0.44^{+0.17}_{-0.21}$
Equivalent Width (keV)	$0.23^{+0.22}_{-0.21}$
Observed Flux ($10^{-12} \text{ ergs cm}^{-2} \text{ s}^{-1}$) [‡]	$1.2^{+0.1}_{-0.1}$
Luminosity ($10^{34} \text{ ergs s}^{-1}$) [§]	$1.9^{+0.1}_{-0.1}$
$\chi^2/\text{d.o.f.}$	50/37

note: The uncertainties indicate the 90% confidence limits.

[†] Fixed to $1.103 \times E(\text{Fe I } K\alpha)$.

[‡] In the 2 to 10 keV band.

[§] Absorption corrected in the 2 to 10 keV band.

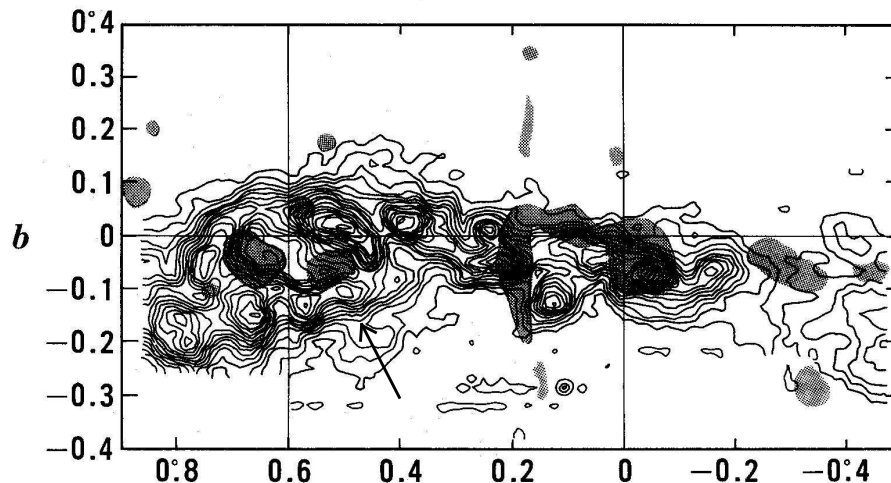


Figure 4.7: Distribution of the molecular gas in the GC region showed with the contours (^{13}CO). A structure around at $(l, b) \sim (0.5^\circ, 0.0^\circ)$ is the molecular shell in the Sgr B1 region (Sofue et al. 1990). The arrow indicates the small molecular cloud at $(l, b) = (0.5^\circ, -0.1^\circ)$, which may be a counterpart of the 6.4 keV cloud, M 0.51–0.10. The gray scale indicates radio continuum structures (H II region).

Table 4.2: Comparison between required luminosities and observed luminosities

the irradiating source candidates	distance* $D(\text{pc})$	photon index Γ	$L_{\text{obs}}\dagger$ (ergs s $^{-1}$)	$L_{\text{req}}\S$ (ergs s $^{-1}$)
1E 1743.1–2843	40	1.9 \dagger	3×10^{36}	2×10^{38}
Sgr A*	100	2.0 \ddagger	2×10^{33}	2×10^{39}

note: Those source are assumed to be at the same distance as M 0.51–0.10, 8.5 kpc. The bright source 1E 1743.1–2843 is a neutron star or black hole LMXB. Sgr A* is a super-massive black hole at the center of our galaxy.

* the distance to M 0.51–0.10.

\dagger the observed photon index and luminosity (Porquet et al. 2003; Baganoff et al. 2003).

\ddagger The assumed value by Koyama et al. (1996) and Murakami et al. (2000).

\S the required luminosity to account for the observed 6.4 keV flux of M 0.51–0.10. It is obtained from equation (4.1).

scenario of electron collision expects rather small equivalent width of ~ 300 eV and an absorption column less than $\sim 10^{21-22}$ cm $^{-2}$ assuming the elemental composition is the same as the solar system (see table 3.3 in section 3.4.2, Tatischeff 2003). The electron collision scenario requires the iron over-abundance by a factor of 4 – 5, while the photo-ionization model does not require the iron over-abundance. Thus, we conclude that M 0.51–0.10 is likely to be an X-ray reflection nebula.

In order to examine the irradiating source, we estimate its luminosity to require the M 0.51–0.10 fluorescence. The cloud absorbs X-rays with the energies higher than 7.1 keV from the external source and emits the fluorescent line of 6.4 keV X-rays. The photon flux of the 6.4 keV line, $C_{6.4\text{keV}}$ (photons s $^{-1}$ cm $^{-2}$), is described as the following equation,

$$C_{6.4\text{keV}} = \epsilon \frac{\Omega}{4\pi} \int_{7.1\text{keV}}^{\infty} \left(1 - e^{-N_{\text{Fe}}\sigma_{\text{Fe}}(E)}\right) AE^{-\Gamma} dE. \quad (4.1)$$

Here, we assume that the irradiating source has a power-law spectrum ($AE^{-\Gamma}$) and the iron abundance of the molecular cloud of M 0.51–0.10 is solar ($[\text{Fe}]/[\text{H}] = 3 \times 10^{-5}$). Since the typical absorption column for sources in the GC region is $N_{\text{H}} = 0.6 \times 10^{23}$ cm $^{-2}$, the one of M 0.51–0.10 itself is estimated to be $N_{\text{H}} = 0.9 \times 10^{23}$ cm $^{-2}$, i.e. $N_{\text{Fe}} = 2.7 \times 10^{18}$ cm $^{-2}$ from the results of the spectral fitting. $\Omega = \pi(r/D)^2$ is the solid angle covered by M 0.51–0.10 from the view point of the irradiating source, where r is the radius of M 0.51–0.10 and D is the distance between M 0.51–0.10 and the irradiating source. ϵ is the fluorescent yield of 0.34 for an iron atom. The K-shell photo-ionization cross section per an iron atom against an X-ray with the energy above 7.1 keV is $\sigma_{\text{Fe}} = 6.0 \times 10^{-18}(E/1\text{keV})^{-2.58}$ (cm 2) (Henke et al. 1982). $C_{6.4\text{keV}}$ is the observed Fe I $K\alpha$ line flux of 2.8×10^{-5} photons cm $^{-2}$ s $^{-1}$.

We discuss candidates for the irradiating source by estimating its luminosity with the equation (4.1). One is a bright X-ray source 1E 1743.1–2843, the PSF tail of which is seen at the northwestern edge of the XIS FOV in figure 4.3. 1E 1743.1–2843 is reported to be a neutron star or a black hole low mass X-ray binary in the GC region, or toward the GC region but beyond there (Porquet et al. 2003; Del Santo et al. 2006).

In the case that 1E 1743.1–2843 is located in the GC region, the projected distance

to the M0.51–0.10 cloud is $D = 40$ pc. Since the power-law slope for the X-ray spectrum of 1E 1743.1–2843 is reported to be $\Gamma = 1.9$ by Porquet et al. (2003), we obtain the luminosity of 2×10^{38} ergs s^{-1} required for the 6.4 keV line flux of M0.51–0.10. However, 1E 1743.1–2843 persistently has the luminosity of $(1 - 4) \times 10^{36}$ ergs s^{-1} (e.g. Cremonesi et al 1999; Porquet et al. 2003), which is 2 orders lower than the required luminosity. In addition, no bursts have been observed from 1E 1743.1–2843 in extensive observations over the last 20 years. In the case that 1E 1743.1–2843 would be beyond the GC region, it is too far to account for the 6.4 keV line flux of M0.51–0.10. Thus, 1E 1743.1–2843 is unlikely for the irradiating source of M0.51–0.10.

Total luminosity of all the cataloged bright point sources within 50 pc (20') from M0.51–0.10 is $\sim 3 \times 10^{35}$ ergs s^{-1} , which is far lower than the required luminosity of 10^{38-39} ergs s^{-1} .

Koyama et al. (1996) and Murakami et al. (2000) proposed that the GC super-massive black hole, Sgr A* irradiated molecular clouds in the Sgr B2 region. Sgr A* is then thought to have been 10^6 or more times brighter about 300 years ago, the light traveling time between Sgr B2 and Sgr A*.

We apply the XRN scenario by past activity of Sgr A* to M0.51–0.10. The Sgr B molecular complex, consisting of Sgr B1 ($l = 0.5^\circ$) and B2 ($l = 0.8^\circ$), belongs to the “Galactic-Center molecular Arm” surrounding Sgr A* (Sofue 1995). Sgr B1 and Sgr B2 are located at the same three dimensional distance from Sgr A* (~ 100 pc) though the projected distances are different. The photon index for Sgr A* is reported to be $\Gamma = 2.7$ by Baganoff et al. (2003), which is not consistent with that of M0.51–0.10 ($\Gamma = 1.3 - 2.2$). However, Baganoff et al. (2001) reported that the photon index became hard ($\Gamma \sim 1.0$) when Sgr A* is in flare-up state.

Koyama et al. (1996) and Murakami et al. (2000) assumed that the photon index is 2.0 for the power-law spectrum of Sgr A*, and reported that the required luminosity for Sgr B2 cloud is $\sim 3 \times 10^{39}$ ergs s^{-1} . We also estimated the required luminosity for M0.51–0.10 to be $\sim 2 \times 10^{39}$ ergs s^{-1} . Since we do not take the limited duration time of the X-ray irradiation from the past Sgr A* flare into account in this calculation, it is consistent with the case in Sgr B2.

4.1.5 Summary

In this section, we analyzed the data of the Sgr B1 region observed with Suzaku with the long exposure ~ 100 ks.

- The line flux ratio $[\text{Fe XXVI}]/[\text{Fe XXV}]$ of the Sgr B1 and B2 regions ($l = +0.3^\circ - +0.8^\circ$) is consistent with that of the region at $l = -0.4^\circ - +0.2^\circ$. The Fe XXV line flux exponentially decreases from the GC center to the Sgr B1 and B2 regions. This results suggest that the GCDX extends at least up to the Sgr B1 and B2 regions with a constant temperature of $kT = 6-7$ keV.
- M0.51–0.10 is identified with the 6.4 keV cloud “Sgr B1” detected by Yusef-Zadeh et al. (2007). The X-ray spectra of M0.51–0.10 exhibit a absorption column of $N_{\text{H}} \sim 1.5 \times 10^{23}$ cm^{-2} and a large equivalent width of ~ 1.4 keV for Fe I $K\alpha$

fluorescence emission line. It suggests that the 6.4 keV X-ray emission is unlikely due to collision of low energy cosmic ray electrons but due to reflection of external hard X-rays, and hence M 0.51–0.10 is thought to be an X-ray reflection nebula. The bright X-ray point source 1E 1743.1–2843 or the collection of fainter point sources near M 0.51–0.10 does not explain the luminosity of $\geq 10^{38-39}$ ergs s^{-1} required for the 6.4 keV X-rays from M 0.51–0.10. The XRN scenario by past activity of Sgr A*, which was successfully applied to Sgr B2, may also be applied to M 0.51–0.10.

4.2 Sgr C

4.2.1 Introduction for Sgr C

The Sgr C region located at $l \sim -359.5^\circ$ consists of giant molecular clouds, large H II regions, and radio non-thermal filaments (NTF). From the ^{13}CO observations, Liszt and Spiker (1995) estimated 6.1×10^5 solar mass for the molecular gas.

Murakami et al. (2001b) discovered a 6.4 keV cloud with ASCA, and interpreted that the cloud is an X-ray reflection nebula (XRN) because the X-ray spectrum exhibited a large equivalent width (EW) of the 6.4 keV emission line with a strong absorption like that in Sgr B2. On the other hand, Yusef-Zadeh et al. (2007) discussed possible association of the 6.4 keV emission lines with some radio NTFs based on the Chandra observation, and argued that the 6.4 keV line is due to the impact of low energy cosmic-ray electrons (LECRE).

These results and arguments are based on the short exposure observations (20 ks and 22 ks by the ASCA and Chandra, respectively). In order to fix the above debates, we, therefore, made a long Suzaku observation on the Sgr C region.

4.2.2 Observation and Data Reduction

The Sgr C region was observed with the Suzaku/XIS from 2006 February 20 to 23. The telescope optical axis position was R.A. = $17^{\text{h}}44^{\text{m}}37.30^{\text{s}}$, Decl. = $-29^\circ 28' 10.2''$ (J2000.0).

A cleaned event list was obtained from the processed data with the version of 2.0.6.13² by removing events taken during the passage of the South Atlantic Anomaly, the elevation angles from the night Earth rim of $< 5^\circ$ and from the sun-lit Earth rim of $< 20^\circ$, and the telemetry saturation. After these data screenings, the net exposure was 107 ks. We analyzed the screened data using the HEADAS software version 6.4, XSPEC version 11.3.2g³. We utilized the calibration databases released on 2008 February 1⁴.

We also made COR-sorted NXB data sets using the night-Earth data released by the Suzaku XIS team⁵. For the following imaging and spectral studies in the Sgr C region (section 4.2.3 and 4.2.3), we used the X-ray data after subtracting the NXB that were compiled to have the same COR distribution as that during the Sgr C observation.

To increase statistics, hereafter, we co-added the four XIS data for imaging study, in which exposure and vignetting correction were made. For the spectral study, we co-added the three FI CCD data, and treated BI data separately.

4.2.3 Analysis and Results

X-ray Image in the Emission Line

Figure 4.8 shows the energy spectrum of the whole Sgr C region, which was extracted from the circular region with a radius of $6.95'$ from the FOV center. The spectrum shows

²<http://www.astro.isas.jaxa.jp/suzaku/process/>

³<http://heasarc.gsfc.nasa.gov/docs/software/lheasoft/>

⁴<http://www.astro.isas.jaxa.jp/suzaku/caldb/>

⁵<http://www.astro.isas.jaxa.jp/suzaku/analysis/xis/nte/>

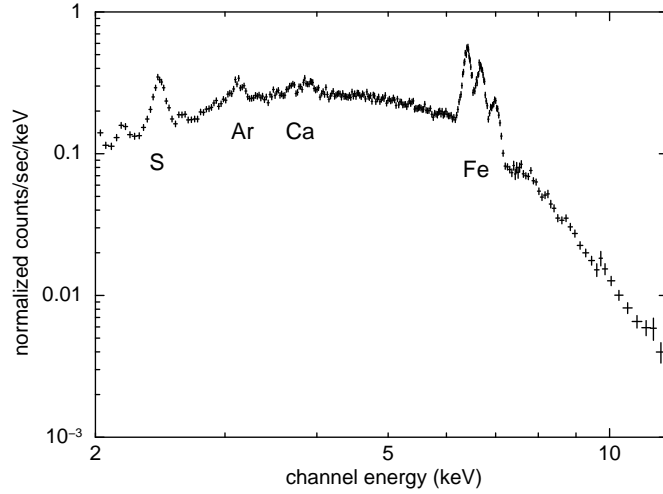


Figure 4.8: The co-added GCDX spectrum of the FIs (XIS0+2+3) in the Sgr C region extracted from the $6.95'$ radius circle in the center of the XIS FOV. The NXB component was subtracted. The spectrum of BI (XIS1) was simultaneously analyzed, but the figure is not shown here, for brevity.

K-shell emission lines from He-like and/or H-like ions of S, Ar, Ca, and Fe. In addition, the 6.4 keV emission line and the K-edge absorption at 7.1 keV due to Fe I are detected. The three Fe K-shell emission lines at 6.4, 6.7 and 6.9 keV in the Galactic center diffuse X-ray emission (GCDX: Koyama et al. 1989; Yamauchi et al. 1990; Koyama et al. 2007c) are clearly resolved.

Since the Suzaku coordinate has 90% confident error of $\sim 20''$ (Uchiyama et al. 2008), we made a coordinate correction using a Chandra observation. In the energy band of 0.7–1.5 keV, a point source with the flux of $\sim 6 \times 10^{-15}$ erg cm $^{-2}$ s $^{-1}$ was detected at (R.A., Decl.) $_{J2000.0} = (17^{\text{h}}44^{\text{m}}52.1^{\text{s}}, -29^{\circ}31'56.7'')$ in the XIS image. In the error circle of Suzaku, there was only one Chandra point source at (R.A., Decl.) $_{J2000.0} = (17^{\text{h}}44^{\text{m}}53.1^{\text{s}}, -29^{\circ}31'45.5'')$. Since the flux was almost the same as that of the Suzaku source, we safely concluded these point sources are identical. We, then fine-tuned the Suzaku coordinate by shifting $\Delta(\text{R.A.}, \text{Decl.}) = (13.7'', 11.2'')$.

Referring figure 4.8, we made the narrow band image of the 2.45 keV-line (2.35–2.50 keV; $K\alpha$ of S XV) and the 6.4 keV-line (6.28–6.42 keV; $K\alpha$ of Fe I). The images after the smoothing with the Gaussian kernel of 48 pixels ($0.83'$) are shown in figure 4.9. In figure 4.9a, a bright 2.45 keV-line clump is found at $(l, b) = (359.407^{\circ}, -0.119^{\circ})$, hence designated as G 359.41–0.12. Likely, four 6.4 keV-line clumps found in figure 4.9b are designated as M 359.43–0.07, M 359.47–0.15, M 359.43–0.12, and M 359.38–0.00, where M 359.43–0.12 is in the region of G 359.41–0.12.

The Emission Line Feature in the Sgr C Region

The photon statistics are limited to make measurable spectra for M 359.38–0.00 and M 359.43–0.12. Furthermore, M 359.43–0.12 is in the 2.45 keV-source, G 359.41–0.12. Therefore we concentrated on the two bright sources, M 359.43–0.07 and M 359.47–0.15,

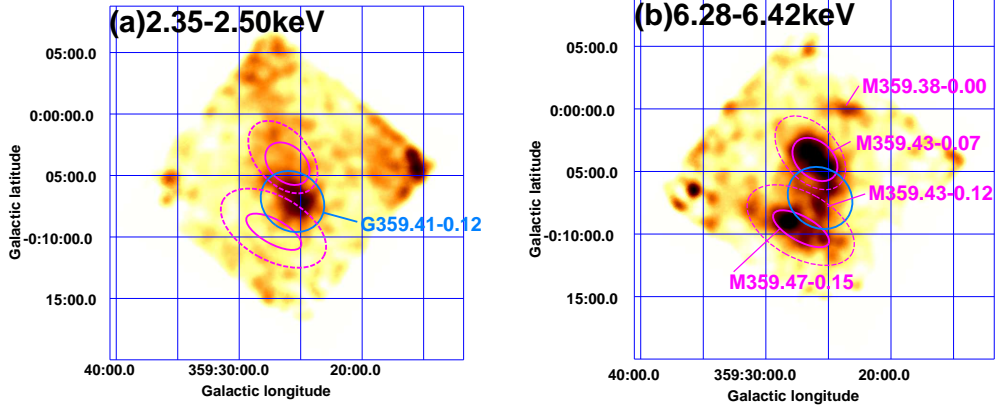


Figure 4.9: (a) The 2.45 keV-line (S XV $K\alpha$) image in the energy band of 2.35–2.50 keV and (b) the 6.4 keV-line (Fe I $K\alpha$) image in the 6.28–6.42 keV band. The source and background regions for the spectral analysis are shown with the solid and dashed magenta ellipses, where the data within the blue ellipse (G 359.41–0.12) were excluded to minimize the contamination from the strong 2.45 keV emission line and its associated continuum.

and the surrounding background regions.

As is seen in figure 4.8, the GCDX with strong 6.7 keV (Fe XXV $K\alpha$) and 6.9 keV (Fe XXVI $Ly\alpha$) lines is the largest background for the local enhancements such as the 6.4 keV-clumps. In addition, the flux of the GCDX is not uniform but variable from position to position. To see the flux distribution and nature of the GCDX near Sgr C, we examined the NXB-subtracted (GCDX is not subtracted) spectra in the 6.4-keV clumps and the surrounding areas including candidate background regions (see figure 4.9).

The spectra from the whole Sgr C region is already made in section 4.2.3 (figure 4.8). The spectra of M 359.43–0.07 and M 359.47–0.15 are extracted from the regions shown with the solid magenta ellipses in figure 4.9b. The background spectra for these 6.4 keV clumps were obtained from the annuli between the inner solid and outer dashed ellipses. Since G 359.41–0.12, the solid blue ellipse in figure 4.9a, may have strong 2.45 keV-line with an associated continuum emission, we excluded G 359.41–0.12 from the spectra of the 6.4-keV sources and their backgrounds. As the surrounding area, we made additional spectrum from a circle at the FOV center with a radius of $7.8'$ but excluding the above cited source and background regions (hereafter, the outer region).

The spectral fittings were made in the same energy band with the same phenomenological model and free parameters as those used in Koyama et al. (2007c; 2009): a single power-law and 10 Gaussian emission lines (table 4.3). The spectra of FIs and BI were simultaneously fitted, and acceptable χ^2 were obtained from all the spectra. The FI spectra and the best-fit model of M 359.43–0.07 and M 359.47–0.15, and the outer region of Sgr C are shown in figure 4.10 as examples. The best-fit parameters are listed in table 4.4.

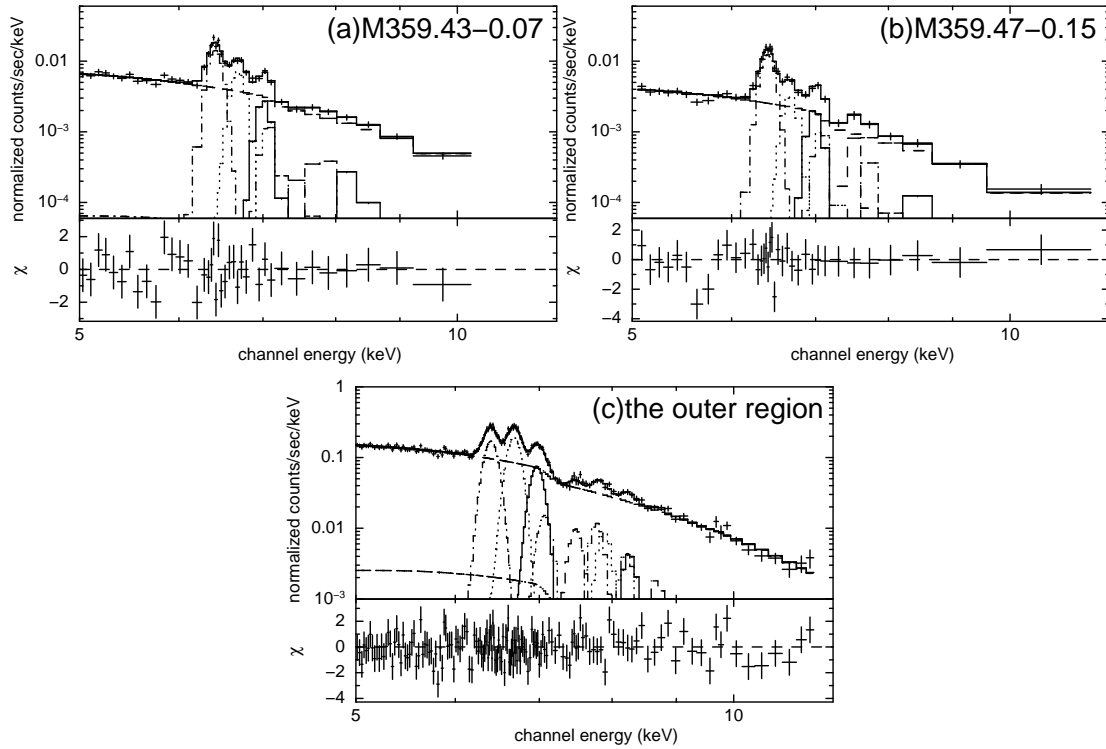


Figure 4.10: Same as figure 4.8, but for M 359.43–0.07 (a), M 359.47–0.15 (b), and the outer region (c). The phenomenological model with single power-law, 10 Gaussian lines, and the cosmic X-ray background component is applied.

Table 4.3: Center energies of the Fe and Ni lines from the GCDX obtained by Suzaku (Koyama et al. 2007c).

line	observed energy (eV)
Fe I $K\alpha$	6409^{+1}_{-1}
Fe XXV $K\alpha$	6680^{+1}_{-1}
Fe XXVI $K\alpha$	6969^{+6}_{-3}
Fe I $K\beta$	$7069 = 1.103 \times E(\text{Fe I } K\alpha)$
Ni I $K\beta$	7490^{+12}_{-14}
Ni XXVII $K\alpha$	7781^{+24}_{-31}
Fe XXV $K\beta$	$7891 = 110 + E(\text{Ni XXVII } K\alpha)$
Fe XXVI $K\beta$	8220^{+31}_{-22}
Fe XXV $K\gamma$	$8264 = 44 + E(\text{Fe XXVI } K\beta)$
Fe XXVI $K\gamma$	8681^{+33}_{-32}

Table 4.4: Best-fit parameters for the NXB-subtracted spectra*.

Region	Area (arcmin ²)	Γ	Line Flux†		Line Equivalent width (eV)	
			$F_{6.4}$	$F_{6.7}$	$EW_{6.4}$	$EW_{6.7}$
(1)	152	1.72(1.65 – 1.78)	0.79(0.77 – 0.81)	0.68(0.65 – 0.70)	458(448 – 470)	420(401 – 430)
(2)	121	1.70(1.63 – 1.82)	0.55(0.53 – 0.57)	0.68(0.66 – 0.71)	346(333 – 363)	454(441 – 471)
(3)	7.09	1.82(1.65 – 2.06)	1.91(1.79 – 2.06)	1.08(0.96 – 1.22)	670(625 – 720)	400(357 – 454)
(4)	11.7	1.64(1.47 – 1.93)	1.00(0.92 – 1.08)	0.93(0.86 – 1.03)	397(365 – 428)	388(360 – 431)
(5)	6.91	1.96(1.59 – 2.24)	2.16(2.03 – 2.31)	0.63(0.53 – 0.73)	966(909 – 1030)	298(253 – 348)
(6)	22.4	1.75(1.59 – 1.97)	1.02(0.97 – 1.08)	0.67(0.62 – 0.72)	587(554 – 620)	404(374 – 437)

(1) the whole Sgr C region, (2) the outer region, (3) M 359.43–0.07, (4) background region for M 359.43–0.07, (5) M 359.47–0.15,

(6) background region for M 359.47–0.15.

* 90% confidence limits are in parentheses.

† Absorption-uncorrected line flux in the unit of 10^{-6} ph cm⁻² s⁻¹ arcmin⁻².

Koyama et al. (2009) found that the GCDX in the Sgr A region is phenomenologically decomposed into the 6.7-keV line plus associated continuum (6.7-component) and the 6.4-keV line plus associated continuum (6.4-component); the EWs of the 6.4 keV ($EW_{6.4}$) and the 6.7 keV ($EW_{6.7}$) lines are given by the relation $EW_{6.7} + 0.50(\pm 0.06) \times EW_{6.4} = 0.62(\pm 0.07)[\text{keV}]$. Then, in the limit of $EW_{6.4} \rightarrow 0$, $EW_{6.7}$ was estimated to be 0.62 ± 0.07 keV. On the other hand, in the limit of $EW_{6.7} \rightarrow 0$, $EW_{6.4}$ is 1.2 ± 0.2 keV. They also made the GCDX-subtracted spectra of the two 6.4 keV clumps in the Sgr A region (source 1 and 2 in Koyama et al. 2009) and obtained consistent $EW_{6.4}$ values as those estimated from the phenomenological relation.

Stimulated by the successful approach of Koyama et al. (2009), we used the same method to decompose the GCDX in the Sgr C region into the 6.4-component and 6.7-component. Using the data in table 4.4, we plot the $EW_{6.4}$ and $EW_{6.7}$ relation of the six regions (figure 4.11). The outer region, the whole Sgr C and the background region for M 359.43–0.07 follow to, but the M 359.43–0.07 and M 359.47–0.15 regions come above the best-fit correlation line of the Sgr A region; these are systematically larger $EW_{6.4}$ than the Sgr A region. The best-fit linear relations between $EW_{6.7}$ and $EW_{6.4}$ for all cited regions except the whole Sgr C is;

$$EW_{6.7} + 0.22(\pm 0.12) \times EW_{6.4} = 0.53(\pm 0.06)[\text{keV}], \quad (4.2)$$

where the errors mean 90% confidence levels.

This relation indicates that $EW_{6.7}$ in the 6.7-component is 0.53 ± 0.06 keV (at $EW_{6.4} \rightarrow 0$) for the Sgr C region, consistent with that of the Sgr A region of 0.62 ± 0.07 keV (Koyama et al. 2009). On the other hand, $EW_{6.4}$ in the 6.4-component is $2.4^{+2.3}_{-0.7}$ keV (at $EW_{6.7} \rightarrow 0$), larger than those in the Sgr A region (Koyama et al. 2009).

Spectra of M 359.43–0.07 and M 359.47–0.15

From table 4.4, we see that the 6.7 keV line flux in M 359.43–0.07 and M 359.47–0.15 are almost identical to those of the respective background regions. The 6.7 keV flux differences are 16% and 6% of those in M 359.43–0.07 and M 359.47–0.15, respectively. Since the 6.7 keV line flux is a good indicator of the flux of the GCDX (Koyama et al. 2007b; 2009), we conclude that the background regions are properly selected within possible systematic error of 6–16%, which is smaller than the statistical errors.

Therefore we made the GCDX-subtracted spectra of these 6.4 keV clumps (figure 4.12). The energy-dependent vignetting were corrected by multiplying the effective-area ratio of the source region to corresponding background region for each energy bin of the GCDX spectra.

We first applied a model of a power-law and a narrow Gaussian line at 6.4 keV with absorption. The metal abundances of the inter stellar medium were fixed to the solar value (Anders & Grevesse 1989), while the center energy of the 6.4 keV line and its flux were free parameters. We simultaneously fit this model to the FIs and BI spectra, and found a line-like residual at 7.0–7.1 keV, with the flux of ~ 10 –20% of the 6.4 keV (Fe I $K\alpha$) line. From the energy and flux, the residual is likely to be the $K\beta$ of neutral Fe. We then added second narrow Gaussian for the Fe I $K\beta$ line, fixing its center energy to 1.103

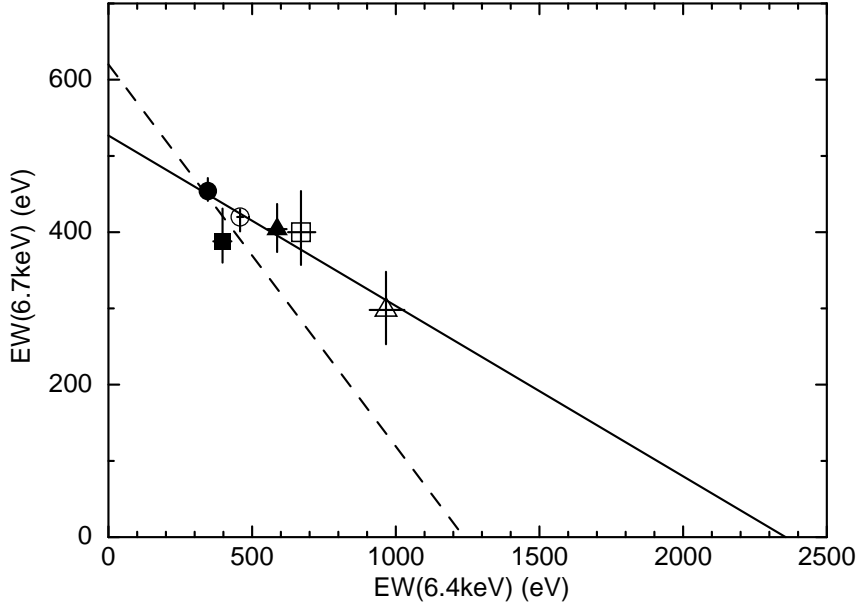


Figure 4.11: The correlation between the EWs of the Fe I- $K\alpha$ line ($EW_{6.4}$) and Fe XXV- $K\alpha$ line ($EW_{6.7}$). The dashed line shows the best fit relation in the Sgr A region (adopted from figure 2d of Koyama et al. 2009). The open and filled circle show the whole Sgr C region and the outer region, respectively. The source regions of M 359.43–0.07 and M 359.47–0.15 are plotted with the open square and triangle, while their background regions are given by the filled marks. The solid line is the best-fit relation for all regions except the whole Sgr C of $EW_{6.7} + 0.22 \times EW_{6.4} = 0.53$ [keV].

times of that of $K\alpha$. This model was accepted as is shown in figure 4.12, while the best-fit parameters are listed in table 4.5.

4.2.4 Discussion for the 6.4 keV Clouds in Sgr C

We detected four 6.4 keV clumps, M 359.43–0.07, M 359.47–0.15, M 359.43–0.12, and M 359.38–0.00 with Suzaku. From the former bright clumps, M 359.43–0.07 and M 359.47–0.15, we found $K\alpha$ and $K\beta$ -lines from Fe I. The most important fact is that EWs of the $K\alpha$ -lines are extremely large as ~ 2 keV (figure 4.12, table 4.5). These large EWs are independently supported by the analysis of the GCDX in the Sgr C regions (figure 4.11), and hence are highly reliable. We note that Yusef-Zadeh et al. (2007) reported small $EW_{6.4}$ from all the clumps, but their estimation was based on the spectra where no GCDX is subtracted.

Comparison with the Past X-Ray Observations

Murakami et al. (2001b) found excess emission at $(l, b) = (359.43^\circ, -0.04^\circ)$ in the X-ray image of the 5.8–7.0 keV band using the ASCA satellite. Although the energy resolution was limited, an emission line at the energy consistent with Fe I- $K\alpha$ line was found. Hence Murakami et al. (2001b) regarded this clump as an XRN.

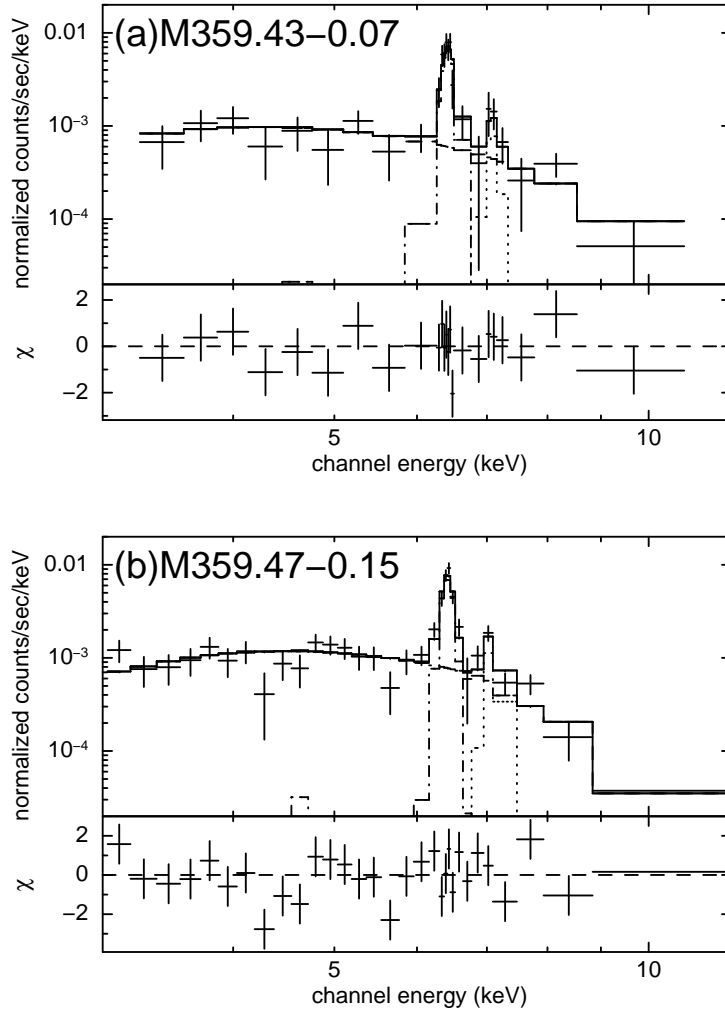


Figure 4.12: Same as figure 4.10, but for GCDX-subtracted spectra of M 359.43–0.07 (a) and M 359.47–0.15 (b). The $K\alpha$ and $K\beta$ emission lines of Fe I and power-law are shown by dot-dashed, dotted, and dashed lines, respectively.

The Suzaku source M 359.43–0.07 is located in the ASCA clump, but the peak position is systematically shifted. For comparison, we extracted the Suzaku spectrum from the same source and background regions as those of the ASCA clump (Murakami et al. 2001b). The background subtracted spectrum has the 6.4 keV line flux of $1.8_{-0.2}^{+0.3} \times 10^{-5}$ ph cm $^{-2}$ s $^{-1}$ (absorption uncorrected), which agrees with that of the ASCA clump ($3.5_{-2.2}^{+1.4} \times 10^{-5}$ ph cm $^{-2}$ s $^{-1}$). With Suzaku, we found that the surface brightness ratio of the 6.4 keV emission lines between the M 359.43–0.07, the ASCA clump and the outer background region are approximately 3 : 2 : 1 (1.9, 1.4, and 0.6 in the unit of 10^{-6} ph cm $^{-2}$ s $^{-1}$ arcmin $^{-2}$). Hence no significant detection of the full region of the ASCA clump in figure 4.9b may be due to its relatively lower surface brightness than M 359.43–0.07. On the other hand, no ASCA detection of M 359.43–0.07 is puzzling, although possible time variability can not be excluded. ASCA also detected no flux from

Table 4.5: The best-fit parameters of the spectral fittings to the background (GCDX) subtracted spectra of M 359.43–0.07 and M 359.47–0.15.

Parameter	M 359.43–0.07	M 359.47–0.15
Absorbed power-law model:		
Column density N_{H} (10^{23}cm^{-2})	0.92(0.48 – 1.41)	0.82(0.65 – 1.18)
Photon index	1.67(1.51 – 1.82)	1.61(1.52 – 1.86)
Gaussian 1 (Fe I $K\alpha$):		
Line energy (keV)	6.41(6.39 – 6.42)	6.41(6.40 – 6.42)
Line flux (10^{-6} ph cm^{-2} s^{-1}) *	6.43(5.27 – 7.39)	8.82(7.87 – 10.0)
Equivalent width (keV)	2.18(1.79 – 2.51)	1.96(1.75 – 2.23)
Gaussian 2 (Fe I $K\beta$):		
Line energy (keV) [†]	7.07	7.07
Line flux (10^{-6} ph cm^{-2} s^{-1}) *	1.05(0.43 – 2.14)	1.91(1.22 – 3.00)
Flux (10^{-13} erg cm^{-2} s^{-1}) [‡]	2.70	4.11
$\chi^2/\text{d.o.f.}$	27.92/41	49.67/46

90% confidence limits are in parentheses.

* Line fluxes are not corrected for the absorption.

† The line center is fixed so that the energy ratio is 1.103 ($K\beta/K\alpha=7.06\text{keV}/6.40\text{keV}$).

‡ Observed flux of the diffuse emission in the energy band of 3–10 keV. Absorption is not corrected.

the other bright Suzaku source M 359.47–0.15. However, this source is near the edge of the ASCA field.

The Suzaku spectrum of the whole Sgr C region (figure 4.8) shows the EWs of 458_{-10}^{+12} eV and 420_{-19}^{+10} eV for the 6.4 keV and 6.7 keV emission lines, respectively. The surface brightness in the 5–8 keV energy band is 7.1×10^{-14} erg cm^{-2} s^{-1} arcmin $^{-2}$. The Chandra analysis of the same region, in which point sources cataloged in the list of Munro et al. (2006) are excluded, shows that the EWs of the 6.4 keV and 6.7 keV emission lines are 460 ± 100 eV and ~ 400 eV, respectively. The surface brightness in the 5–8 keV band is $\sim 7.5 \times 10^{-14}$ erg cm^{-2} s^{-1} arcmin $^{-2}$ (figure 1b in Yusef-Zadeh et al. 2007). These are very similar to those of Suzaku, and hence point source contribution with the flux level larger than 1×10^{-13} erg cm^{-2} s^{-1} (Munro et al. 2006) may not be large, at least in the whole Sgr C region.

Detailed comparison in the smaller scale emission, however, shows significant differences. M 359.47–0.15 and a part of M 359.43–0.07 can be seen in the narrow band image at 6.4 keV with Chandra (left panel in figure 4.13; Yusef-Zadeh et al. 2007). However, M 359.43–0.07 is not found in the EW map of Chandra (right panel in figure 4.13; Yusef-Zadeh et al. 2007). This is a puzzle, because the Suzaku EW of M 359.43–0.07 is one of the largest among cited regions in the NXB-subtracted spectra. One possibility is a time variability as was found in Sgr B2 and Radio Arc regions (chapter 5 in this thesis; Munro et al. 2007; Koyama et al. 2008; Inui et al. 2009). In the Chandra image of the 2–6 keV band (figure 1a of Yusef-Zadeh et al. 2007), a clump named as G 359.45–0.07 is found. How-

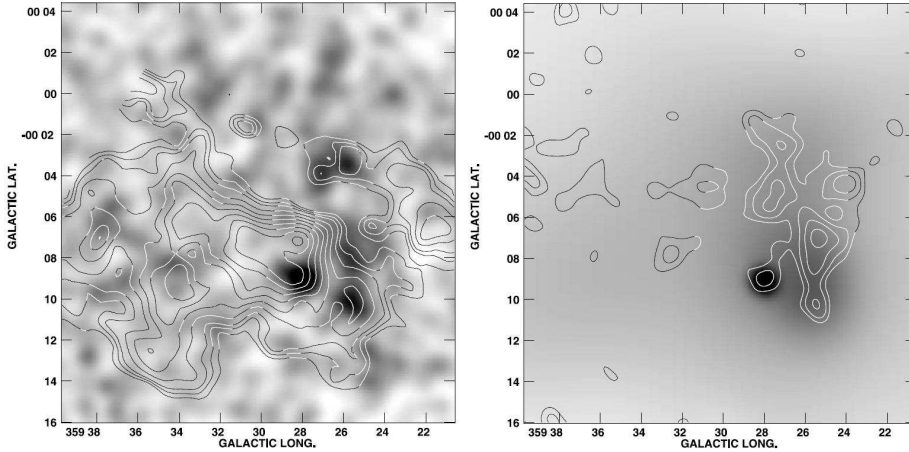


Figure 4.13: Left panel: Contours of velocity-integrated ^{13}CO emission between -77.2 and -22 km s^{-1} superimposed on a gray-scale 6.4 keV $\text{K}\alpha$ line emission with a $30''$ resolution taken by the Chandra satellite (figure 5a in Yusef-Zadeh et al. 2007). Right panel: Contours of X-ray continuum emission superimposed on a gray-scale equivalent width map of 6.4 keV line emission.

ever Suzaku found no excess in this region with the 6.4 keV line, and hence G 359.45–0.07 would not be 6.4 keV line emitter. Conversely no excess from M 359.38–0.00 is found with either Chandra or ASCA, possibly due to limited flux, and hence this is a new 6.4 keV clump found with the Suzaku satellite.

Ionization Mechanism

Two scenarios have been proposed for the origin of the 6.4 keV emission line from MCs in the GC region. One is X-ray photo ionization by external X-ray sources (the XRN scenario: Koyama et al. 1996; Sunyaev & Churazov 1998; Park et al. 2004). The other is the inner shell ionization by the impact of LECRe (the electron bombardment scenario: Valinia et al. 2000; Yusef-Zadeh et al. 2002). The LECRe scenario expects $EW_{6.4}$ of $\sim 300 \text{ eV}$ for the solar abundance Fe (table 3.3, see also Tatischeff 2003; Yusef-Zadeh et al. 2007), and hence is difficult to explain the observed large $EW_{6.4}$ of $\sim 2 \text{ keV}$, unless Fe is extremely over-abundant by a factor of 6–7. We found no observational evidence for such over-abundance. On the other hand, XRN scenario naturally explain the large $EW_{6.4}$ of the M 359.43–0.07 and M 359.47–0.15, and hence is more likely.

Photo-Ionization Source

Since the typical absorption toward GC is $\sim 0.6 \times 10^{23} \text{ H cm}^{-2}$ (Rieke et al. 1989; Sakano et al. 2002), intrinsic absorption depth of M 359.43–0.07 and M 359.47–0.15 are $\leq 0.8 \times 10^{23} \text{ H cm}^{-2}$ and $\leq 0.6 \times 10^{23} \text{ H cm}^{-2}$, respectively. The areas of M 359.43–0.07 and M 359.47–0.15 shown in figure 4.9b are 7 arcmin^2 , then their masses are estimated to be $\leq 4 \times 10^4$, $\leq 3 \times 10^4$ solar mass, respectively. From these masses and fluxes of the

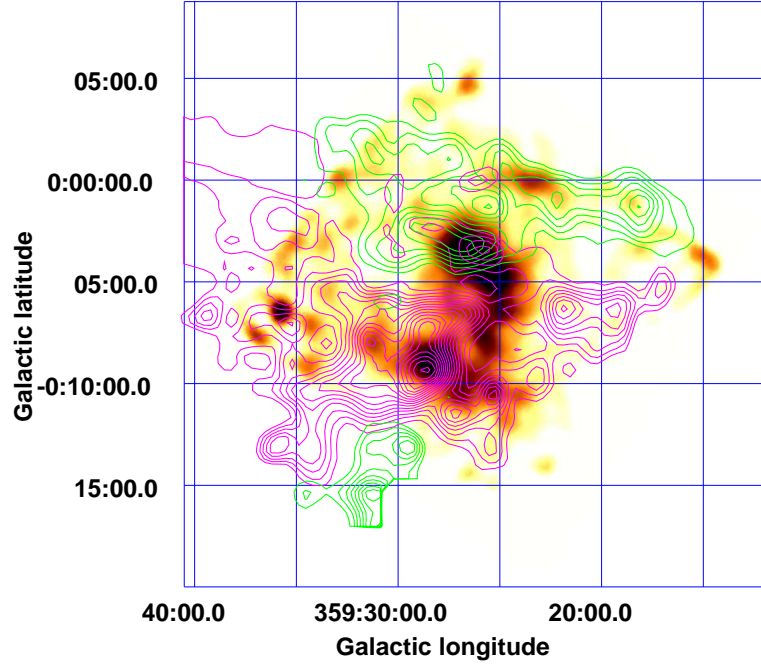


Figure 4.14: The contours of channel map of CS $J = 1 - 0$ emission line overlaid on the narrow band image at 6.4 keV shown in figure 4.9b. The first contour level and contour interval are 14.3 and 4.8 K km s⁻¹, respectively. Emission in the velocity ranges of -130 to -90 km s⁻¹ is shown with green and that of -80 to -30 km s⁻¹ is magenta, respectively.

6.4 keV lines, the luminosity of photo-ionizing source can be estimated following Sunyaev and Churazov (1998) as $\geq 1 \times 10^{38}$ erg s⁻¹ and $\geq 2 \times 10^{38}$ erg s⁻¹.

There is no X-ray object bright enough inside or nearby Sgr C region. Even the brightest near-by sources, KS 1741–293 and the Great Annihilator (1E 1740.7–2943) are impossible to explain this luminosity. Thus we arrive to the same conclusion for the 6.4 keV clumps origin near Sgr B2, a past Sgr A* activity of $\geq 1 \times 10^{38}$ erg s⁻¹ at 240 yr ago.

Comparison with the Molecular Line Observations

The absorption column derived from the background-subtracted spectra of M 359.43–0.07 and M 359.47–0.15 are $N_{\text{H}} \sim 1 \times 10^{23}$ H cm⁻². We require similar amounts of column in the MCs that corresponds to M 359.38–0.00 and M 359.43–0.12. Referring the CS molecular line map over the velocity range of $V_{\text{LSR}} = -200$ to $+200$ km s⁻¹ (Tsuboi et al. 1999, and the electric data), we searched for possible counterpart of the 6.4 keV clumps with $N_{\text{H}} \geq 10^{23}$ H cm⁻² (figure 4.14).

M 359.43–0.07 : MCs of $N_{\text{H}} \sim 10^{23}$ H cm⁻² are seen both in the velocity ranges of -50 to -70 km s⁻¹ (also Yusef-Zadeh et al. 2007) and -90 to -110 km s⁻¹ (also Murakami et al. 2001b).

M 359.47–0.15 : An MC with $N_{\text{H}} \geq 10^{23} \text{ H cm}^{-2}$ in the velocity range of -50 to -70 km s^{-1} exists in this region. M 359.47–0.15 is located in the western edge of -65 km s^{-1} MC as is also noticed by Yusef-Zadeh et al. (2007). There is no other MC of $\sim 10^{23} \text{ H cm}^{-2}$ in the other velocity range.

M 359.38–0.00 : No MC is seen in the -50 to -70 km s^{-1} band but an MC in the velocity range of -110 to -130 km s^{-1} is associated to the 6.4-keV clump; The column density of this radio cloud is roughly half of those in the directions of M 359.43–0.07 and M 359.47–0.15.

M 359.43–0.12 : There is a weaker peak in the -130 to -120 km s^{-1} band than that at M 359.38–0.00.

Sofue (1995) and Sawada et al. (2004) proposed that molecular gases in the GC region consists of two arms, Arm I and Arm II. The -130 to -90 km s^{-1} MC is physically associated with Arm I, while the -80 to -30 km s^{-1} MC is a part of Arm II. M 359.38–0.00 and M 359.47–0.15 belong to Arm I and Arm II, respectively, while M 359.43–0.07 has both possibilities. Since Arm II is located far side of Arm I (Sofue 1995; Sawada et al. 2004), X-rays from Sgr A* of several hundred years ago arrived at M 359.47–0.15 probably earlier than M 359.38–0.00.

4.2.5 Summary

1. We found four diffuse 6.4 keV clumps, M 359.43–0.07, M 359.47–0.15, M 359.43–0.12 and M 359.38–0.00 in the Sgr C region. The last one, M 359.38–0.00 is newly discovered.
2. The spectra of the two bright clumps, M 359.43–0.07 and M 359.47–0.15, have power-law of photon index of 1.6–1.7 with a very large $EW_{6.4}$ of 2.0–2.2 keV, the largest $EW_{6.4}$ among the 6.4 keV clumps in the GC.
3. The large $EW_{6.4}$ supports that the origin of 6.4 keV clumps is due to X-ray reflection irradiated by hard X-ray sources.
4. M 359.38–0.00 and M 359.47–0.15 possibly associate with MCs in different velocity ranges, indicating these are located in the different molecular arms.

Chapter 5

Discovery of Correlated Time-Variability between the Fe I K and Hard X-rays from Sgr B2

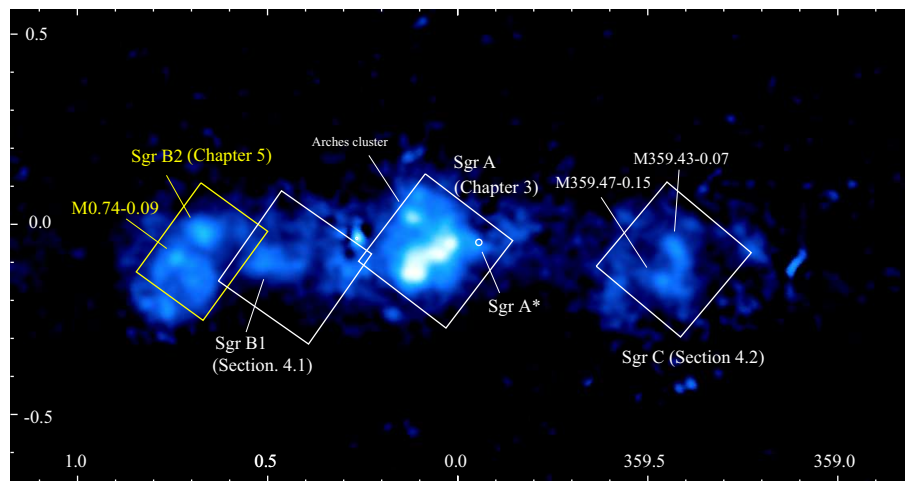


Figure 5.1: 6.4 keV image in the GC region, same as figure 3.1. In this chapter, we focus on two bright clumps in the Sgr B2 region indicated with the yellow boxed region.

5.1 Introduction

In the previous chapters 3 and 4, the external X-ray origin for the Fe I K line in the GC region was established by the large equivalent widths of the K-shell lines. Some molecular clouds "reflects" the X-rays from an external bright object (X-ray reflection nebula; XRN). Accordingly, we call X-rays from the MCs as "X-ray echo".

The more serious unresolved problem is "What and where the external X-ray source

is?”. One proposed scenario is that Sgr A*, the super-massive black hole with around 4 million solar masses (Ghez et al. 2008) in the GC located at a several hundred light-years distance from the molecular clouds (MCs) (Koyama et al. 1996; Murakami et al. 2000), was bright several hundred years ago with the X-ray luminosity millions times higher than the present one of 10^{33} – 10^{34} erg s⁻¹ (Baganoff et al. 2001).

Although the required luminosity of the external X-ray source depends on the distance to the MCs, the duration time of irradiating X-rays, and size and density of the MCs, current data were unable to exclude a possibility of intense X-ray flares of near-by transient sources. Also no clear evidence that Sgr A* was so bright in the past has been presented. Recently rapid time-variability of Fe I-K was discovered from some molecular clouds in the Sgr A and B2 regions (Muno et al. 2007; Koyama et al. 2008; Inui et al. 2009; Ponti et al. 2010). However, those observations were not enough to distinguish the verify the origin because the positions of the clouds are unknown and/or systematical uncertainties due to a combination of different instruments remain.

In order to identify the external X-ray source for the ”X-ray echo”, Sgr B2 has unique properties as, (i) Sgr B2 is one of the brightest 6.4 keV clouds, (ii) the 3-dimensional position is well determined (Ryu et al. 2009), and (iii) the Galactic center diffuse X-ray emission (GCDX: Koyama et al. 1996) is relatively small and uniform, and hence possible contamination from the GCDX can be reliably subtracted.

This chapter provides clear evidence for the scenario of a past big-flare of Sgr A*. Errors in this chapter are estimated at the 90% confidence level unless otherwise mentioned.

5.2 Observation and Data Reduction

We have observed the Sgr B region with the Suzaku/XIS. The observations were made two times in October 2005 and September 2009 at the identical pointing positions within 4”. Sequence numbers for the two observations are 100037060 and 504004020. The effective exposures in 2005 and 2009 were 21.3 hours and 56.1 hours, respectively. Four XIS (XIS0, 1, 2, and 3) and three XIS (XIS0, 1, and 3) cameras were available in 2005 and 2009, respectively. We discard the data obtained in a one fourth field (segment A) of XIS0 for both observations, which has become nonfunctional since June 2008.

Although the effective energy range of XIS is 0.2–10 keV, we use the 4–10 keV band data for the spectral analyses, because soft X-rays from the target (Sgr B) are absorbed by the interstellar medium toward the GC region. We construct the non-X-ray background (NXB) data caused by the cosmic-rays using `xisnxbgen` (Tawa et al. 2008) and subtracted the NXB from the observed data. We then corrected the local differences of the effective area for the data analyses (the vignetting correction).

5.3 Analysis

5.3.1 X-ray Images

Figure 5.2a shows X-ray images in the Fe I-K α (6.4 keV) line of the Sgr B region in 2005, where bright diffuse sources are clearly detected (Koyama et al. 2007b). Following

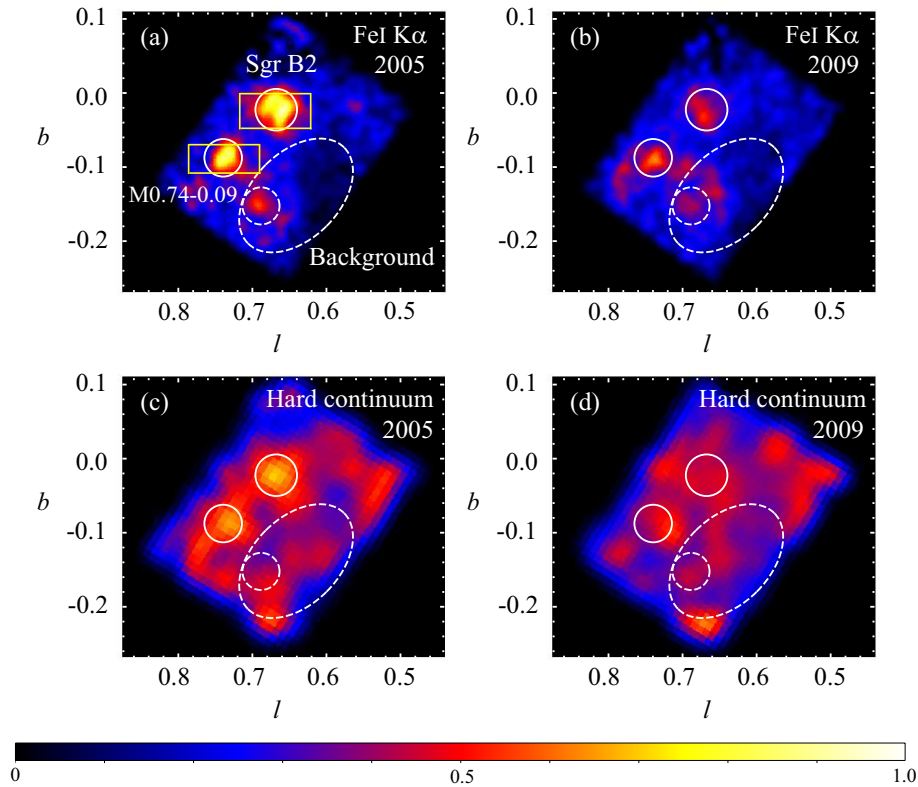


Figure 5.2: X-ray images near Sgr B2 and M0.74–0.09 in the field of view of $17.8' \times 13.4'$. The vertical and horizontal axes are the Galactic longitude (l) and latitude (b) in degree ($^\circ$), respectively. (a): The Fe I-K α (6.4 keV) band images in 2005. The bin size is $8.3''$ and is smoothed with a Gaussian kernel of $1\sigma=42''$. Profiles of the 6.4 keV line intensity in the Sgr B2 and M0.74–0.09 are taken from the yellow boxes (see text and figure 5.3). (b): The same as (a) but in 2009. (c): The hard continuum (8–10 keV) band images in 2005. The bin size is $33.3''$ and is smoothed with a Gaussian kernel of $1\sigma=100''$. (d) The same as (c) but in 2009. The source regions for the Sgr B2 and M0.74–0.09 spectra are shown in the white solid circles, centered at $(l, b) = (0.6676^\circ, -0.0226^\circ)$ with radius of $1.7'$ and $(l, b) = (0.7394^\circ, -0.087^\circ)$ with radius $=1.5'$, respectively. The background region is shown in the white dashed ellipse centered at $(l, b) = (0.6410^\circ, -0.1523^\circ)$ with the major and minor radii of $5.5'$ and $3.5'$, respectively. The inside white dashed circle at $(l, b) = (0.6885^\circ, -0.1523^\circ)$ with radius $=1.5'$ is excluded for the background region (see text). In this figure, 0.1° ($6'$) corresponds to 50 light-years. The color scale is arbitrarily adjusted for comparison.

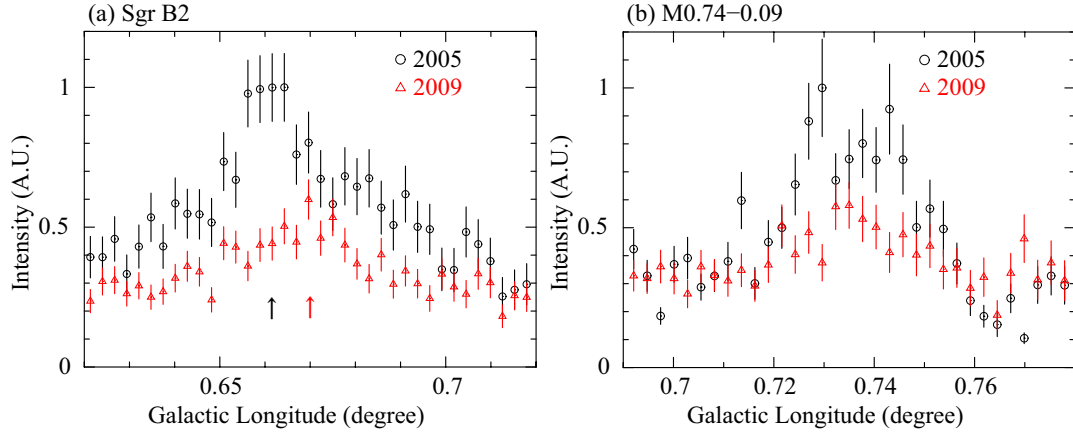


Figure 5.3: (a): Projected profile of the 6.4 keV line intensity in the Sgr B2 cloud ($l = 0.63^\circ\text{--}0.72^\circ$) extracted from the yellow box in figure 5.2. The integral interval is $b = -0.05^\circ\text{--}0.00^\circ$. The peak positions $l = 0.6610^\circ \pm 0.0027^\circ$ in 2005 and $l = 0.6692^\circ \pm 0.0056^\circ$ in 2009 are indicated with the black and red arrows, respectively. The peak position has shifted by $\Delta l = 0.0082^\circ \pm 0.0062^\circ$ at a 2.1σ confidence level. (b): Same as (a), but in the M0.74–0.09 cloud. The integral interval is $b = -0.11^\circ\text{--}0.07^\circ$. We do not find the peak shift ($\Delta l = 0.0045^\circ \pm 0.0110^\circ$).

the naming by the previous work (Koyama et al. 2007b), we hereafter refer to the two sources as Sgr B2 and M0.74–0.09. Figure 5.2b shows the same image but taken 4 years later in 2009. Comparing the two images, we find that the two bright sources have darkened in the 4 years, whereas no significant change of the brightness is in the surrounding region. We also find that the peak position (the Galactic longitude) of Sgr B2 in 2005 is $l = 0.6610^\circ \pm 0.0027^\circ$, while that in 2009 is $l = 0.6692^\circ \pm 0.0056^\circ$. Thus, the peak position has shifted by $\Delta l = 0.0082^\circ \pm 0.0062^\circ$ at a 2.1σ confidence level in 4 years. No significant shift is found in the Galactic latitude (b) direction. Then the shift corresponds to 4.0 ± 3.0 light-years toward the east direction, which indicates that the shift speed is consistent with the light-velocity. For M0.74–0.09, a peak shift is not found ($\Delta l = 0.0045^\circ \pm 0.0110^\circ$).

We also make the hard X-ray images of the Sgr B region in the 8–10 keV band for the 2005 and 2009 observations in figure 5.2c and 5.2d, respectively. As shown in figure 5.2c, we find hard X-ray excesses at the positions of Sgr B2 and M0.74–0.09 in 2005. This is the first resolved hard X-ray image of Sgr B2 and M0.74–0.09, although the hard X-ray excess near Sgr B2 has been found with insufficient spacial resolution of $12'$ by the past X-ray observation (Terrier et al. 2010). On the other hand, the hard X-ray fluxes from these MCs are almost comparable to those of the surrounding areas and hence no significant hard X-ray excesses are found in the 2009 data (see figure 5.2d). These facts suggest that the hard X-rays from Sgr B2 and M0.74–0.09 decreased from 2005 to 2009, in correlation to the decrease of the Fe I-K fluxes.

5.3.2 Spectra

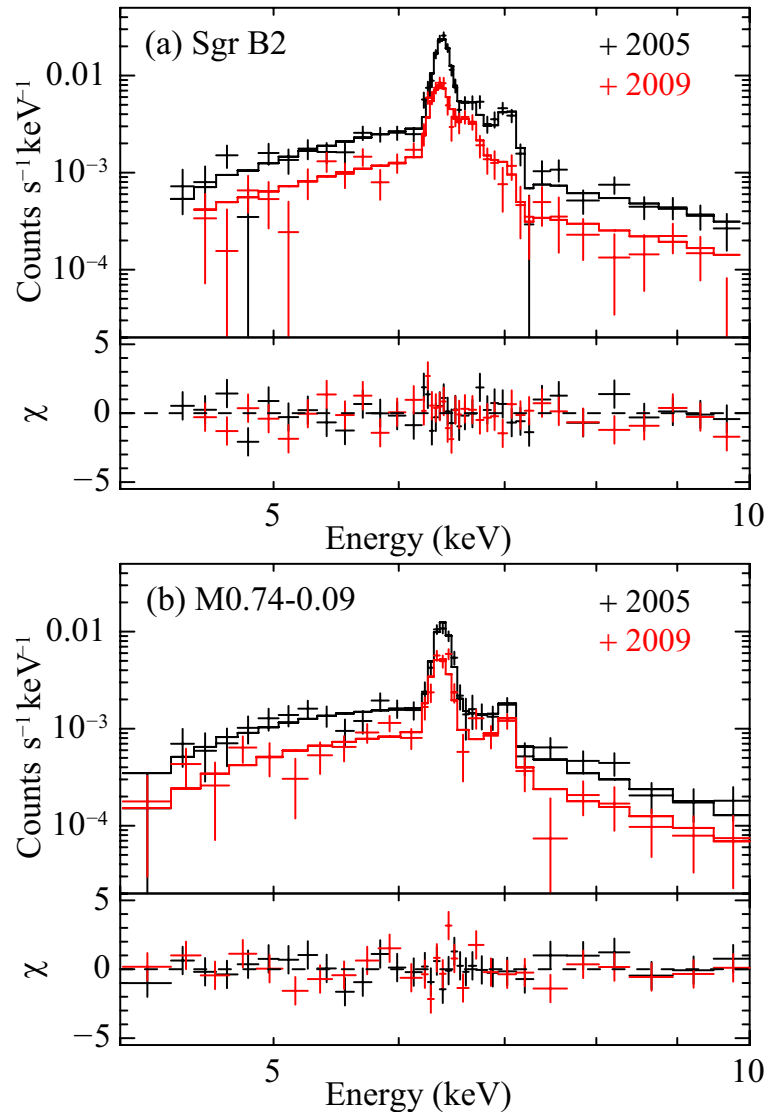


Figure 5.4: X-ray spectra of Sgr B2 (a) and M0.74–0.09 (b). Spectra of the 2005 observation and those of the 2009 observation are indicated with the black and red crosses, respectively. The best-fit models are shown with the solid histograms. Residuals between the observed data and the models are shown in the bottom panels of (a) and (b).

We investigate the X-ray spectra to study the time variability more quantitatively. The regions selected for the Sgr B2 and M0.74–0.09 spectra are indicated with the white solid lines in figure 5.2. The background region is also shown with the white dashed lines, where the dashed small circle in which a MC might be emitting the faint Fe I-K emission is excluded. Figure 5.4a and 5.4b are the background-subtracted spectra of Sgr B2 and M0.74–0.09, respectively. The spectra in 2005 and 2009 are shown by black and red crosses, respectively. As seen in the both spectra, the fluxes of the Fe I-K α line and the hard continuum have simultaneously decreased from 2005 to 2009.

Table 5.1: Best-fit parameters.*

Source (Year)	N_{H}	Fe I $K\alpha$	Fe I $K\beta$	5–10 keV
unit	10^{23} cm^{-2}	$10^{-5}\dagger$	$10^{-5}\dagger$	$10^{-12}\ddagger$
Sgr B2 (2005)	8.4 ± 1.4	13.6 ± 1.1	1.3 ± 0.5	4.3 ± 0.8
Sgr B2 (2009)	8.8 ± 2.2	5.2 ± 0.8	<0.6	2.1 ± 0.5
M 0.74–0.09 (2005)	5.7 ± 0.6	5.1 ± 0.6	0.4 ± 0.3	1.7 ± 0.3
M 0.74–0.09 (2009)	6.5 ± 1.9	2.7 ± 0.5	0.5 ± 0.3	0.9 ± 0.3

* The error ranges in this table are calculated at the 90% confidence level.

† Absorption-corrected value in the unit of photons $\text{s}^{-1} \text{ cm}^{-2}$.

‡ Absorption-corrected flux of the continuum excluding the Fe I K lines. The unit is $\text{ergs s}^{-1} \text{ cm}^{-2}$.

We fit the spectra with a phenomenological model of an absorbed power-law plus Fe I- $K\alpha$ and Fe I- $K\beta$ lines at 6.4 keV and 7.06 keV, respectively. A supernova remnants (SNR) candidate G 0.61+0.01 (Koyama et al. 2007b) is located $4'$ away from Sgr B2, and may slightly contaminate the Sgr B2 spectrum. We therefore take into account the contamination of the thermal plasma of G 0.61+0.01, by adding a plasma model (Mazzotta et al. 1998) with fixed temperature of $kT = 3.2$ keV and iron abundance $Z_{\text{Fe}} = 5.1$ solar (Koyama et al. 2007b). Then the contamination is found to be less than 10%, and hence the error due to possible uncertainty of the contaminated flux can be ignored.

The four spectra (Sgr B2 and M 0.74–0.09 for 2005 and 2009) are simultaneously fitted with free parameters of the absorption column density N_{H} , the iron abundance Z_{Fe} , the photon index Γ , and the fluxes of the continuum and the Fe I-K lines. Among them, only Z_{Fe} and Γ are set to be common for all the spectra. The fit is acceptable with $\chi^2/\text{d.o.f.}$ of 216/217 (null hypothesis probability=0.6). The best-fit common parameters of Z_{Fe} and Γ are 1.3 ± 0.5 solar and 2.5 ± 0.9 , respectively. Those of the other free parameters are listed in table 5.1.

We find that the fluxes of Fe I- $K\alpha$ and the hard continuum band for Sgr B2 decrease by a factor of 0.39 ± 0.06 and 0.49 ± 0.15 from 2005 to 2009, respectively. These variation factors are consistent within the 1σ confidence level with the mean value of 0.41 ± 0.06 . The variation factors of 0.53 ± 0.10 (Fe I- $K\alpha$) and 0.53 ± 0.21 (continuum band) for M 0.74–0.09 are also consistent with the mean value of 0.53 ± 0.09 .

5.4 Discussion for the 6.4 keV Clouds in Sgr B2

We confirmed with the 2005 data that the two MCs (Sgr B2 and M 0.74–0.09) exhibit intense Fe I-K lines. Clear excesses of the hard continuum (8–10 keV) from the MCs are found for the first time. The most important discovery is the correlated decrease in 4 years between the Fe I-K lines and the hard continuum in the two MCs. Since the data for these results are obtained with the same instrument (Suzaku/XIS) and the identical pointing field, possible systematic errors would be minimized. The correlated fluxes change in the two MCs and the two components (Fe I-K and hard continuum) immediately indicate that

they are in a common origin.

As we have already discussed, the origin is likely to be an X-ray irradiation by an external source ("X-ray echo"). Then the equivalent width of the Fe I-K α line ($EW_{6.4\text{keV}}$) is expressed as $1.0 \times (Z_{\text{Fe}}/1 \text{ solar}) \text{ keV}$ (chapter 3 in this thesis; Tatischeff et al. 2003; Nobukawa et al. 2010). Since the observed $EW_{6.4\text{keV}}$ is 1.0–1.5 keV, we derive the iron abundance as $Z_{\text{Fe}}=1.0\text{--}1.5 \text{ solar}$. The absorption column density N_{H} of about 10^{24} cm^{-2} is significantly higher than the value of 10^{23} cm^{-2} for typical sources in the GC (Muno et al. 2004), and hence the major fraction would be due to the absorption inside the MCs. The depth of the iron absorption edge at 7.1 keV gives the iron abundance in the MCs of $Z_{\text{Fe}}=1.3 \pm 0.5 \text{ solar}$, which is consistent with that derived from the $EW_{6.4\text{keV}}$. These facts firmly support the "X-ray echo" for the X-ray emission from Sgr B2 and M0.74–0.09: the fluorescent Fe I-K line and the Thomson-scattered hard-continuum.

We find that the position of the "X-ray echo" in Sgr B2 had shifted for 4 light-years during 4 years toward the east direction, and the fluxes of Sgr B2 and M0.74–0.09 had dropped by factors of 0.41 ± 0.6 and 0.53 ± 0.09 , respectively. These results indicate that the X-ray irradiating source had flared up in duration of shorter than 4 years, and was located in the GC direction with respect to Sgr B2.

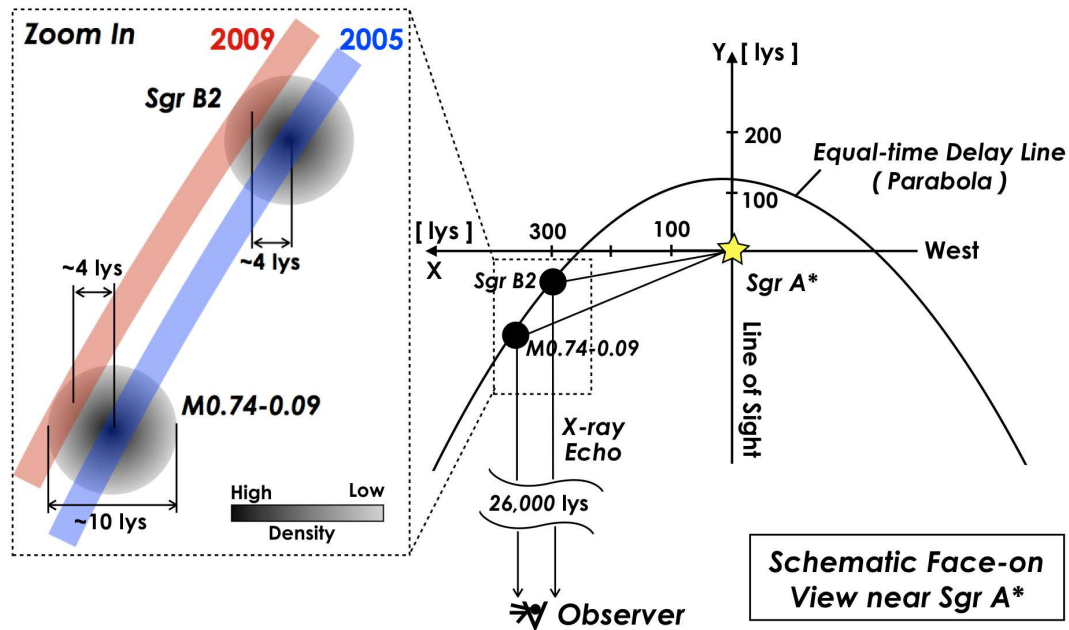


Figure 5.5: Schematic face-on view of movement of "X-ray echoes" in the molecular clouds. The irradiating source, i.e. the super-massive black hole Sgr A* is indicated with the yellow star. The line-of-sight positions of Sgr B2 and M0.74-0.09 are adopted from results by the previous work (Ryu et al. 2009). The solid parabola guides eyes to see the X-ray echoes from Sgr B2 and M0.74-0.09 arriving at the observer at the same time (equal-time delay line). The unit of distance is in light-years (lys).

The schematic view of the "X-ray echo" scenario is shown in figure 5.5. As the incident X-ray flare moves at light speed in the MCs, the bright spot also moves. Since the

density of the MCs is not uniform, brightness of the X-ray echoes would be higher in high-density regions than those in low-density regions. The X-ray echoes in 2005 would be produced in high-density regions, and then moved into low-density regions in 2009. In fact, the radio observation reported a dense region at $l = 0.664^\circ \pm 0.001^\circ$ (Sato et al. 2000), which is almost coincident with the position of the bright spot of Sgr B2 in 2005 ($l = 0.661^\circ \pm 0.003^\circ$). The darker spot at $l = 0.669^\circ$ in 2009 means that probably the echo had already passed the dense region.

The required luminosity (L_X) of the X-ray flare to produce the "X-ray echo" of the MCs depends on the duration time (t) of the flare, the distances (d) to the MCs, and the optical depths (τ) along the X-ray pass in the MCs. To be more exact, L_X also depends on the density profiles and the sizes of MCs. We here approximate these fine-tuning factors by a single parameter N_H . Using the observed N_H of about 10^{24} cm^{-2} , τ is estimated to be about 0.1. Then we can estimate L_X from Sunyaev et al. (1998); Ryu et al. (2009) as,

$$L_X = 6 \times 10^{40} \left(\frac{t}{\text{year}} \right)^{-1} \left(\frac{d}{300 \text{ ly}} \right)^2 \text{ erg s}^{-1}. \quad (5.1)$$

We have already noted that the X-ray flare source should be located in the west of Sgr B2. The minimum value of the required luminosity is therefore given when the flare-source is near the west-rim of Sgr B2. In this case, the distance d to the other MC, M0.74–0.09 is about 0.1° , or 50 light-years (see figure 5.2). Since the observed duration time t is shorter than 4 years, the minimum value of the required luminosity is $L_X = 4 \times 10^{38} \text{ erg s}^{-1}$. Equation (5.1) is derived from the simple assumptions and approximations, and hence some uncertainties exist in $L_X = 4 \times 10^{38} \text{ erg s}^{-1}$ but the errors should not be larger than one order of magnitude.

The most conservative value of L_X is $4 \times 10^{37} \text{ erg s}^{-1}$, which is nearly equal to or higher than those of the brightest X-ray sources in our Galaxy. Since we found no such stable source in the GC, one possible candidate is a transient X-ray binary system. The X-ray monitoring in the GC has been continuing for nearly 10 years with the INTEGRAL satellite (Jensen et al. 2003). All the bright transient sources had the peak luminosities lower than a few times of $10^{37} \text{ erg s}^{-1}$ (Sakano et al. 2002; Werner et al. 2003). Moreover, the flare durations (t) are shorter than 0.1 years (Sakano et al. 2002; Werner et al. 2003). The averaged luminosity of transient sources for 4 years are not larger than $10^{36} \text{ erg s}^{-1}$, which is 40 times lower than the minimum required luminosity by the most conservative estimation.

These facts relegate the transient binary to an implausible candidate for the irradiating source. We therefore reach the unique conclusion of a big-flare of Sgr A*, the super-massive black hole. Since d (Sgr B2 to Sgr A*) is 300 light-years (figure 5.5), the big-flare with the luminosity of larger than $1.5 \times 10^{40} \text{ erg s}^{-1}$ had occurred about 300 years ago. The flare duration was shorter than 4 years. At present, the X-ray luminosity of Sgr A* is about $10^{34} \text{ erg s}^{-1}$ and exhibits many flares, but the flare scales are relatively small and at most 50 times with respect to the quiescent level (Baganoff et al. 2001). Our predicted big-flare, which is more than 10^4 times bigger than the biggest flare observed so far, would be new evidence for the past high activity of the super-massive black hole at the center of our Galaxy.

Chapter 6

Discussion

6.1 Features of the 6.4 keV Clouds

We observed the clouds emitting the strong Fe I K (6.4 keV) lines in the GC region with the Suzaku/XIS, and studied the detailed features of the clouds. Two possible origins of the Fe I K lines were proposed so far: ionization of neutral atoms due to low energy cosmic-ray electrons (LECRE) with 10–100 keV (Valinia et al. 2000; Yusef-Zadeh et al. 2007), and photo-ionization due to external X-rays (X-ray reflection nebula: XRN) (e.g. Koyama et al. 1996; Sunyaev et al. 1998).

We found that the X-ray spectra produced by the two scenarios have large difference in equivalent widths of emission lines. In chapter 3, we predicted that the equivalent width of Fe I K α to be ~ 0.3 keV and ~ 1 keV in the LECRe and XRN scenarios, respectively. Those values for the other atoms were shown in figure 3.8 and table 3.3. From the Suzaku data, we obtained that equivalent widths of the Fe I K α line were large (1–2 keV) for all clouds. The fact indicates that the X-ray emission from the 6.4 keV clouds is due to the X-ray origin (chapter 3, 5, and 4).

Best-fit parameters of the 6.4 keV clouds analyzed in this thesis are shown in table 6.1. The other 6.4 keV clouds, G 0.174–0.233 and M 359.23–0.04 were found by Fukuoka et al. (2009) and Nakashima et al. (2010), respectively. These sources are shown in figure 6.1. G 0.174–0.233 is at $(l, b) \sim (0.2^\circ, 0.2^\circ)$, $\sim 20'$ southeast apart from Sgr A*. M 359.23–0.04 is at $(l, b) \sim (359.2^\circ, 0.0^\circ)$, to the west side from Sgr C. These clouds have also large equivalent widths ~ 1 keV of Fe I K α , and hence are suspected to be XRNe (Fukuoka et al. 2009; Nakashima et al. 2010) The obtained parameters are also listed in table 6.1 for this discussion.

The observed equivalent width may suggest that Fe is abundant in each cloud compared with the solar value. In particular, since M 359.43–0.07 and M 359.47–0.15 have the large equivalent widths of the 6.4 keV lines, the Sgr C region is rich in Fe, whose abundance is larger than 2 solar.

Table 6.1: Best-fit parameters of various 6.4 keV clouds studied in this thesis.

Value	$I_{6.4\text{keV}}^\dagger$	EW	N_{H}	Γ	n^{\S}	$d_{\text{proj}}^{\parallel}$	$d^{\#}$	L_{req}^{**}
Unit	$10^{-5} \text{ ph s}^{-1} \text{ cm}^{-2}$	keV	10^{-23} cm^{-2}	cm^{-2}	H cm^{-3}	pc	pc	erg s^{-1}
Sgr A	34.0 ± 1.0	1.15 ± 0.09	1.9 ± 0.1	1.87 ± 0.04	4×10^3	30	50	2×10^{40}
Sgr B2	13.6 ± 0.7	1.3 ± 0.2	8.4 ± 0.9	2.5 ± 0.6	4×10^4	110	110	1.5×10^{40}
M 0.74–0.09	5.1 ± 0.4	1.3 ± 0.3	5.7 ± 0.4	2.5^\dagger	3×10^4	120	170	2×10^{40}
Sgr B1	$2.8_{-0.4}^{+0.2}$	1.4 ± 0.3	$1.5_{-0.1}^{+0.2}$	$1.8_{-0.5}^{+0.4}$	3×10^3	90	90	3×10^{40}
M 359.43–0.07	$6.4_{-1.1}^{+1.0}$	$2.2_{-0.4}^{+0.3}$	$0.9_{-0.4}^{+0.5}$	$1.7_{-0.2}^{+0.1}$	$\sim 5 \times 10^3$	75	75	3×10^{40}
M 359.47–0.15	$8.8_{-0.9}^{+1.2}$	$2.0_{-0.2}^{+0.2}$	$0.8_{-0.1}^{+0.4}$	$1.6_{-0.1}^{+0.3}$	$\sim 5 \times 10^3$	75	75	3×10^{40}
G 0.174–0.233 [†]	0.6 ± 0.1	1.0 ± 0.2	0.8 ± 0.2	$1.7_{-0.2}^{+0.1}$	$\sim 1 \times 10^3$	50	75	3×10^{40}
M 359.23–0.04 [†]	$3.4_{-0.8}^{+0.6}$	$1.2_{-0.4}^{+0.2}$	$3.1_{-1.2}^{+0.4}$	$2.9_{-0.7}^{+0.6}$	7×10^3	100	100	2×10^{40}

* Errors are given at the 90% confidence levels.

[†] The parameters of G 0.174–0.233 and M 359.23–0.04 are referred to Fukuoaka et al. (2009) and Nakashima et al. (2010), respectively.

[‡] Absorption-corrected intensity of the 6.4 keV line.

[§] Hydrogen densities in the clouds.

^{||} Projected distance to the super-massive black hole, Sgr A*.

[#] Actual distance to Sgr A* on the assumption that the clouds align on the paraboloidal surface (see text).

* Required luminosity for the 6.4 keV line if the irradiating source is Sgr A*.

^{††} Linked to the same value with that of Sgr B2.

The observed absorption column densities N_{H} are 10^{23} – 10^{24} cm^{-2} for the clouds. The N_{H} values are larger than that of the interstellar matter in the GC region (0.6×10^{23} cm^{-2}) (Predehl & Schmitt 1995; Munro et al. 2006). The large N_{H} should reflect the dense matter in the clouds. Number densities n in the clouds can be roughly estimated from the observed N_{H} and surface areas S if the clouds are like a sphere. The density is described as $n = N_{\text{H}}/\sqrt{S}$, and is shown in table 6.1.

6.2 Irradiating Source of the 6.4 keV Clouds

We do not know whether a single object illuminates all the 6.4 keV clouds or not. Bright X-ray binaries are found in the GC region. We may consider the possibility of a scenario that the 6.4 keV clouds are illuminated by different objects. However, only one cloud, M 359.23–0.04, accompanies with a bright source (Great Annihilator) with enough luminosity to explain the observed Fe I $K\alpha$ flux (Nakashima et al. 2010). Thus, this scenario seems to be unlikely.

On the other hand, in the case of the single origin, the irradiating source should exist at the central region since the clouds are distributed on the east (Sgr B1, B2) and west (Sgr C) regions with respect to the GC. Moreover, the peak shift of the Sgr B2 cloud also favors this idea that the source is near the GC (chapter 5). We estimated the required luminosity $L_{\text{req}} > 10^{40}$ erg s^{-1} for the Sgr B2 cloud in chapter 5. The source with the high luminosity should have a large mass of $> 50 M_{\odot}$ because the Eddington luminosity is $L_{\text{Edd}} = 2 \times 10^{38} M_{\odot} \text{ erg s}^{-1}$. Hence the super-massive black hole, Sgr A*, with the huge mass of $\sim 4 \times 10^6 M_{\odot}$ is the only plausible candidate.

From the two Suzaku observations with 4 years interval, we discovered the time variability of the X-ray emission from the Sgr B2 clouds (chapter 5). The fact suggests that the external irradiation was not made persistently but instantaneously, and hence Sgr A* had flared up for the duration time < 4 years in the past. We examine whether the single flare of Sgr A* simultaneously illuminated all the 6.4 keV clouds including the others than the Sgr B2 cloud.

According to Sunyaev et al. (1998), the required luminosity of the irradiating source is described as,

$$L_{\text{req}} = 5 \times 10^{40} \left(\frac{I_{6.4 \text{ keV}}}{10^{-5}} \right) \left(\frac{n}{10^3 \text{ cm}^{-3}} \right)^{-1} \left(\frac{d}{100 \text{ pc}} \right)^2 \left(\frac{\Delta t}{4 \text{ yr}} \right)^{-1} \text{ erg s}^{-1}. \quad (6.1)$$

$I_{6.4 \text{ keV}}$ are the 6.4 keV line intensity in the unit of photons $\text{s}^{-1} \text{ cm}^{-2}$. A hydrogen number density n in the clouds. d is a distance between the 6.4 keV cloud and the irradiating source. Δt is the duration time for which the external source irradiates the cloud.

The distances d to the irradiating source for 6.4 keV clouds are not all known, while Ryu et al. (2009) estimated the relative position of the Sgr B2 cloud to Sgr A* (see figure 5.5). On the assumption of the single flare origin, total passes in which X-rays from Sgr A* reach the clouds and then the generated 6.4 keV X-rays arrive at an observer (the Suzaku satellite) should be the same. Then, the 6.4 keV clouds should align on the same paraboloidal surface plotted in figure 6.2, on the basis of the position of the Sgr B2 cloud.

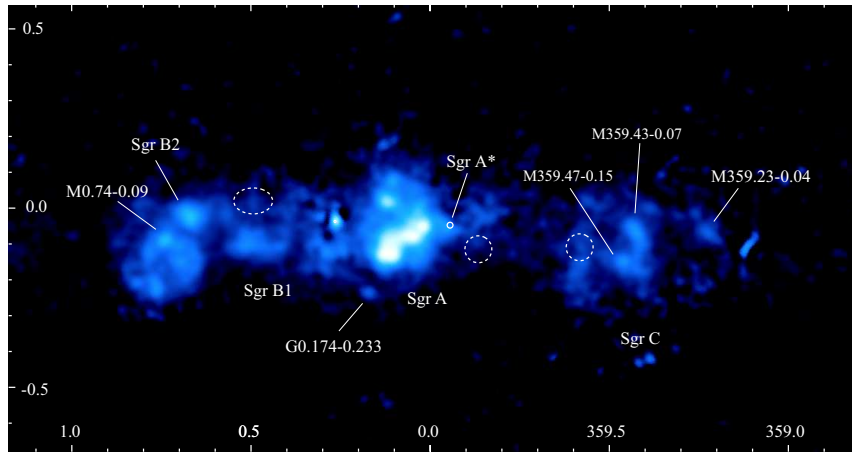


Figure 6.1: X-ray image of the GC region in the 6.4 keV line, same as figure 3.1. Dashed regions indicated molecular clouds found by the radio observations but with no 6.4 keV emission.

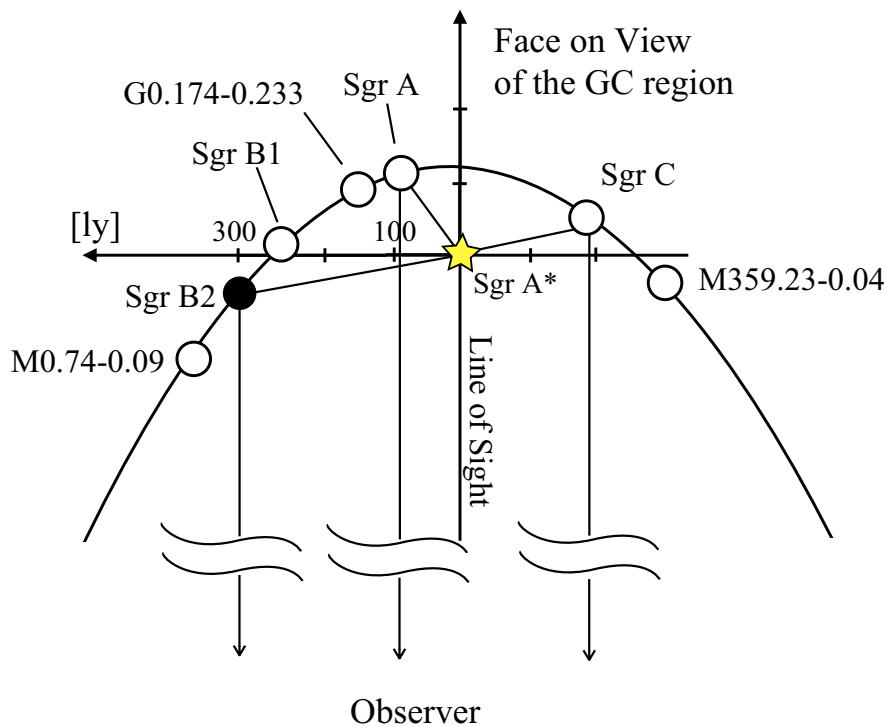


Figure 6.2: Schematic face-on view of distribution of the molecular clouds emitting the 6.4 keV line if the irradiating source is a single big flare of the super-massive black hole, Sgr A*, which is marked with the yellow star. The solid curve is a parabola on which the light passes of all molecular clouds (open circles) are equal to that of Sgr A*—Sgr B2 (filled circle)—observer.

The actual distances d are estimated from the distribution. According to the result in the Sgr B2 observations (chapter 5), the duration time of the past flare is assumed to be 4 years in the following discussion. As stated in the discussion of chapter 5, we note that there are some uncertainties in the estimation but the errors should not be larger than one order of magnitude.

We estimated the required luminosity L_{req} for the 6.4 keV clouds by the above equation (6.1) and described the results in table 6.1. The L_{req} of all the clouds are $\sim 1\text{--}3 \times 10^{40}$ erg s $^{-1}$. Thus, the single origin of the Sgr A* flare successfully explains the observed results.

Sofue (1990) mentioned a giant molecular cloud with $2 \times 10^6 M_{\odot}$ at $(l, b) = (0.52^{\circ}, -0.05^{\circ})$ to the north of the Sgr B1 cloud in a radio observation of ^{13}CO emission line (Bally et al. 1987). The large mass is comparable to that of the Sgr B2 cloud, but we have found no X-ray emission at the corresponding position. By a radio observation, Tsuboi et al. (1999) found a giant molecular cloud at $(l, b) = (359.55^{\circ}, -0.05^{\circ})$ in the Sgr C region. However, the radio cloud is $\sim 0.1^{\circ}$ apart from the 6.4 keV clouds, M 359.43–0.07 or M 359.47–0.15 and is dim in X-ray. A giant molecular cloud without 6.4 keV emission has been also found at $(l, b) \sim (-359.85^{\circ}, -0.10^{\circ})$, whose projected distance to Sgr A* is about 0.1° (Sofue 1990; Tsuboi et al. 1999). Velocities obtained from the Doppler shift of the molecule lines suggest that these molecular clouds exist in the GC region. The X-ray flare of Sgr A* might have already pass over those molecular clouds or have not reached them.

Acknowledgement

I would like to express my sincere gratitude to my supervisor, Prof. Koyama for providing me this precious study opportunity as a Ph.D student in his laboratory. My deepest appreciation goes to my supervisor, Prof. Tsuru for his elaborated guidance, considerable encouragement and invaluable discussion that make my research of great achievement and my study life unforgettable.

I am very grateful to members of the present and past cosmic-ray laboratory.

I would also like to express my gratitude to my family for their moral support and warm encouragements.

References

- [1] Aharonian, F., et al. 2006, *Nature*, 439, 695
- [2] Anders, E., & Grevesse, N. 1989, *Geochim. Cosmochim. Acta*, 53, 197
- [3] Baganoff, F. K., et al. 2001, *Nature*, 413, 45
- [4] Baganoff, F. K., et al. 2003, *ApJ*, 591, 891
- [5] Balick, B., & Brown, R. L. 1974, *ApJ*, 194, 265
- [6] Bałucińska-Church, M., & McCammon, D. 1992, *ApJ*, 400, 699
- [7] Bautz, M. W., et al. 1998, *proc. SPIE*, 3444, 210
- [8] Bautz, M. W., Kissel, S. E., Prigozhin, G. Y., LaMarr, B., Burke, B. E., & Gregory, J. A. 2004, *Proc. SPIE*, 5501, 111
- [9] Bautz, M. W., et al. 2007, *Proc. SPIE*, 6686, 66860Q
- [10] Beckert, T., Duschl, W. J., Mezger, P. G., & Zylka, R. 1996, *A&A*, 307, 450
- [11] Bleach, R. D., Boldt, E. A., Holt, S. S., Schwartz, D. A., & Serlemitsos, P. J. 1972, *ApJ*, 174, L101
- [12] Blumenthal, G. R., & Gould, R. J. 1970, *Rev. Mod. Phys.*, 42, 237
- [13] Brinkmann, W., Kawai, N., Matsuoka, M., & Fink, H. H. 1991, *A&A*, 241, 112
- [14] Burke, B. E., Gregory, J. A., Bautz, M. W., Prigozhin, G. Y., Kissel, S. E., Kosicki, B. B., Loomis, A. H., & Young, D. J. 1997, *IEEE Transactions on Electron Devices*, 44, 1633
- [15] Burke, B. E., Mountain, R. W., Doniels, P. J., Cooper, M. J., Dolat, V. S. 1993, *Proc. SPIE Vol. 2006*, p. 272-285, *EUV, X-Ray, and Gamma-Ray Instrumentation for Astronomy IV*, Oswald H. Siegmund; Ed.
- [16] Cooke, B. A., Griffiths, R. E., & Pounds, K. A. 1969, *Nature*, 224, 134
- [17] Cremonesi, D. I., Mereghetti, S., Sidoli, L., & Israel, G. L. 1999, *A&A*, 345, 826
- [18] Del Santo, M., Sidoli, L., Bazzano, A., Cocchi, M., De Cesare, G., Paizis, A., & Ubertini, P. 2006, *A&A*, 456, 1105

- [19] Dutra, C.M., & Bica, E. 2000, *A&A*, 359, L9
- [20] Eisenhauer, F., et al. 2003, *ApJL*, 597, L121
- [21] Eyles, C. J., Skinner, G. K., Willmore, A. P., & Rosenberg, F. D. 1975, *Nature*, 257, 291
- [22] Fukuoka, R., Koyama, K., Ryu, S. G., & Tsuru, T. G. 2009, *PASJ*, 61, 593
- [23] Garmire, G. P., et al. 1992, in *AIAA, Space Programs and Technologies Conference (Paper 92-1473)* (New York: AIAA)
- [24] Genzel, R., Pichon, C., Eckart, A., Gerhard, O. E., & Ott, T. 2000, *MNRAS*, 317, 348
- [25] Ghez, A. M., Morris, M., Becklin, E. E., Tanner, A., & Kremenek, T. 2000, *Nature*, 407, 349
- [26] Ghez, A., M., et al. 2003, *ApJ*, 586, 127L
- [27] Ghez, A., M., Salim, S., Hornstein, S. D., Tanner, A., Lu, J. R., Morris, M., Becklin, E. E., & Duchene, G. 2005, *ApJ*, 620, 744
- [28] Ghez, A. M., et al. 2008, *ApJ*, 689, 1044
- [29] Ginzburg, V. L., & Syrovatskii, S. I. 1964, *The Origin of Cosmic Rays* (New York: Pergamon)
- [30] Henke, B. L., Lee, P., Tanaka, T. J., Shimabukuro, R. L., & Fujikawa, B. K. 1982, *At. Data Nucl. Data Tables*, 27, 1
- [31] Hudson, H. S., Peterson, L. E., & Schwartz, D. A. 1971, *Nature*, 230, 177
- [32] Hyodo, Y., Tsujimoto, M., Koyama, K., Nishiyama, S., Nagata, T., Sakon, I., Murakami, H., & Matsumoto, H. 2008, *PASJ*, 60, 173
- [33] Hyodo, Y., Ueda, Y., Yuasa, T., Maeda, Y., Makishima, K., & Koyama, K. 2009, *PASJ*, 61, S99
- [34] Inui, T., Koyama, K., Matsumoto, H., & Tsuru, T. G. 2009, *PASJ*, 61, S241
- [35] Ishisaki, Y., et al. 2007, *PASJ*, 59, S113
- [36] Iwan, D., Shafer, R. A., Marshall, F. E., Boldt, E. A., Mushotzky, R. F., & Stottlmyer, A. 1982, *ApJ*, 260, 111
- [37] Jansen, F., et al. 2001, *A&A*, 365, L1
- [38] Jensen, P. L., et al. 2003, *A&A*, 411, L7
- [39] Kawai, N., Fenimore, E. E., Middleditch, J., Cruddace, R. G., Fritz, G. G., Snyder, W. A., & Ulmer, M. P. 1988, *ApJ*, 330, 130

- [40] Kelley, L. R., et al. 2007, PASJ, 59, S77
- [41] Kennea, J. A., & Skinner G. K. 1996, PASJ, 48, L117
- [42] Kokubun, M., et al. 2007, PASJ, 59, S53
- [43] Kotani, T., Kawai, N., Matsuoka, M., & Brinkmann, W. 1996, PASJ, 48, 619
- [44] Koyama, K., Makishima, K., Tanaka, Y., & Tsunemi, H. 1986a, PASJ, 38, 121
- [45] Koyama, K., Ikeuchi, S., & Tomisaka, K. 1986b, PASJ, 38, 503
- [46] Koyama, K., Awaki, H., Kunieda, H., Takano, S., Tawara, Y., Yamauchi, S., Hattakade, I., & Nagase, F. 1989, Nature, 339, 603
- [47] Koyama, K., Maeda, Y., Sonobe, T., Takeshima, T., Tanaka, Y., & Yamauchi, S. 1996, PASJ, 48, 249
- [48] Koyama, K., Hyodo, Y., & Inui, T. 2006, Journal of Physics Conference Series, 54, 95
- [49] Koyama, K., et al. 2007a, PASJ, 59, S23
- [50] Koyama, K., et al. 2007b, PASJ, 59, S221
- [51] Koyama, K., et al. 2007c, PASJ, 59, S245
- [52] Koyama, K., Inui, T., Matsumoto, H., & Tsuru, T. G. 2008, PASJ, 60, S201
- [53] Koyama, K., Takikawa, Y., Hyodo, Y., Inui, T., Nobukawa, M., Matsumoto, H., & Tsuru, G. T. 2009, PASJ, 61, S255
- [54] Krabbe, A., et al. 1995, ApJ, 447, L95
- [55] Kubota, A. et al. 2007, PASJ, 59, S185
- [56] Kushino, A., Ishisaki, Y., Morita, U., Yamasaki, N. Y., Ishida, M., Ohashi, T., & Ueda, Y., 2002, PASJ, 54, 327
- [57] LaRosa, T. N., Kassim, N. E., Lazio, T. J. W., & Hyman, S. D. 2000, A&A, 119, 207
- [58] Liszt, H. S., & Spiker, R. W. 1995, ApJS, 98, 259
- [59] Law, C., & Yusef-Zadeh, F. 2004, ApJ, 611, 858
- [60] Maeda, Y., Koyama, K., Sakano, M., Takeshima, T., & Yamauchi, S. 1996, PASJ, 48, 417
- [61] Maeda, Y., et al. 2002, ApJ, 570, 671
- [62] Markevitch, M., Sunyaev, R. A., & Pavlinsky, M. 1993, Nature, 364, 40
- [63] Matsumoto, H., et al. 2006, Proc. SPIE, 6266

- [64] Mazzotta, P., Mazzitelli, G., Colafrancesco, S., & Vittorio, N. 1998, *A&AS*, 133, 403
- [65] Mehringer, D. M., Palmer, P., & Goss, W. M. 1993, *ApJ*, 402L, 69M
- [66] Mendoza, C., Kallman, T. R., Bautista, M. A., & Palmeri, P. 2004, *A&A*, 414, 377
- [67] Mirabel, I. F. 1994, *ApJS*, 92, 369
- [68] Mitsuda, K., et al. 2007, *PASJ*, 59, S1
- [69] Mori, H., et al. 2005, *PASJ*, 57, 245
- [70] Mori, H., et al. 2007, *Proc. SPIE*, 6686
- [71] Mori, H., Tsuru, T. Go, Hyodo, Y., Koyama, K., & Senda, A. 2008, *PASJ*, 60, 183
- [72] Morris, M., & Serabyn, E. 1996, *ARA&A*, 34, 645
- [73] Munro, M. P., et al. 2004, *ApJ*, 613, 326
- [74] Munro, M. P., Bauer, F. E., Bandyopadhyay, R. M., & Wang, Q. D. 2006, *ApJS*, 165, 173
- [75] Munro, M. P., Baganoff, F. K., Brandt, W. N., Park, S., & Morris, M. R. 2007, *ApJL*, 656, L69
- [76] Munro, M. P., et al. 2008, *ApJS*, 181, 110
- [77] Murakami, H., Koyama, K., Sakano, M., Tsujimoto, M., & Maeda, Y. 2000, *ApJ*, 534, 283
- [78] Murakami, H., Koyama, K., & Maeda, Y. 2001, *ApJ*, 558, 687
- [79] Murakami, H., Koyama, M., Tsujimoto, M., Maeda, Y., & Sakano, M. 2001, *ApJ*, 550, 297
- [80] Nakajima, H., et al. 2008, *PASJ*, 60, S1
- [81] Nakajima, H. et al. 2009, *PASJ*, 61, S233
- [82] Nakashima, S., Nobukawa, M., Tsuru, T. Go, Koyama, K., & Uchiyama, H. 2010, *PASJ*, 62, 971
- [83] Nobukawa, M., et al. 2008, *PASJ*, 60, S191
- [84] Nobukawa, M., Koyama, K., Ryu, S. G., Tsuru, T. G., & Tatischeff, V. 2010, *PASJ*, 62, 423
- [85] Nobukawa, M., Ryu, S. G., Tsuru, T. G., & Koyama, K. submitted to *ApJL*
- [86] Oka, T., Hasegawa, T., Sato, F., Tsuboi, M., & Miyazaki, A. 1999 *ApJS*, 118, 455
- [87] Ozawa, M., et al. *PASJ*, 61, S1

- [88] Ozernoy, L. M., Genzel, R., & Usov, V. V. 1997, *MNRAS*, 288, 237
- [89] Park, S., Munro, M. P., Baganoff, F. K., Maeda, Y., Morris, M., Howard, C., Bautz, M. W., & Garmire, G. P. 2004, *ApJ*, 603, 548
- [90] Paumard, T., Maillard, J. P., Morris, M., & Rigaut, F. 2001, *A&A*, 366, 466
- [91] Pavlinsky, M. N., Grebenev, S. A., & Sunyaev, R. A. 1994, *ApJ*, 425, 110
- [92] Ponti, G., Terrier, R., Goldwurm, A., Belanger, G., & Trap, G. 2010, *ApJ*, 714, 732
- [93] Porquet, D., Rodrigues, J., Corbel, S., Goldoni, P., Warwick, R. S., Goldwurm, A., & Decourchelle, A. 2003, *A&A*, 406, 299
- [94] Predehl, P., & Trümper, J. 1994, *A&A*, 290, L29
- [95] Predehl, P., & Schmitt, J. H. M. M. 1995, *A&A*, 293, 889
- [96] Predehl, P., & Zinnecker, H. 1996, in *ASP Conf. Ser. 102, The Galactic Center*, ed. R. Gredel (San Francisco: ASP), 415
- [97] Predehl, P., Costantini, E., Hasinger, G., & Tanaka, Y. 2003, *Astronomische Nachrichten*, 324, 73
- [98] Prigozhin, G., Burke, B., Bautz, M., Kissel, S., & Lamarr, B. 2008, *IEEE Transactions on Electron Devices*, 55, 2111
- [99] Protheroe, R. J., Wolfendale, A. W., & Wdowczyk, J., 1980, *MNRAS*, 192, 445
- [100] Rasmussen, A. P., Behar, E., Kahn, S. M., den Herder, J. W., & van der Heyden, K. 2001, *A&A*, 365, L231
- [101] Revnivtsev, M. G., et al. 2004, *A&A*, 425, L49
- [102] Revnivtsev, M., Vikhlinin, A., & Sazonov, S. 2007, *A&A*, 473, 857
- [103] Rieke, G. H., Rieke, M. J., & Paul, A. E. 1989, *ApJ*, 336, 752
- [104] Plucinsky, P. P., et al. 2008, *Proc. SPIE*, 7011
- [105] Ryu, G. S., Koyama, K., Nobukawa, M., Fukuoka, R., & Tsuru, G. T., 2009, *PASJ*, 61, 751
- [106] Sakano, M., Imanishi, K., Tsujimoto, M., Koyama, K., & Maeda, Y. 1999, *ApJ*, 520, 316
- [107] Sakano, M., Koyama, K., Murakami, H., Maeda, Y., & Yamauchi, S. 2002, *ApJS*, 138, 19
- [108] Sato, F., Hasegawa, T., Whiteoak, J. B., & Miyawaki, R. 2000, *ApJ*, 535, 857
- [109] Sawada, T., Hasegawa, T., Handa, T., & Cohen, R. J. 2004, *MNRAS*, 349, 1167

- [110] Serlemitsos, P. J., et al. 1995, PASJ, 47, 105
- [111] Serlemitsos, P. J., et al. 2007, PASJ, 59, S9
- [112] Sidoli, L., Mereghetti, S., Israel, G. L., Chiappetti, L., Treves, A., & Orlandini, M. 1999, ApJ, 525, 215
- [113] Sidoli, L., Mereghetti, S., Favata, F., Oosterbroek, T., & Parmar, A. N. 2006, ApJ, 456, 287
- [114] Skinner et al.(1987) Skinner, G. K., Willmore, A. P., Eyles, C. J., Bertram, D., & Church, M. J. 1987, Nature, 330, 544
- [115] Smith, D. M., Heindl, W. A., & Swank, J. H. 2002, ApJ, 578, 89
- [116] Sofue, Y. 1990, PASJ, 42, 827
- [117] Sofue, Y. 1995, PASJ, 47, 527
- [118] Strüder, L., et al. 2001, A&A, 365, L18
- [119] Sunyaev, R. A., Markevitch, M., & Pavlinsky, M. 1993, ApJ, 407, 606
- [120] Sunyaev, R., & Churazov, E. 1998, MNRAS, 297, 1279
- [121] Takahashi, T., et al. 2007, PASJ, 59, S35
- [122] Tanaka, Y., Koyama, K., Maeda, Y., Sonobe, T. 2000, PASJ, 52, L25
- [123] Tatischeff, V. 2003, in Final Stage of Stellar Evolution, ed. C. Motch & J. M. Hameury (Les Ulis: EDP Sciences), 79
- [124] Tawa, N., et al. 2008, PASJ, 60, S11
- [125] Terrier, R., et al. 2010, ApJ, 719, 143
- [126] Tomida, H., et al. 1997, PASJ, 49, 405
- [127] Tsuboi, M., Handa, T., & Ukita, N. 1999, ApJS, 120, 1
- [128] Tsujimoto, M., Hyodo, Y., & Koyama, K. 2007, PASJ, 59, S229
- [129] Turner, M. J. L., et al. 2001, A&A, 365, L27
- [130] Uchiyama, H., et al. 2009, PASJ, 61, S9
- [131] Uchiyama, Y., et al. 2008, PASJ, 60, S35
- [132] Valinia, A., Tatischeff, V., Arnaud, K., Ebisawa, K., & Ramaty, R. 2000, ApJ, 543, 733
- [133] Watson et al.(1981) Watson, M. G., Willingale, R., Hertz, P., & Grindlay, J. E. 1981, ApJ, 250, 142

- [134] Weisskopf, M. C., Brinkman, B., Canizares, C., Garmire, G., Murray, S., & Van Speybroeck, L. P. 2002, *PASP*, 114, 1
- [135] Werner, N., et al. 2003, *A&A*, 416, 311
- [136] Worrall, D. M., Marshall, F. E., Boldt, E. A., & Swank, J. H. 1982. *ApJ*, 255, 111
- [137] Yamaguchi, H., et al. 2006, *Proc. SPIE*, 6266
- [138] Yamauchi, S., Kawada, M., Koyama, K., Kunieda, H., Tawara, Y., & Hatsukade, I. 1990, *ApJ*, 365, 532
- [139] Yusef-Zadeh, F., Law, C., Wardle, M., Wang, Q. D., Fruscione, A., Lang, C. C., & Cotera, A. 2002, *ApJ*, 570, 665
- [140] Yusef-Zadeh, F., Munro, M., Wardle, M., & Lis, D. C. 2007, *ApJ*, 656, 847